Title

Assessment of Embryo Health and Circulating Tumor Cell Metabolism Using the Phasor-FLIM Approach

Author

Ma, Ning

Publication Date

2019

UNIVERSITY OF CALIFORNIA,
IRVINE

Assessment of Embryo Health and Circulating Tumor Cell Metabolism Using the Phasor-FLIM Approach

DISSERTATION

submitted in partial satisfaction of the requirements
for the degree of

DOCTOR OF PHILOSOPHY

in Biomedical Engineering

by

Ning Ma

Dissertation Committee:
Assistant Professor Michelle Digman, Chair
Professor Enrico Gratton
Assistant Professor Timothy Downing

2019

DEDICATION

To

my family

TABLE OF CONTENTS

LIST OF FIGURES

LIST OF TABLES

ACKNOWLEDGMENTS

I would like to express the deepest appreciation to my committee chair and my Ph.D. adviser, Professor Michelle Digman. Her support, guidance and numerous hours of discussion help me to reshape from a clueless student to a female scientist who will never stop innovation. I would like to extend my acknowledgment to my committee members, Professor Enrico Gratton, and Professor Timothy Downing for their insightful comments, the wealth of knowledge and extraordinary vision.

In addition, I would like to extend my gratitude to all the members and visitors in Digman lab as well as Laboratory for Fluorescence Dynamics (LFD) and UCI friends who supported me in all aspects. I would like to thank everyone from the 1st Digman lab Ph.D. squad, Dr. Emma Mah, Dr. Sara Sameni, Dr. Andrew Trinh and Dr. Michael Muruta for all the help and support on scientific researches and daily life. I am thankful to Hongtao Chen for always being there to fix hardware related issues and answer my questions about optical imaging techniques; Milka Titin for taking care of LFD family and teaching and helping me for the sample preparation; Andrea Anzalone and Paolo Annibale for guiding my first research steps; Carmine de Rienzo for the passionate of science, the little Matlab support group as well as the spirit of helping everyone, I will always remember him; Jenu Chacko, Leonel Malacrida, Suman Ranjit for all the discussion and insights about science, chemistry, optical imaging, and life; Sasha (Alexander Dvornikov) for helping me with imaging on the DIVER; Tracey for welcoming me and bringing fun to us all the time. I would also like to thank Sohail Jahid, Alessandro Rossetta, Ylenia Santoro, Rachel Cinco-Hedde, Jie Zheng, all my study group members, UCI innovation team people, … this list can go on and on, and I am thankful to all the friends and scientists I met during my Ph.D. who help me to be who I am now. A special thanks to Xin Tong for always being there.

I will take this opportunity to thank all my collaborators from Cho lab, Lee lab and Donovan lab and more for the knowledge, insightful views from different aspects and teamwork. I would like to thank all my students I mentored. They help me develop the ability and spirit to be a teacher and help others to succeed. I would like to thank the UCI innovation center, UCI associated graduate students, Foundation of reproductive medicine, and Maschoff Brennan law firm for the awards. These achievements really encourage me to move forward for my career.

I would like to express my sincere gratitude to my parents Dr. Guiyang Ma and Suzhi Liu as well as my families and friends in China. Their unconditional love and support keep me going and never lost. They are my lighthouse even though we are oceans apart. Last but not the least I wish to thank my husband Zhenghao Li who supports me to continue the career I love without any concerns. I cannot express enough appreciation for our relationship.

This work is made possible with the funding source from National Institutes of Health (NIH), including 2P41GM103540 and R21HD090629, California Institute for Regenerative Medicine (CIRM) 100000900 RB5-07458, Hellman Fellows Fund.

CURRICULUM VITAE

Education

2007-2012	B.S. in Chemical Engineering, Dalian University of Technology B.A. in English Literature, Dalian University of Technology
2012-2013	M.S. in Chemical and Biochemical Engineering, University of California, Irvine
2014-2019	Ph.D. in Biomedical Engineering, University of California, Irvine

Research Experience

2014-2019	Graduate Student Researcher, Digman's Lab/ Laboratory for Fluorescence Dynamics, Department of Biomedical Engineering, University of California, Irvine
2014	Junior Specialist, Laboratory of Fluorescence Dynamics, University of California, Irvine
2008-2012	Research Assistant, Dr. Tonghua Wang's Carbon Research Lab, Key National Laboratory of Fine Chemicals, Dalian University of Technology, Dalian, China

Honors/Awards

Nov. 2018	Foundation of Reproductive Medicine Young Investigator Award New York, NY
Nov. 2018	Student Startup Fund Micro-grant University of California, Irvine
Nov. 2018	UC Irvine Associated Graduate Students Travel Grant University of California, Irvine
Sep. 2018	Maschoff Brennan Innovator Scholarship Irvine, CA

Jun. 2018	Student Startup Fund Micro-grant University of California, Irvine
Jun. 2018	Wayfinder Incubator Program 2018 University of California, Irvine
Jun. 2018	Finalist of Beall student design & Butterworth product development competition University of California, Irvine
May 2018	Proof of Product grant University of California, Irvine
Apr. 2018	Selected team NSF I-Corps Sprint 2018 University of California, Irvine
Feb. 2018	UC Irvine Associated Graduate Students Travel Grant University of California, Irvine
2010	Award in University Innovation Research and Training Program Dalian University of Technology, Dalian, China
2010	Award in Outstanding Contribution to Student Union Dalian University of Technology, Dalian, China

Publications

- **Ning Ma***, Nabora Reyes de Mochel*, Paula Pham, Tae Yoo, Ken Cho, Michelle Digman. Label-free assessment of pre-implantation embryo quality by the Fluorescence Lifetime Imaging Microscopy (FLIM)-phasor approach. Nature Scientific Reports. 2019 (submitted)

- **Ning Ma***, Gopakumar Kamalakshakurup*, Michelle Digman and Abraham. High-Efficiency Single Cell Encapsulation in Droplets and Label-Free Characterization using Fluorescent Lifetime Imaging Microscopy. Cytometry Part A. 2019

- Hongtao Chen, **Ning Ma**, Keiichiro Kagawa, Michelle Digman and Enrico Gratton. Widefield multi-frequency fluorescence lifetime imaging using a two-tap CMOS camera with lateral electric field charge modulators. Journal of biophotonics. 2018

- **Ning Ma***, Nabora Reyes de Mochel*, Paula Pham, Tae Yoo, Ken Cho, Michelle Digman. Label-free assessment of pre-implantation embryo quality by the Fluorescence Lifetime Imaging Microscopy (FLIM)-phasor approach. bioRxiv. 2018

- Do-Hyun Lee, Xuan Li, **Ning Ma**, Michelle Digman, Abraham Lee. Rapid and label-free identification of single leukemia cells from blood in a high-density microfluidic trapping array by Fluorescence Lifetime Imaging Microscopy. Lab on a chip. 2018

- **Ning Ma**, Michelle A. Digman, Leonel Malacrida, and Enrico Gratton. Measurements of absolute concentrations of NADH in cells using the phasor FLIM method. Biomed. Opt. Express. 2016

* Co-first author

Conference Presentations

-"Label-free Detection of Pre-implantation Embryo Developmental Potential via the Fluorescence Lifetime Imaging and Hyperspectral Microscopy." The 4th Annual Conference of the Foundation for Reproductive Medicine Translation Reproductive Biology and Clinical Reproductive Endocrinology. New York City, New York, USA. 2018.

-"Quiescent metabolism identification in 1-1 encapsulation droplet via Fluorescence Lifetime Imaging Microscopy (FLIM)". NanoEngineering for Medicine and Biology Conference. Los Angeles, California, USA. 2018.

-"Fluorescence Lifetime Trajectory of the Mouse Pre-implantation Embryo Predicts its Viability." Cell Symposia: Multifaceted Mitochondria. San Diego, California, USA. 2018.

-"Quiescent metabolism identification in 1-1 encapsulation droplet via Fluorescence Lifetime Imaging Microscopy (FLIM)". TechConnect WORLD INNOVATION conference & EXPO. Anaheim, California. 2018.

-"Fluorescence Lifetime Trajectory of the Mouse Pre-implantation Embryo Predicts its Viability." 62nd Biophysical Society Annual Meeting. San Francisco, California, USA. 2018.

-"Quiescent metabolism identification in 1-1 encapsulation droplet via Fluorescence Lifetime Imaging Microscopy (FLIM)". Center for Advanced Design and Manufacturing of Integrated Microfluidics (CADMIM) Industrial Advisory Board Meeting, Chicago, Illinois. 2018.

-“Label-free Identification of Single-Cell encapsulated in droplet by Phasor-Fluorescence Lifetime Imaging (FLIM)” Center for Advanced Design and Manufacturing of Integrated Microfluidics (CADMIM) Industrial Advisory Board Meeting, Chicago, Illinois. 2017.

-“Fluorescence Lifetime Trajectory of the Mouse Pre-implantation Embryo Predicts its Viability.” Japan-UCI Meeting on 3D Morphogenesis conference. 2017.

-“Fluorescence Lifetime Trajectory of the Mouse Pre-implantation Embryo Predicts its Viability.” The 18th Annual UC Systemwide Bioengineering Symposium. 2017.

-“Non-invasive Fluorescence Lifetime Imaging (FLIM) of stem cell signature metabolic states.” 60th Biophysical Society Annual Meeting. Los Angeles, California, USA. 2016.

-“Fluorescence Lifetime Imaging Microscopy of Extravasating Cancer Cells inside the Mouse Microenvironment.” Los Angeles, California. 2015.

-Chao Family Comprehensive Cancer Center’s Scientific Retreat; “Fluorescence Lifetime Imaging Microscopy of Extravasating Cancer Cells Inside the Mouse Microenvironment.” Palm Springs, California. 2014.

Teaching and Mentorship

2016	Teaching Assistant, Department of Biomedical Engineering, University of California, Irvine
2017-	Mentor for “Pathways to Biophotonics and Biomedical Engineering (PBBE)” Training Program
Mar. 2017	Orange County Science and Engineering Fair Judge, Orange County, CA
2016-	Lecturer, Laboratory for Fluorescence Dynamics workshop, University of California, Irvine
2016-	Project Leader, Mathematical, Computational and Systems Biology (MCB) Bio Bootcamp, University of California, Irvine
2016	Mentor for Graduate Student Senior Design, University of California, Irvine

Oct. 2015	“Ask-A-Scientist Night” Science Fair Advisor, Irvine Unified School District, Rancho San Joaquin Middle School, Irvine
2014-	Project Leader, Laboratory for Fluorescence Dynamics workshop, University of California, Irvine
2014-	Project Leader, Undergraduate Student Initiative for Biomedical Research, University of California, Irvine
2014-	Project Leader, COSMOS: California State Summer School for Math & Science

ABSTRACT OF THE DISSERTATION

Assessment of Embryo Health and Circulating Tumor Cell Metabolism Using the Phasor-FLIM Approach

By

Ning Ma

Doctor of Philosophy in Biomedical Engineering

University of California, Irvine, 2019

Professor Michelle Digman, Chair

Cellular functional and structural changes associated with metabolism are essential for understanding healthy tissue development and the progression of numerous diseases. Quantitatively monitoring of metabolic processes would spur medical research towards developing precise diagnostic tools, treatment methods, and preventive strategies for reducing the impact of the diseases. Unfortunately, established methods for this purpose are either destructive or require the use of exogenous agents. Recent work has highlighted the potential of endogenous two-photon excited fluorescence as a method to monitor subtle metabolic changes. In this thesis, we apply two-photon fluorescence lifetime imaging microscopy (FLIM) of intrinsic fluorophores for label-free metabolic imaging in pre-implantation embryos and other biological samples.

We exploited the intrinsically fluorescent coenzyme reduced nicotinamide adenine dinucleotide (NADH), an endogenous probe extensively used for metabolic imaging. We

propose a graphical method using the phasor representation of the fluorescence decay to derive the absolute concentration of NADH in cells. Using phasor-FLIM, we identified unique metabolic states that distinguish embryonic stem cells from differentiating progeny. We also apply the phasor-FLIM and hyperspectral microscopy to capture endogenous fluorescent biomarkers of pre-implantation embryos as a non-morphological and non-invasive caliber for embryo quality. We identify the unique spectroscopic trajectories at different stages of mouse pre-implantation development which can be further used to distinguish pre-implantation embryo quality using an artificial intelligence algorithm at the early compaction stage with 86% accuracy. Furthermore, we showed the heterogeneity and changes in the normal pre-implantation embryos and aneuploidy embryos treated with the spindle assembly checkpoint inhibitor during embryo division can be rapidly distinguished at blastocyst stage via spectra phasor.

Finally, we designed rapid and label-free single leukemia cell identification platform that combines high-throughput size-based separation of hemocytes, and leukemia cell identification through phasor approach and phasor-FLIM to quantify changes between free/bound NADH as an indirect measurement of metabolic alteration in living cells. These examples illustrate the potential of fluorescence lifetime imaging microscopy for unveiling complex physiological processes. Detailed image analysis and combined microscopy modalities will continue to reveal and quantify fundamental biology that will support the advance of biomedicine.

Chapter 1

Metabolism

Chapter overview: In this thesis, we demonstrate the applications of two-photon fluorescence lifetime imaging microscopy in the assessment of metabolism for normal and pathological states, in a wide range of biological samples – embryonic stem cells, pre- and post-implantation embryos as well as microfluidic device cultured cells. Furthermore, we establish a novel technique for absolute Nicotinamide adenine dinucleotide (NADH) concentration measurement. This chapter discusses the basics of metabolism and the enzyme facilitated metabolic pathways along with current techniques available for measurement of metabolism. The chapter concludes with establishing the importance of quantitatively non-invasive imaging of metabolites.

1.1 Classification of Energy Metabolism

"Metabolism is the set of life-sustaining chemical reactions in organisms."[1]

The metabolism is derived from the Greek word Μεταβολισμός for "change". Cells are constantly changing and carrying out thousands of chemical reactions needed to sustain the life of the cells, human body, and all the organisms. All of the chemical reactions that take place inside of a cell are collectively called the cell's metabolism. Metabolism is fundamentally important for identification between healthy and unhealthy cells, tumor heterogeneity, viability wound healing, diabetes, and neurodegenerative disorders[2-6]. The quantitative measurement of the metabolites can be applied as a diagnostic and drug screening tool due to the reflection of the changes during disease development and treatment response[7-9].

There are three types of metabolic processes that are crucial to life on earth, anabolism, catabolism, and waste disposal[6,10]. *Anabolism* is a “building up”, or synthesis of small molecules and their polymerization into complex macromolecules and these processes typically require adenosine triphosphate (ATP) molecules, the currency of energy. Whereas *Catabolism* is a “breaking down”, or digestion of large molecules (polysaccharides, lipids, nucleic acids, and proteins) into smaller subunits (monosaccharides, fatty acids, nucleotides, and amino acids) with the release of ATP. The pathways that help eliminate the toxic waste produced by other class are *Waste Disposal.* Within the typical eukaryotic cell, the main catabolism pathway to produce energy are known to be cellular respiratory which including (1) glycolysis, (2) the citric acid cycle, also known as TCA cycle (tricarboxylic acid cycle) or the Krebs cycle, and (3) Oxidative phosphorylation (or electron transport chain, ETC), [11] (Figure 1. 1).

Glycolysis is the first step for this three-phase energy production, which literally means the breaking down of glucose. This process initiates from the phosphorylation of a glucose molecule which takes 2 ATPs as an energy investment and 2 nicotinamide adenine dinucleotide (NAD+) as raw materials. The end-products are two glyceraldehyde-3-phosphate (GAP) molecules which are very unstable and can be reconfigured into two interconvertible three-carbon molecules[12]. As a consequence, glycolysis ends up with 2 pyruvates, 2 net ATPs and 2 NADH in total for every molecule of glucose this pathway starts with. The entire process does not require the existence of oxygen and happens in the cell cytosol.

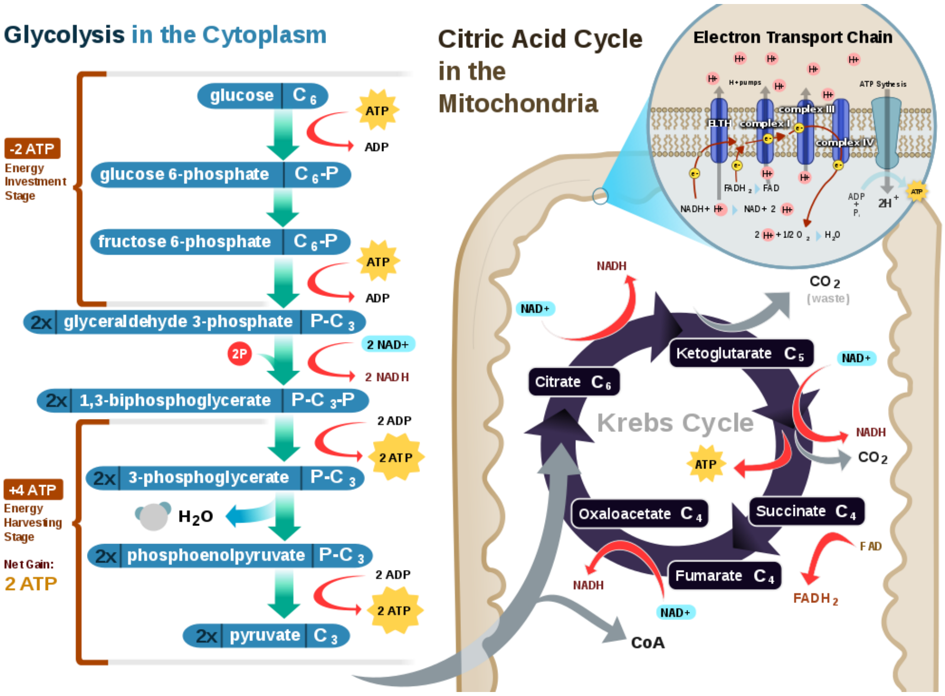

Figure 1. 1 Overview of respiratory metabolism

Figure 1. 1 Overview of respiratory metabolism. This diagram shows the relationship among the major pathways, glycolysis, Krebs cycle (AKA citric acid cycle), and the electron transport chain (AKA oxidative phosphorylation), where the reactions comprising these pathways are located in the cell, and some of the products derived from these pathways. (Figure from https://en.wikipedia.org/wiki/Cellular_respiration. This work is licensed by Copyright (C) 2000, 2001, 2002 Free Software Foundation, Inc.)

Subsequently, in the presence of oxygen, pyruvate is transported across the mitochondrial membrane and then decarboxylated to produce acetyl coenzyme A (acetyl-CoA) with the production of two molecules of NADH and carbon dioxide. The acetyl CoA is then oxidized by a cyclical series of enzyme-catalyzed reactions known as tricarboxylic acid

(TCA) cycle, also known as the Krebs cycle. During the Krebs cycle, electrons are removed from acetyl CoA and these electrons reduce more NAD+, along with another electron carrier, flavin adenine dinucleotide (FAD). The acetyl-CoA enters the Krebs cycle can be fully oxidized to 4 CO_2 molecules, 6 reduced NADH molecules, and 2 reduced $FADH_2$. Each NADH and $FADH_2$ molecule created in all the above steps is an important source of energy and donates electrons to the electron transport chain (ETC) and this coenzyme oxidized process generates ATP.

The electron transport chain is the final step of the cellular respiratory which composed of protein complexes that are located in the inner membrane of the mitochondria. The high-energy carriers NADH and $FADH_2$ can themselves be oxidized by the electron transport chain. The hydrogen atoms (protons) liberated from NADH and $FADH_2$ form a gradient across the inner membrane and create an electrochemical potential which is used by a protein complex to drive the phosphorylation of Adenosine Di Phosphate (ADP) to produce ATP. The last molecule that is reduced is oxygen, which results in the generation of water molecules.

Besides the primary energy production metabolism, there is a pentose phosphate pathway (PPP pathway) which is parallel to glycolysis[13]. It generates NADPH and pentoses (5-carbon sugars) as well as ribose 5-phosphate, the last one is a precursor for the synthesis of nucleotides to build the backbone for both RNA and DNA. Even though it does involve oxidation of glucose, its primary role is anabolic rather than catabolic.

For one molecule of glucose, 30-38 ATP can be produced via cellular respiration [14]. Whereas, only two are produced by glycolysis. Oxidative phosphorylation is a way more efficient energy production pathway than glycolysis. However, when limited amounts of oxygen are available, the cells might shift to anaerobic glycolysis where pyruvate is converted to lactate. In addition, most highly proliferative cells, stem cells, and cancer cells predominantly produce their energy through aerobic glycolysis, also termed the Warburg effect even in the presence of abundant oxygen[15]. Even though the Warburg effect is not an efficient pathway to produce energy, this metabolism adaptation is beneficial for maximizing the rapid uptake and incorporation of nutrients for macromolecule biosynthetic reactions[16-18]. For instance, there is a high demand for fatty acids incorporated diglyceride phospholipids that make up the bulk of cellular membranes for the cellular division of the highly proliferative cells. During this process, palmitic acid is the first fatty acid produced during fatty acid synthesis and is the precursor to longer fatty acids. The synthesis of palmitate requires the input of 8 molecules of acetyl-CoA, 14 molecules of NADPH, and 7 molecules of ATP. The bottleneck for the fatty acid metabolism to produce energy in a fast manner is the production of acetyl-CoA and NADPH instead of pure energy production[19]. Thus, the Warburg effect can fulfill the requirement for biosynthesis and nutrient uptake.

1.2 Techniques to study metabolism

Metabolism sustains cellular bioenergetics, and their balance is critical for the cellular normal development and aging. On the other hand, metabolic perturbations or dysfunctions are often implicated in different diseases, including developmental mitochondrial disease, neurodegenerative and cardiovascular disorders, diabetes, and cancer[20-24]. Metabolic responses can be highly dynamic and heterogeneous both temporally and spatially, and this inherent heterogeneity can significantly affect the disease diagnosis, development and response to treatment. Almost 80 years ago, Hans Krebs and his assistant Henseleit discovered the first metabolic cycle - ornithine cycle by the basic biochemistry method[25]. Since then, scientists have been using different techniques to study metabolism. Metabolic flux analysis (MFA) using stable isotope labeling is an important tool for explaining the flux of certain elements through the metabolic pathways and reactions within a cell[26]. A new age of study of metabolic pathways came with the emergence of genomics. Metabolomics can profile the comprehensive molecule composition of the biological sample of interest like tissue or cell extract, culture media or biofluids in order to characterize the endogenous substrates of enzymes[27]. The analysis of metabolites can be accomplished based on the techniques like mass spectrometry coupled with chromatography techniques including high performance liquid chromatography (HPLC), ultra performance liquid chromatography (UPLC), gas chromatography (GC) or capillary electrophoresis (CE) followed by multivariate statistical analysis for pattern-recognition and biological interpretation[28]. Other spectroscopic technologies have emerged as a non-invasive means of revealing embryo viability via detection of various metabolic states of common molecules associated with embryo development. Raman spectroscopy, near-infrared, Nuclear Magnetic Resonance (NMR), thin-layer chromatography (TLC) and Fourier-transform infrared spectroscopy (FT-IR) can also detect the metabolic states of pyruvate, lactate, glucose, and oxygen during pre-implantation mammalian development[29-31]. However, the current method used to measure the metabolites is based on either indirect measurement of metabolites in culture media or conventional biochemical methods of lysates from a group of cells. Thus, the morphological context cannot be kept given the fact that these assays require the destruction of the cells and tissues. It is imperative to develop non-invasive, measurements of metabolites in real time within the cells and tissues. These features have inspired the development of several approaches. Some of them include auto-radiography to study metabolite 2-deoxyglucose and positron emission tomography (PET) scanning to study Fluorodeoxyglucose (FDG-PET). FDG-PET has been employed in clinical diagnostic imaging of various kinds of tumors[19,32]. Some studies reported the use of 4-fluoroglutamines PET for metabolic imaging[33]. Magnetic resonance (MR) spectroscopy employing nuclei like 1H, 13C, 31P, and 19F is also used for metabolic imaging[34]. The potential limitation of these techniques is the requirement of radiolabeling. Analysis of extracellular flux to measure oxygen consumption rate (OCR) and extracellular acidification rate (ECAR) to evaluate mitochondrial respiration and glycolysis respectively using the Seahorse technology has been gaining popularity over the past decade[35,36]. However, these techniques analyze the media over the monolayer of cells or extracted tissue within a microplate, thus lacking in spatial information and cannot be translated to in vivo measurements.

1.3 Chapter Summary

In this chapter, we briefly introduce the basics of cell metabolism. We establish the motivation to study these parameters by discussing their significance in regulating normal physiology and pathogenesis. Next, we consider some of the alternative techniques currently employed for metabolism and oxidative stress measurements and their shortcomings. We conclude the chapter by emphasizing the needs of a non-invasive method to study metabolic pathways without any perturbation to the Biosystems.

Chapter 2

Fluorescence Lifetime Imaging Microscopy

Chapter overview: To study the metabolism in a non-invasive manner, we use the fluorescence lifetime imaging (FLIM) microscopy to investigate the metabolism activity through the detection of endogenous fluorescent molecules. In this chapter, we will introduce the basics of the FLIM technique, and the graphical phasor method coupled with FLIM to perform the data analysis and interpretation. And we also applied a few other spectroscopy techniques applied in certain projects, including hyperspectral imaging and second harmonic generation (SHG) and third harmonic generation (THG). The detailed explanation and application of these techniques will be provided in the relevant chapters.

2.1 Phasor-Fluorescence Lifetime Imaging Microscopy

Fluorescence lifetime (τ) is the time of a fluorophore spends in the excited state before returning to the ground state by emitting a photon. When a fluorophore is excited, the lifetime is the time it takes for the number of excited molecules to decay to $1/e$ of the original value. The fluorescence lifetime information can be used to perform multiple quantitative fluorescence measurements including Förster resonance energy transfer (FRET), polarization and quenching, etc. The significant advantage of lifetime measurements is that there is no need for wavelength-ratiometric probes to provide a quantitative determination of many analytes. So, this method could be used for analytes which have no direct probes including, metabolites, antigens, or any affinity or immunoassays based on fluorescence energy transfer transduction mechanism. On the contrary, the lifetime method expands the sensitivity of the analyte concentration range by the use of probes with spectral shifts.

Fluorescence lifetime can be measured by time domain FLIM or frequency domain FLIM. The time domain method involves the illumination of the specimen (cells, tissue or cuvette) with a short pulse of light and the intensity of the emission versus time is recorded via the slope of the decay curve. If the decay is single exponential and the lifetime is long compared to the exciting light, then the lifetime can be determined directly from the slope of the curve. If the lifetime and the excitation pulse width are comparable, some type of the deconvolution method must be used to extract the lifetime. For the frequency domain method, the sinusoidal modulation of the incident light at high frequencies will be applied. In this method, the emission occurs at the same frequency as the incident light accompanied with a phase delay and demodulation (change in the amplitude relative to the excitation light). This method is not as calculation-demanding as the time domain FLIM.

Phasor-FLIM is a way to analyze the data by calculating the decay curve of a fluorescent species without the use of fitting (Figure 2. 1 A). In FLIM, an ultra-fast pulsed 2-photon laser is used to measure the intensity at short time windows (time arrival of the photons) as a function of time. Instead of fitting the decay curve into an exponential equation, the raw data (intensity at each pixel) is transformed into polar coordinates by plotting the sine and cosine using the Fourier transformation. Thus, the phasor approach is a fit-free analysis of FLIM imaging, and the g and s coordinates represent the decay curve at each pixel of the image. More specifically, in the phasor plot if the decay is a single exponential $I(t) = Ae^{-t/\tau}$ the coordinates are given by:

$$g_i(\omega) = \int_0^\infty I(t)\cos(\omega t)dt \,/ \int_0^\infty I(t)dt$$

$$s_i(\omega) = \int_0^\infty I(t)\sin(\omega t)dt \,/ \int_0^\infty I(t)dt$$

Therefore, a phasor analysis transforms complicated spectrum and decay into a unique position on the phasor plot. It can be used to measure the endogenous fluorescence of a sample to detect the biochemical reactions occurring in a live specimen, such as oxidation and reduction. The phasor analysis applies a Fourier transform to the fluorescence decay of each pixel resulting in a point that is plotted on a phasor plot. This enables each pixel in the plot to be compared to species, such as metabolites, of known lifetimes. Recently a metabolic trajectory (the "M-Trajectory") has been identified as the Phasor-FLIM trajectory for reducing to oxidizing conditions, which are indicative of cellular, glycolytic (high free/bound NADH ratios) to an oxidative phosphorylation phenotype (low free/bound NADH ratios, Figure 2. 1 C-D).

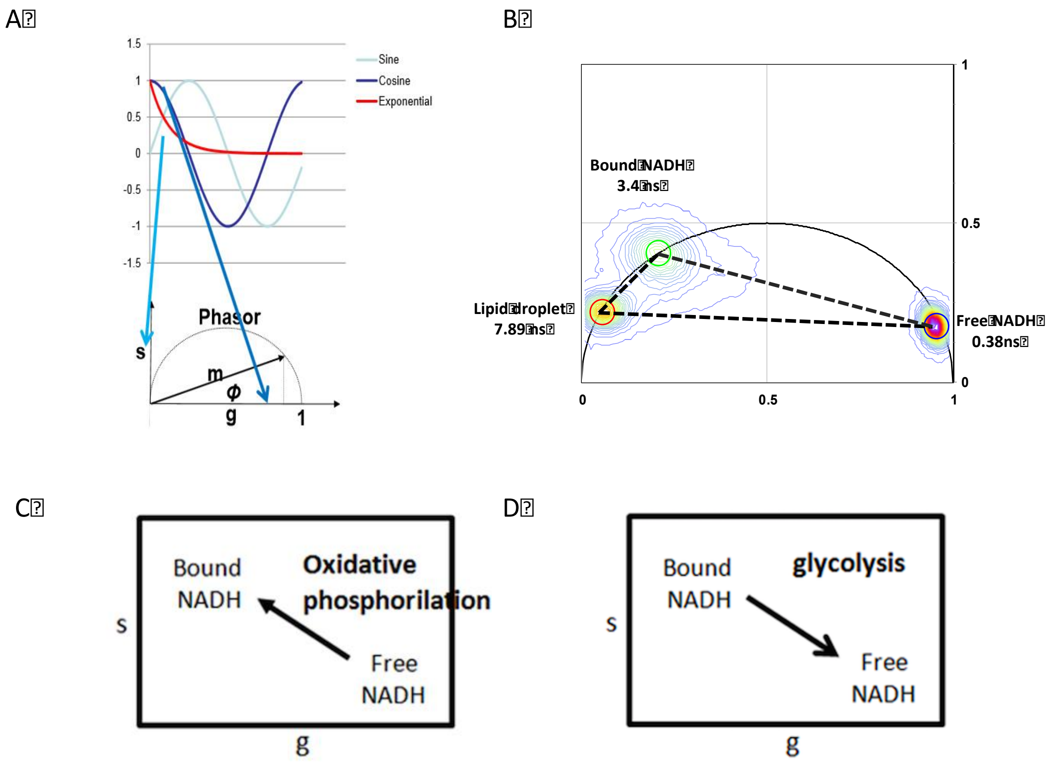

Figure 2. 1 Phasor-FLIM analysis

Figure 2. 1 Phasor-FLIM analysis and application. A) A schematic demonstrates the transformation from lifetime to phasor coordinates. B) Phasor fingerprint of pure intrinsic biomarkers of free NADH in solution, bound NADH in the presence of lactate dehydrogenase, and a long lifetime species derived from lipid droplets. Based on the law of phasor addition, any sample contains the combination signature of these three species will fall within the triangle joining the three phasors. C) The schematic diagram indicates that glucose uptake shifts cellular metabolic signature toward a glycolytic phenotype with high ratios of free/bound NADH. D) The schematic diagram indicates that the inhibition of glycolysis through DCA treatment shifts cellular metabolic signature toward an oxidative phosphorylation phenotype with low ratios of free/bound NADH.

2.2 Endogenous fluorophores and NADH

There are a lot of biomolecules that can emit light in the visible range when excited at proper wavelengths (table 1)[37-40]. The quantum yield and spectrum properties of these native fluorophores can be affected by the state of the microenvironment and, thus, provide functional and morphological information of the living system. Unlike conventional staining, the endogenous fluorescence does not require complicated sample preparation and can rule out the complexity induced by exogenous chemicals. When combined with optical imaging, tissue beneath the surface can be examined without disturbance and provide the possibility for noninvasive optical biopsy[41].

Table 1 The excitation and emission wavelengths of endogenous fluorophores

ENDOGENOUS FLUOROPHORE	EXCITATION (NM)	EMISSION (NM)
NAD(P)H	340	400-550
FLAVINS, FAD	380-490	520-560
FLAVIN MONONUCLEOTIDE (FMN)	444	558
RETINOL	330	500
RIBOFLAVIN	327	510
TRYPTOPHAN	280	300-350
MELANIN	broad	360-560
ELASTIN	370	420-510
COLLAGEN	330	305-450

NADH is one of the main fluorescent metabolic coenzymes involved in oxidative phosphorylation (OXPHOS) and glycolysis, reporting metabolic changes associated with cell carcinogenesis and differentiation. The reduced form NADH and oxidized form NAD+ takes part in the mitochondrial function, energy metabolism, calcium homeostasis, gene expression, oxidative stress, aging, and apoptosis. The reduced NADH phosphate (NADPH) is associated with reductive fatty acid biosynthesis and steroids, oxidative stress, anti-oxidation and the oxidized form, NADP+, is involved with calcium homeostasis[42]. Real-time monitoring cellular metabolism during pathophysiological changes is possible by of the measuring the redox ratio (NADH: NAD+). As mentioned in Chapter 1, NADH is the high-efficient carrier involved in each phase of the cellular respiratory process. Thus, the reduction-oxidation pair NADH: NAD+ serves as an indicator of the balance between oxidative phosphorylation and glycolysis. Bird, et al. demonstrated a correlation between the redox ratio NADH: NAD+ and the ratio of free to protein bound NADH, which is advantageous in fluorescent-based technique because unlike NADH, NAD+ is not fluorescent[43]. On the basis of the pivotal role of NADH in cell biology and metabolism, it has the potential to be employed as an endogenous biomarker for cellular redox reactions, energy metabolism and mitochondrial anomalies under different pathophysiological conditions. The most important property of NADH that makes it an attractive biomarker in optical imaging is its endogenous fluorescence with an absorption maximum of 340nm and emission maximum of 470nm[37]. More importantly, its fluorescence is affected by the local environment and protein binding which is dependent on metabolism. This allows non-invasive metabolic imaging of cells and tissue in their native physiological environment avoiding perturbation of the biological system.

Endogenous NADH fluorescence has been used extensively to study metabolism. Combination of NADH and FAD fluorescence intensity in the form of the redox ratio FAD/(NADH+FAD) had been proposed in late 1960s[44]. This ratiometric approach, where an increase in the ratio indicated lower metabolic activity, has also been widely employed to explore metabolic activity[45-49].

In this work, we exploit the fluorescence lifetime properties of NADH for metabolic imaging. Free NADH exists in a folded configuration. This causes quenching of the reduced nicotinamide (which is the fluorescent group) by the adenine group. On the contrary, upon binding to proteins, NADH is in extended configuration causing this quenching to decrease. Due to this self-quenching, the lifetime of free NADH is significantly lower (~0.4ns) compared to protein bound NADH[37,50]. For example, the lifetime of NADH bound to lactate dehydrogenase (LDH) is 3.4ns[51-53]. Hence the two forms can be distinguished by fluorescence lifetime imaging microscopy (FLIM). FLIM of intrinsic fluorescent NADH can serve as a powerful tool to study metabolism due to the extreme sensitivity of fluorescence lifetime to molecular conformations and the fluorophore's surrounding environment. Also, unlike intensity-based imaging, lifetime measurements are independent of concentration. Hence, NADH FLIM is extensively employed as an endogenous biomarker for metabolic imaging in cancer, stem cell differentiation.

Currently, there is a limit in deciphering the difference between NADH and NADPH. Blacker et al. stated that the relative ratios of NADH and NADPH can be determined using a mathematical calculation based on the lifetime of the bound species[54]. However, they used genetically modified cells (NAD+ kinase (NADK) was either overexpressed (NADK+) or knocked down (NADK−)) to shift the metabolic state of the cells. In their case, the relative ratios can be determined from manipulated cells. To our knowledge, there is a limitation in determining the difference between the two species. Given that the concentration of NADH is about 10 fold higher than that of NADPH[55], we expect that the major contribution of fluorescence signal comes from NADH[56]. However, it is quite possible that if levels of free or bound NADPH were changing, we would see a similar effect. Thus, for this thesis, we discuss lifetime phasors in terms of NADH.

Chapter 3

Measurements of absolute concentrations of NADH via phasor FLIM

Chapter overview: In this chapter, we describe a graphical method using the phasor representation of the fluorescence decay to derive the absolute concentration of NADH in cells. The method requires the measurement of a solution of NADH at a known concentration. The phasor representation provides a simple approach for the accounting of the differences in quantum yield of the free and bound form of NADH, pixel by pixel of an image. The concentration of NADH in every pixel in a cell is obtained after adding to each pixel in the phasor plot a given amount of unmodulated light. This operation is done mathematically or with the use of an external physical light source. After addition of a constant amount of light to the decay, the phasor at each pixel is shifted toward the origin by an amount that depends on the intensity at the pixel and the fluorescence lifetime at the pixel. The absolute concentration of NADH is obtained by comparison of the shift obtained at each pixel of an image of a cell with the shift of the calibrated solution.

3.1 Introduction

The accurate determination of the concentration of common cellular metabolites is of fundamental importance for understanding cellular metabolism and changes in metabolism due to cell cycle, stress, and neurodegenerative diseases[57-66]. In fluorescence microscopy, the measurement of the concentration of a fluorescent molecule in a cell is commonly achieved by a calibration procedure in which the fluorescence signal is measured for a known concentration of the substance in a homogeneous solution and then this signal is compared with the signal from the fluorophore in the cell. This method works when the fluorescent substance is well above any fluorescent background and when there is no change of the quantum yield of the substance from the solution used for calibration and the quantum yield of the fluorophore in the cell.

When the fluorescent substance is NADH (reduced form of the Nicotinamide adenine dinucleotide), a common and abundant co-enzyme related to metabolism found in every living system, this simple calibration procedure cannot be applied because NADH in a cell exists in at least two forms, one free, with a lifetime of approximately 0.4ns (low quantum yield) and a second form when bound to enzymes, where the quantum yield could be much higher. Unless we know the relative amount of the free and bound form of NADH in every pixel of the image, the simple calibration procedure based on comparison with the intensity of a calibrated solution cannot be applied because the quantum yield is not the same as in the solution. The lifetime of the bound form of NADH is not easy to obtain under the microscope conditions. Lifetime values reported in the literature for NADH range from 1.4 to 9 ns[46,48,50,61,65-77]. This very large range could imply that the specific protein binding NADH could strongly affect the quantum yield of NADH.

In this chapter, we propose a simple method that could resolve the issue of the two different quantum yields of NADH and could provide absolute values of the NADH concentration using a calibration with a solution of free NADH of known concentration. The proposed method makes use of the phasor representation of the fluorescence lifetime and of a graphical solution of the changes of the phasor position at each pixel of an image when we add a given amount of unmodulated light to the entire image[78]. The addition of light to the decay does not require the physical addition of light, but it can be achieved mathematically by adding a constant value to the decay at each pixel.

The proposed graphical approach could be applied to any combination of molecular species in a pixel provide the quantum yield of each species is known. Although in this chapter we describe the determination of the absolute concentration of NADH, the same approach could be applied to the determination of other substances like retinoic acid, folate, and flavins that have a different quantum yield in the cell with respect to solutions[79-81].

3.2 Materials and Methods

Cells preparation.

Chinese hamster ovary (CHO-K1) cells were cultured and maintained in a 37°C incubator humidified at 5% CO2 atmosphere in Dulbecco's modified Eagle's medium/F12(D-MEM) (1:1) (11320-033, Life Technologies, Carlsbad, CA), supplemented with 10% fetal bovine serum and 1% penicillin streptomycin. The cells were freshly trypsinized and plated onto 35 mm glass bottom dishes (Mattek Corporation, Ashland, Massachusetts) for imaging.

Microscopy.

The phasor FLIM images were acquired with LFD customized microscopy system M3 which is a modified Zeiss Axiovert S100TV microscope (Carl Zeiss, Jena, Germany) coupled with a two-photon Ti: Sapphire laser (Spectra-Physics MaiTai) and Becker&Hickl SPC-830 card (Becker and Hickl, Berlin). A Zeiss 40x1.2 NA water immersion objective (Carl Zeiss, Oberkochen, Germany) is used. The specimens were excited at 740nm and the emission signal is split with 496nm dichroic filter and detected in two channels using a band pass filter 460/40 nm and a band pass filter at 540/50-565nm for the second channel. Only the blue channel was used in this study.

Free NADH preparation. For pure free NADH FLIM calibration, NADH (Sigma N8129) were diluted in 10X Tris-HCl buffer (pH = 7.4).

Sample preparation to lifetime measurements of NADH bound to Lactate Dehydrogenase.

Powder L-Lactic Dehydrogenase (LDH) from rabbit muscle (code L1254, Sigma-Aldrich, Inc) was prepared in buffer Tris-HCl 0.2 mM, pH 7.5. Later the enzyme was cleaned for whatever contaminant using Vivaspin® 2 Centrifugal Concentrator (GE Healthcare), flowing the specification of the manufacturer we change the same buffer for 5 times. After the concentration protocol, the supernatant was centrifuged for 20 minutes at 9500 xg in order to remove precipitations. The amount of protein was determined using absorbance at 280nm with an extinction coefficient of 205000 M-1.cm-1[82] in a NanoDrop 2000 UV-Vis Spectrophotometer (Thermo Fisher Scientific Inc). A final concentration of enzyme around 22 μM was reached, the enzyme was used immediately or stored in the refrigerator at 4°C for 1 week. The β-Nicotinamide adenine dinucleotide (NADH, 10107735001 ROCHE, Sigma-Aldrich, Inc) was prepared fresh every day as stock solution of 250 μM in a Tris-HCl buffer 0.2 mM, pH 7.5, the absolute concentration of the NADH was determined to measure the absorbance of 340 nm using an extinction coefficient 6200 M-1.cm-1[82], with a Perkin-Elmer Lambda 40 spectrophotometer. Following the thermodynamically reversible equilibrium rules for the enzyme /ligand complexation[83], we determined the percentage of enzyme/ligand complex (EL) using the described dissociation constant (KD) equal to 0.2 μM (Weber) in 100 mM of the oxalic acid (75688 Sigma-Aldrich, Inc). An approximate ratio of 92.7% of EL was prepared by the incubation at room temperature for 30 min of 2.2 μM of LDH and 0.05 μM of NADH (see Equations 3,4, and 5). Consider the following equilibrium

$$\mathrm{E} + \mathrm{L} \Leftrightarrow \mathrm{EL}$$

Where E, L, and EL represent: the free enzyme, free ligand and EL complex at the equilibrium, respectively.

$$\mathrm{K}_D = \frac{[\mathrm{E}]\,[\mathrm{L}]}{[\mathrm{EL}]}$$

Using the initial concentration of the E_0 (E_0=E-E_L) and L_0 (L_0=L-E_L) and reorganizing the terms in the KD expression it is possible to obtain the following notation for the EL equilibrium concentration.

$$[EL] = \frac{(K_D + E_0 + L_0) - \sqrt{[(K_D + E_0 + L_o)^2 - 4E_0L_0]}}{2}$$

And the EL percentage as:

$$EL\% = \left(\frac{[\mathrm{EL}]}{[\mathrm{E}]}\right) * 100$$

The FLIM measurements were taken in an Olympus FluoView FV1000 system with IX81 microscope and 2-photon excitation of 740 nm using a Spectra-Physics MaiTai HP laser and Fast-FILM-box (ISS, Inc). For the NADH lifetime measurement we used a water immersion UPL SAPO Olympus objective 60x with a NA 1.2 and a filter block composed two band pass filter of 460/40 nm and 540/50 nm with a dichroic mirror 495 nm long pass filter The calibration of the system was performed using a solution of 10 ⍰M of Rhodamine 110, with a lifetime of 4.0 ns (ISS webpage at www.iss.com).

3.3 Results

3.3.1 The phasor method to determine absolute concentrations of NADH in cells

In figure 3. 1a we schematically show the principle of the method. The blue circle indicates the phasor position of free-NADH, which could be obtained experimentally as shown in Figure 3. 1 b. The phasor position of the free-NADH lies on the universal circle hence the lifetime of this species is well approximated by a single exponential. Since the fluorescence lifetime is independent on the concentration, the same phasor position is obtained from any concentration of the solution used for calibration. For ease of explanation, let us assume that the concentration we use for calibration is 1mM.

If we add a constant intensity value to the measured decay, the phasor of this unmodulated light is at the origin (Figure 3. 1, black circle). The constant intensity could be an external light source or, more conveniently, we can add a constant number to the record of the decay. In either case, we will call it “external light added”. After the phasor transformation, there is no difference if the decay was measured in the frequency domain or in the time domain using the popular TCSPC [84]. In either case the phasor of the solution of free-NADH moves toward the origin.

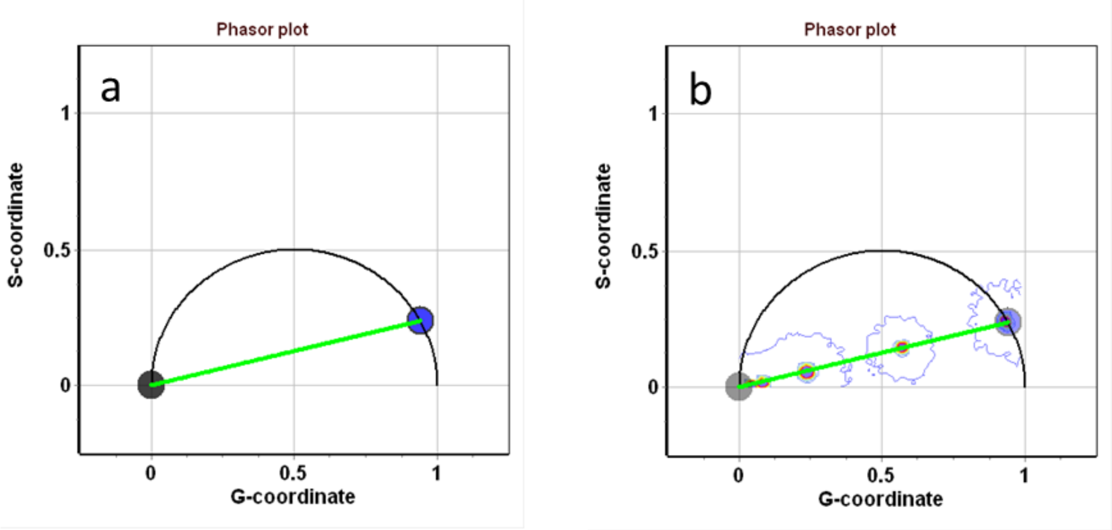

Figure 3. 1 The principle of NADH absolute concentration measurement

Figure 3. 1 a) Phasor representation of a single exponential component on the universal circle (blue circle) and a component of unmodulated light at the origin (black circle). b) The experimental value of the free-NADH lifetime (blue circle). When different amounts of unmodulated light are added to the sample, the phasor position moves towards the origin according to the rules of phasors addition. In this figure, we use a physical source of unmodulated light to shift the position of the phasor of the free-NADH. A mathematical addition of a constant to each pixel of the decay gives the same plot.

As we increase the amount of the unmodulated light added, the phasor of the free-NADH solution moves towards the origin due to the law of phasor addition, as shown experimentally in Figure 3. 1b. However, the amount of shift toward the origin depends on the concentration of the solution and of the quantum yield. Figure 3. 1b shows a series of measurement in which a solution of 1mM NADH is illuminated with an increasing amount of unmodulated light L. In this case, we actually added an external light source, but the same effect could be obtained if we “mathematically” add a constant to the measured decay. For a given amount of light added, the shift toward the origin depends on the total fluorescence of the solution of NADH we are using for calibration. Therefore, by measuring the shift for a given amount of external light added we can determine the concentration by comparison with the calibrated solution (Figure 3. 1 B). Specifically, the distance (M) of the blue circle from the origin can be expressed in terms of the external light intensity L and the amount F of fluorescence emitted by a known concentration of NADH

$$M = \frac{L}{L+F} \qquad (1)$$

The value of M, which is the modulation of the phasor in Figure 3. 1b can be measured with high precision and the ratio F/L be determined. In this chapter, we will use the projection of M on the x-axis that we call the g-coordinate, as done in most of the papers using phasors.

In Figure 3. 2 we show the experimental graph of the coordinate G calculated using the following formula

$$g = \frac{g_0}{1+\frac{F}{L}} \qquad (2)$$

Where g0 is the g-coordinate of the calibration solution without external light and the ratio F/L is obtained directly from the average of the intensity of the image as defined in Equation 1. So, the only experimental quantity we need is the intensity F of the free-NADH solution used for calibration.

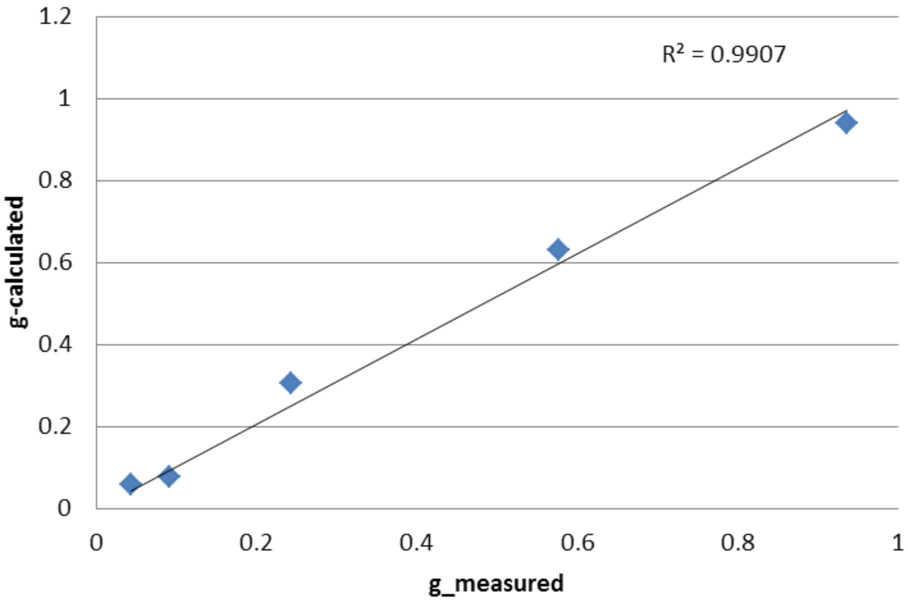

Figure 3. 2 Experimental value of free-NADH lifetime modulation with external light

Figure 3. 2 Relationship between the experimental value of the g coordinate of the phasor plot and the value of g calculated using Equation 2, for different amounts of external light L While in figure 3. 2 we show several points, only one point with "external light added" needs to be obtained along the line of calibration since the g0 value is directly measured and the calibration line must pass through the origin. This single point along the line in figure 3. 2 will be the calibration point we will use to determine the concentration of an unknown sample. Of course, the same amount of "external light added" should be used for the measurement of the unknown sample.

3.3.2 Linear combination of free and bound NADH.

In this work, we are focusing on the measurement of the absolute concentration of NADH in every pixel of an image of a cell. Specifically, we are using 2-photon excitation at 740nm and an emission filter 460/40 nm to select the emission of NADH. Previous measurements in our lab have shown that the NADH lifetime, when bound to the LDH

(Lactate DeHydrogenase) enzyme, is about 3.4ns [81,85]. For this work, we measured again the value of the NADH lifetime bound to LDH and the value found is in full agreement with previous measurements. In Figure 3. 3a, the phasor of NADH for a combination of free and bound NADH in a given pixel should fall along the green line in Figure 3. 3a from the blue (free NADH) to the red circles (bound NADH). The phasor clusters in Figure 3. 3a correspond to experimental values determined for this work using the same instrument used for all measurements reported here.

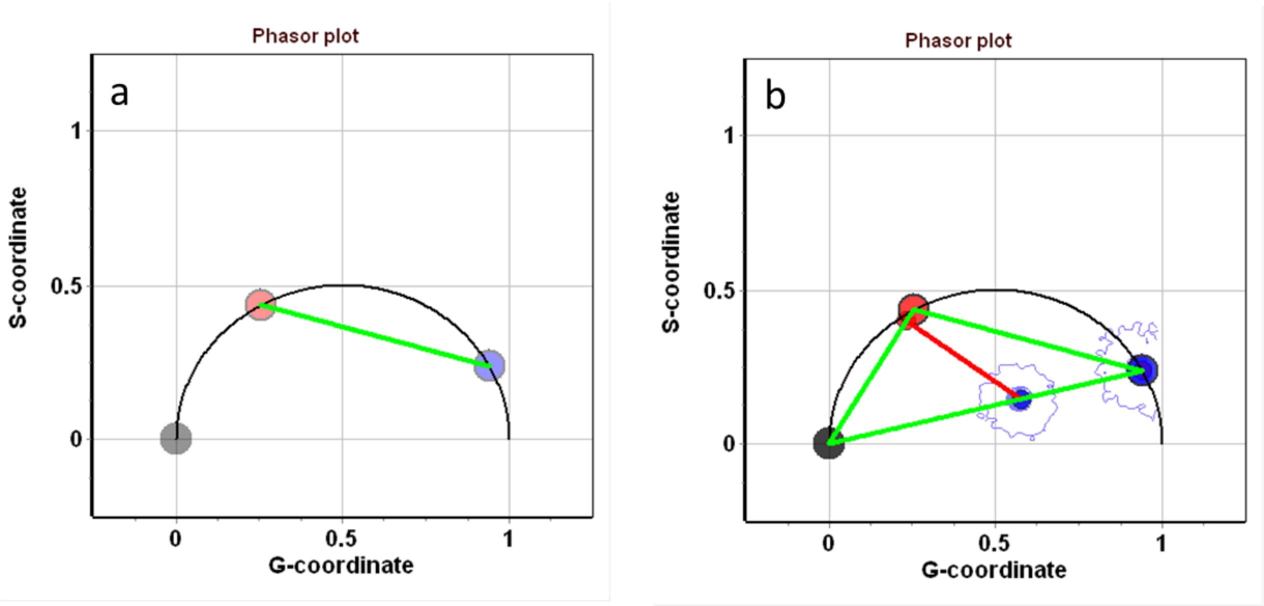

Figure 3. 3 Linear combination of free and bound NADH

Figure 3. 3 Linear combination of free and bound NADH. a) The blue and red circles indicate the phasor position for free and bound NADH, respectively. Every possible combination in a pixel of free and bound NADH will be on the green line joining the phasor of the free and bound NADH. b) Upon addition of the external light, the phasor of the free and bound NADH moves toward the origin, but in different amounts as, indicated by the red line. However, all points of the shifted red line have the same concentration equal, to the concentration of the calibration solution since the solution phasor has moved by a given amount along the line of linear combination with the phasor at the origin.

Along this line, every point represents a different linear combination of free and bound NADH. As the “external light” is added, the entire line of the linear combination will move according to the changes of position of the red and blue circles, respectively. Since the red circle represents molecules with a high quantum yield (long lifetime) while the blue circle represents molecules with a low quantum yield (short lifetime), the two points will move different amounts as shown in figure 3. 3b, red line. All points along the red line in figure 3. 3b have the same concentration which is equal to the concentration of the calibration NADH solution. However, if some pixels in the image contain a smaller amount of NADH (than the calibration solution), they will move further toward the origin than pixels where NADH is more concentrated. From this shift, we can determine the absolute NADH concentration in every pixel of the image.

3.3.3 Determining the absolute concentration of NADH in cells

Figure 3. 4a shows the endogenous fluorescence of a CHOK1 cell by photon excitation at 740 nm, with an emission filter at 460/80 nm and the corresponding phasor plot is shown in Figure 3. 4b.

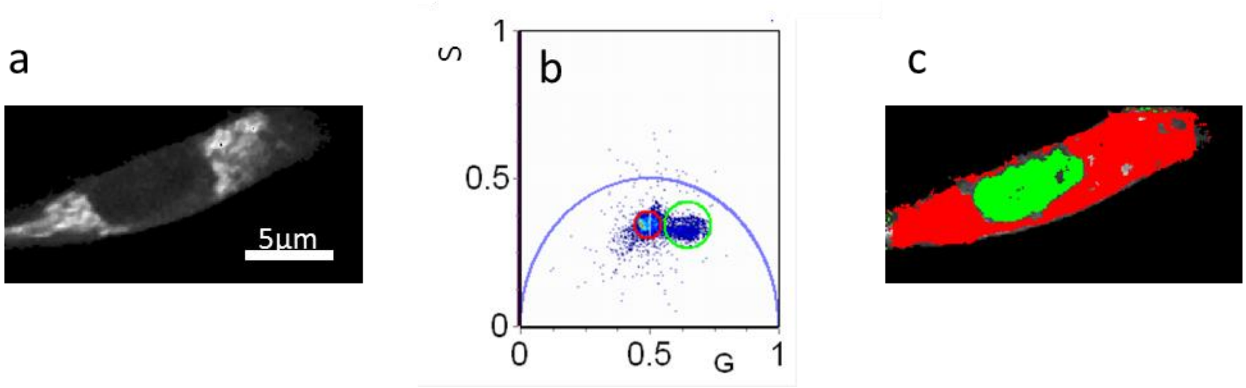

Figure 3. 4 A FLIM color-coded cell

Figure 3. 4 a) Intensity image of a CHOK1 cell in a grayscale. b) The phasor plot shows two characteristic clusters shown by the red and green cursors. c) All pixels in the red cursor are painted in red and all pixels in the green cursor are painted in green.

In the phasor plot of figure 3. 4b, there are two major clusters, one highlighted by the green cursor corresponding to shorter lifetime values in the cell nucleus and the other cluster highlighted by the red cursor with longer lifetime values and painted in red corresponding to pixels in the cytoplasm (Figure 3. 4c). However, in the cytoplasm, there are regions of equal lifetime but very different intensities (Figure 3. 4a). Based on intensity only we cannot tell if the concentration of NADH in the cytoplasm is similar in every pixel and different from the nucleus. It could be that the concentration is the same, but the quantum yield is very different in different parts of the cell.

When the external light is added to every pixel of the image, the image contrast changes (figure 3. 5a) and the entire phasor distribution moves toward the origin (figure 3.5 b). It is easy to see that some pixels move more than others toward the origin, indicating different NADH concentration in these pixels.

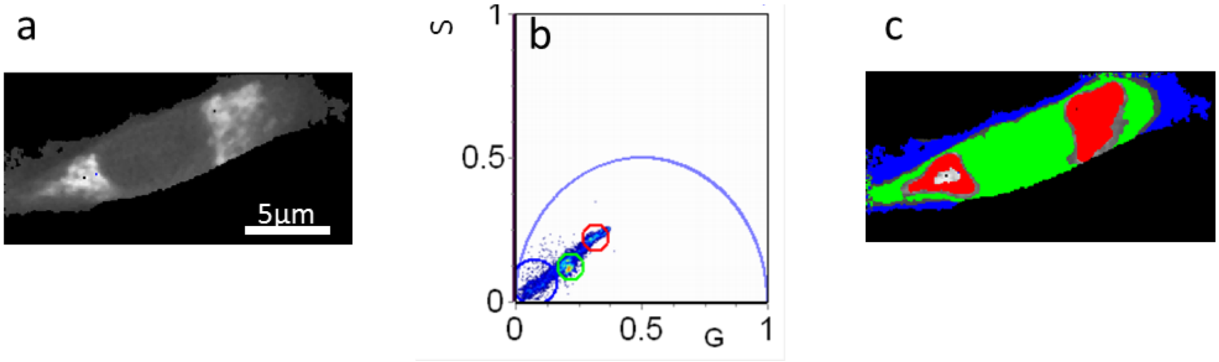

Figure 3. 5 Phasor coordinate modification with “external light” in a CHOk1 cell

Figure 3. 5 a) Same CHOk1 cell as in figure 3. 4 with external light added. Note that the contrast of the image is quite different from Figure 3. 4a. b) Comparing panels b in figures 3.4 and 3.5 we can determine that some pixels of the image have moved more than others toward the origin, indicating a different concentration of NADH in those pixels. c) Same image colored according to the cursors selected in panel b.

To obtain the NADH concentration in the various parts of the cell we use the calibrated phasor plot for a given intensity of the external light (Figure 3. 3b). In figure 3. 6 we show how to use the calibration to display the concentration of NADH of the various pixels of the image.

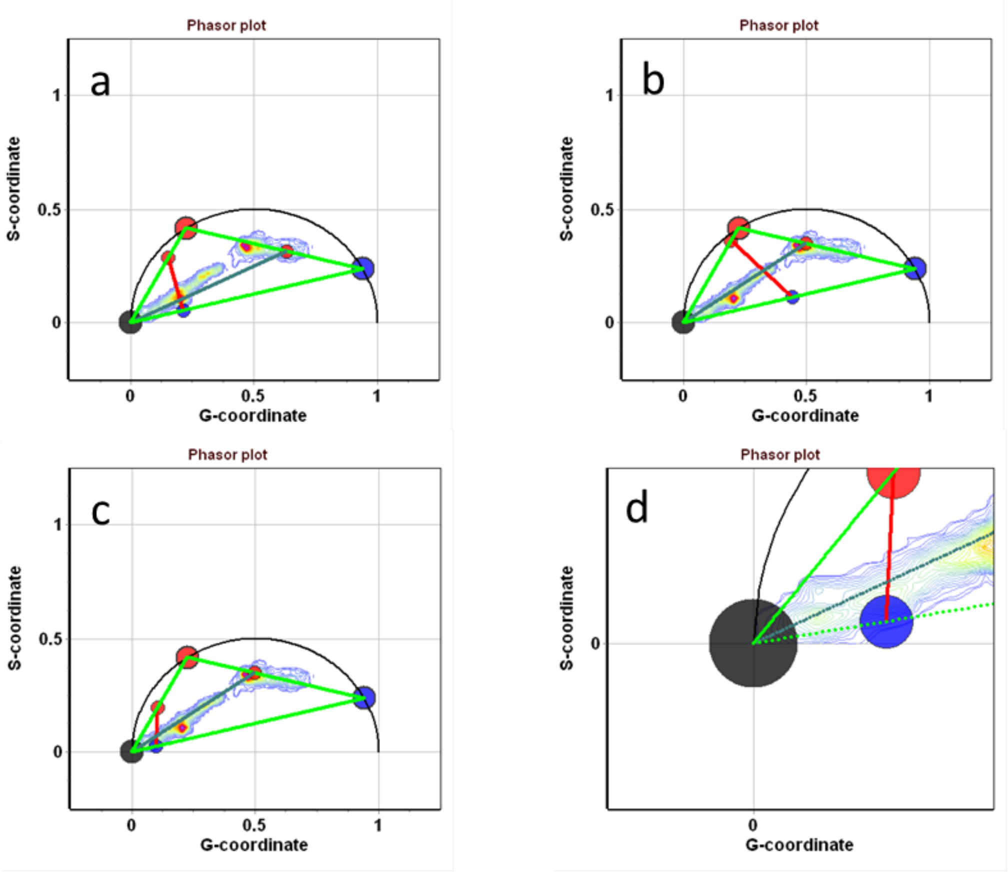

Figure 3. 6 The cell phasor plots modification with external light

Figure 3. 6 The cell phasor plots are shown in the background of each of the panels in this figure together with the phasor plot obtained with a certain amount of external light added. a) The amount of light added moves the red line to the position shown in panel a). All pixels with phasors along the red line have an equal concentration (0.295 mM). These pixels correspond to the nucleus and part of the cytoplasm of the cell as shown in figure 3. 5b Using less external light, the red line moves away from the origin. All points along this line have a concentration of 0.889mM. These points are selected by the red cursor in figure 3.5 b and they map to the brighter pixels in the cytoplasm. c) Increasing the amount of added light, the red line moves toward the origin. The pixels selected in this region of the phasor plot map to certain regions of the cytoplasm where the concentration is about 0.117mM. d) Zoomed part of panel c near the origin.

The cluster region indicated by the small red dot along the line blue-red after addition of a given amount of external light moves to the point corresponding to the intercept of the blue line with the red line. The red line position is directly proportional to the NADH concentration so that all points along the red line have the same concentration. For this position of the red line, the concentration is 0.295mM. We have already identified in figure 3. 4 that the selection of this cluster corresponds to pixels in the nucleus. Now we move the blue line to the other cluster that was identified with points in the cytoplasm. After adding the external light, this cluster moves to the position indicated by the red line in figure 3. 6b. Along this line, the NADH concentration is 0.889mM. In figure 3. 6c (zoomed in Figure 3. 6d) we show that there are other pixels, originally in the cytoplasm that move to a different position along the blue line. This position corresponds to a concentration of 0.117mM.

Finally, a simple software algorithm can paint the original image pixel by pixel using a color scale based on concentration rather than fluorescence intensity. This is shown in figure 3. 7.

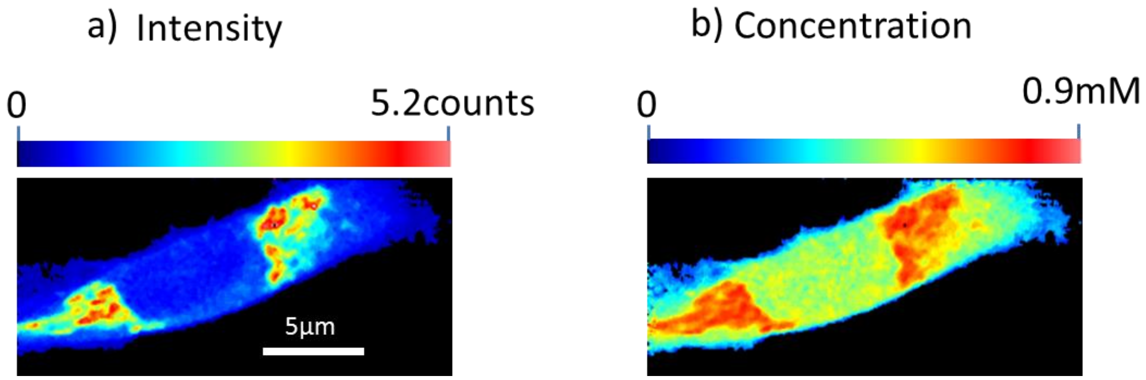

Figure 3. 7 Intensity and NADH absolute concentration color-coded cell

Figure 3. 7 a) Intensity image of NADH in a CHOK1 cell. The color scale is in counts/pixel/frame. b) NADH concentration image according to the method described in this chapter. The concentration scale was calibrated using a solution 1mM free-NADH.

3.4 Discussion

To calibrate for the absolute concentration of NADH in cells, we need a FLIM measurement of the intensity of a known solution of free-NADH done with the same illumination condition used for the cells. Once the FLIM image is obtained, the graphical method for the absolute determination of the NADH concentration is very rapid, automatic and provides accurate values of concentration as long as some assumptions are satisfied. i) The relative quantum yield of the components (free and bound NADH) must be known or it must be measured. These are the blue and red dots in figure 3. 3.ii) There are no other major contributions to the fluorescence than the assumed species. iii) The volume of exploration (the height of the confocal slice) must be uniform across the sample.

In the case of NADH, the quantum yield could be assumed to be proportional to the lifetime of the two states (bound and free) so that they can be determined by independent measurement. As discussed in the Introduction, the phasor position of free-NADH is easy to measure. For the bound NADH, the phasor position could be obtained from the experimental data by extrapolation of the line passing through the experimental points and through the point on the universal circle for the free-NADH. In the case of an unknown compound, we could calibrate the “brightness” with a substance of known quantum yield and then use the same calibrated amount of external light to record the change in position in the phasor plot.

The graphical procedure discussed in this work could be applied to unknown samples. Consider the following situation: two fluorescent proteins have the same lifetime, which is frequently the case, so that they will be on the same spot on the universal circle in the phasor plot. If the two proteins have different brightness when we add the external light, they will move a different amount toward the origin. From the shift amount, we could determine their relative brightness. If we know the concentration, we can determine the relative quantum yield.

When collecting a FLIM image, we are measuring the lifetime at each pixel. If there are other substances and they contribute differently in different regions of the cell, then we should be able to separate the contribution of additional species and build a graphical analysis model for 3 components instead of the two-component model used here. Note that the experimental values of the fluorescence lifetime in the cell (figure 3. 6) align along the line between free and bound NADH. In the specific example discussed in this work presumably, we only have a mixture of 2 components in each pixel. This is not always the case and in many experiments of cell endogenous fluorescence using the same excitation and emission filters used in this work we observe pixels that are not along the line of a linear combination of free and bound NADH [85].

The requirement of the equal volume of excitation only applies to the concentration calculation. For example, in a thin lamella of a cell, the volume of excitation could be a small section of the cell. In this case, what we are measuring is the number of molecules in the layer rather than the concentration.

Can this method work with time domain fluorescence decay data without using the phasor transformation? Theoretically yes. However, for every pixel, we need to resolve for two (or more) exponential components and the background contribution. We have a total of 2 lifetimes (which presumably are known), 2-preexponential factors and the background term. This analysis can be difficult to perform because a small shift in the lifetime values could have a large effect on the pre-exponential factors.

We note that the only equations used for this work are the equations for the linear combination of lifetime components (phasors) in the phasor plot (Equations 1 and 2). A user interface for the calculation of absolute concentrations of NADH in cells is available in the SimFCS software at www.lfd.uci.edu\software.

Chapter 4

Non-invasive live imaging of stem cell signature metabolic states

Chapter overview: In this chapter, we demonstrated using the combination of two-photon fluorescence lifetime imaging (FLIM) and hyperspectral imaging technique to monitor the metabolic states of human embryonic stem cells (hESCs) and study their response with different growth factors such as WNT3A, BMP4, etc. We have exploited the cell phasor approach to detect a trend in the human embryonic stem cells as well as mouse post-implantation embryos with endogenous WNT and BMP4 signal. The cell phasor approach to lifetime imaging provides a label-free, fit-free, and sensitive method to identify different metabolic states of cells during differentiation, to sense small changes in the redox state of cells, and may identify symmetric and asymmetric divisions and predict cell fate. Our method is a promising noninvasive optical tool for monitoring metabolic pathways during differentiation or disease progression, and for cell sorting in unlabeled tissues. And this method can be used to understand heterogeneity in hESCs cultures, how that metabolic heterogeneity is affected by culture conditions, how it affects cell fate decisions and if it reflects conditions in developing embryos which can be further used for diagnosis and drug screening for targeted therapy in the future.

4.1 Introduction

A growing body of evidence suggests that stem cells and their progeny exhibit unique metabolic states along a continuum of oxidative phosphorylation and glycolysis[86-88].

Theoretically, differences in these states could be used to distinguish stem cells from differentiated daughters and from surrounding niche cells. Such a method could be used to study the normal biology of stem cells and their behavior in aberrant conditions such as cancer.

But current methods of analyzing cell metabolism utilize technologies that involve biochemistry on extracts from large numbers of cells or use reporter cell lines or dyes, with the inherent problems associated with such invasive technologies[89,90]. Therefore, a major challenge in the stem cell field whether studying pluripotent stem cells or adult stem cells is how to study metabolic state at the molecular level in single living cells. This difficulty is especially critical in studying human tissues where transgenics or other types of genetically embedded reporters are impossible or risky. New technologies to detect precise, molecular changes in primary human cultures or tissues without any molecular markers or invasive manipulation would be transformative.

In this chapter, we propose that different metabolic states can be distinguished from each other using a non-invasive, label-free imaging technique that we have pioneered[62,91,92]. To follow changes in the metabolic state of differentiating stem cells, we propose to use a state-of-the-art microscopy technique called the phasor approach to fluorescence lifetime imaging microscopy (FLIM). FLIM utilizes two-photon microscopy and allows for label-free detection of molecules that are intrinsically endogenous fluorescent when activated by specific wavelengths of light. FLIM is powerful because it enables real-time, non-invasive monitoring of unlabeled cells in culture or in living tissues[80]. In our previous studies, FLIM was used to monitor the metabolic coenzyme nicotinamide adenine dinucleotide (NADH), the principal electron acceptor in glycolysis and a major electron donor in oxidative phosphorylation. NADH is detected via its endogenous fluorescence (740nm excitation), a fluorescence that decays differently (lifetime) in a glycolytic versus a respiring environment (oxidative phosphorylation). Emission filters (460-480nm) are used to detect NADH endogenous fluorescence specifically by filtering out contributions from other intrinsically endogenous fluorescent species. NADH FLIM signatures are therefore especially powerful as they provide a rapid, specific, and sensitive readout of the metabolic status of individual cells within their native microenvironment[62,63,65]. Such methods could be used to understand heterogeneity in human embryonic stem cell (hESC) cultures, how that metabolic heterogeneity is affected by culture conditions, how it affects cell fate decisions and if it reflects conditions in developing embryos. Our group has shown that the NADH signature in living stem cells in the hermaphrodite gonad of C. elegans, or in living stem cells in the mouse intestinal crypt indicate strong glycolysis and are distinctly detected by FLIM[62,91,93]. If hESCs could be induced to differentiate more efficiently with or without growth factors such as Wnt, it would resolve a major roadblock to high-efficiency specialized cell production and reduce costs of cell-based therapies. If metabolic signatures seen in hESCs closely match those seen in the developing embryo, hESCs could be used to help predict risks to the developing embryo. In adult tissues such methods could allow detection of metabolic, pre-cancerous changes in cells, allowing earlier disease diagnoses (e.g. colon cancer). In this chapter, we have developed FLIM as a method to monitor the metabolic state of stem cells and post-implantation mouse embryos. We suggest that methods that evaluate stem cell populations on a shorter time frame are more amenable for practical use in regenerative medicine and disease diagnosis. Another feature that makes FLIM an exciting, powerful approach is that it is amenable to analyzing the heterogeneity of cultures – detecting metabolites such as NADH on a cell-cell, and even pixel-pixel basis. FLIM is a sensitive method; non-invasive and does not interfere with the biology of the cells in culture or in tissues[81]. Collectively, these features are impossible with current methods and groundbreaking.

4.2 Materials and methods

hESC Culture

Human embryonic stem cell (hESC) line H9 was grown on a feeder-free culture system with Matrigel Growth Factor Reduced (Corning) and maintained with TeSR-E8 (StemCell Technologies) medium. For general maintenance and propagation, hESCs were passaged every 5-6 days using ReLeSR (StemCell Technologies). Culture plates were coated with Matrigel at a concentration of 0.5mg/ml for 24 hours at room temperature prior to passaging. Cells were fed with 2ml of TeSR-E8 per well of a 6-well plate every twenty-four hours.

For hESCs that were cultured for FLIM imaging, cells were cultured on 35mm glass bottom dishes (Matek). Glass bottom dishes were coated with Matrigel at 0.5mg/ml for 24 hours at room temperature prior to passaging. Cells were single-cell passaged at a 1:48 dilution via

ReLeSR and mechanical cell straining with the addition of 5mM of ROCK Inhibitor (Y-27632) in order to facilitate single-cell survival. After the first 24 hours, media was replaced with TeSR-E8 without any ROCK inhibitor. 48 hours after passaging, cells in the experimental group were replaced with TeSR-E8 media containing 100ng/ml of BMP4 (R&D Systems), 100ng/ml WNT3A (R&D Systems), and 1uM of IWP2 (Tocris). Control groups were maintained with TeSR-E8 without any growth factors. Treatment with these growth factors ensued for 96 hours prior to FLIM imaging.

Immunofluorescence Staining

For immunofluorescence staining analysis, hESCs were grown on 18mm glass slips in a 12-well culture plate. Cells were fixed in 4% paraformaldehyde for 10 minutes, followed by three 5minute washes in PBS. Cells were then permeabilized in 0.3% Triton X-100 in PBS for 5-minutes, followed by another three 5-minute washes in PBS. Cells were then blocked in 10% donkey serum and 5% BSA for 1 hour. All fixing, permeabilization, blocking and washes were done at room temperature. After 1 hour of blocking, cells were incubated in primary antibodies at a concentration of 1:100 in 1% BSA at 4°C overnight. After the primary incubation, cells were washed in PBS three times for 5 minutes each. Cells were then incubated in secondary antibodies at a concentration of 1:1000 for 2 hours at room temperature and protected from light. Following secondary incubation, three 5 minutes washes with PBS prior to incubating in Hoechst at a concentration of 1:5000 for 1 minute and a final three 5-minute wash with PBS. Glass slips were gently removed from the 12-well plate and mounted on a glass slide with Vectashield and sealed with nail polish.

Primary Antibodies used here: Ab76541, Rabbit mAb to CDX2 (abcam), Sc-8628, Goat Polyclonal IgG to OCT4 (Santa Cruz Biotechnology).

Secondary Antibodies are Alexa Fluor 488 Donkey anti-rabbit IgG (Invitrogen) and Alexa Fluor 568 Donkey anti-goat IgG (Invitrogen).

4.3 Results

4.3.1 Phasor Cluster Analysis Identify the Changes in growth factor-treated hESCs

The phasor transformation of FLIM images of a living tissue directly provides maps of individual tissue components without prior assumption on the number of species in the tissues[80,94]. The analysis of the FLIM data in the phasor space is performed by detecting clusters of pixel values in specific regions of the phasor plot. Fig. 4. 1 displays the hESCs signature shift to shorter lifetime with the growth factors treatment. Previously we have found that the WNT signaling pathway is one of the earliest signaling pathways affected when hESCs begin to differentiate and that BMP4 is a key regulator of that pathway. Therefore, we exposed cells to BMP4 or to WNT3A and examined the NADH FLIM signature. Cells that were untreated had a FLIM signature in which much of the NADH indicated states of active oxidative phosphorylation (Bound NADH, Cyan, Fig. 4. 1). Cells treated with BMP4 exhibited significant, but modest and heterogeneous changes in NADH both in the cytoplasm and the nucleus. Cells treated with WNT3A showed marked changes in the FLIM signature, alterations that indicated shifts in metabolism toward greater use of glycolysis. However, the most striking changes occurred in response to simultaneous treatment with BMP4 and Wnt3a. In this case, there was a clear shift in the NADH signature in the cytoplasm to free NADH (glycolysis indications). The NADH signature was also more homogeneous (see panel C, Fig. 4. 1) and significant. These data suggest that a major influence of the metabolic state of hESCs is the WNT signaling pathway. These studies demonstrate the ability FLIM to carry out the metabolism information of hESCs.

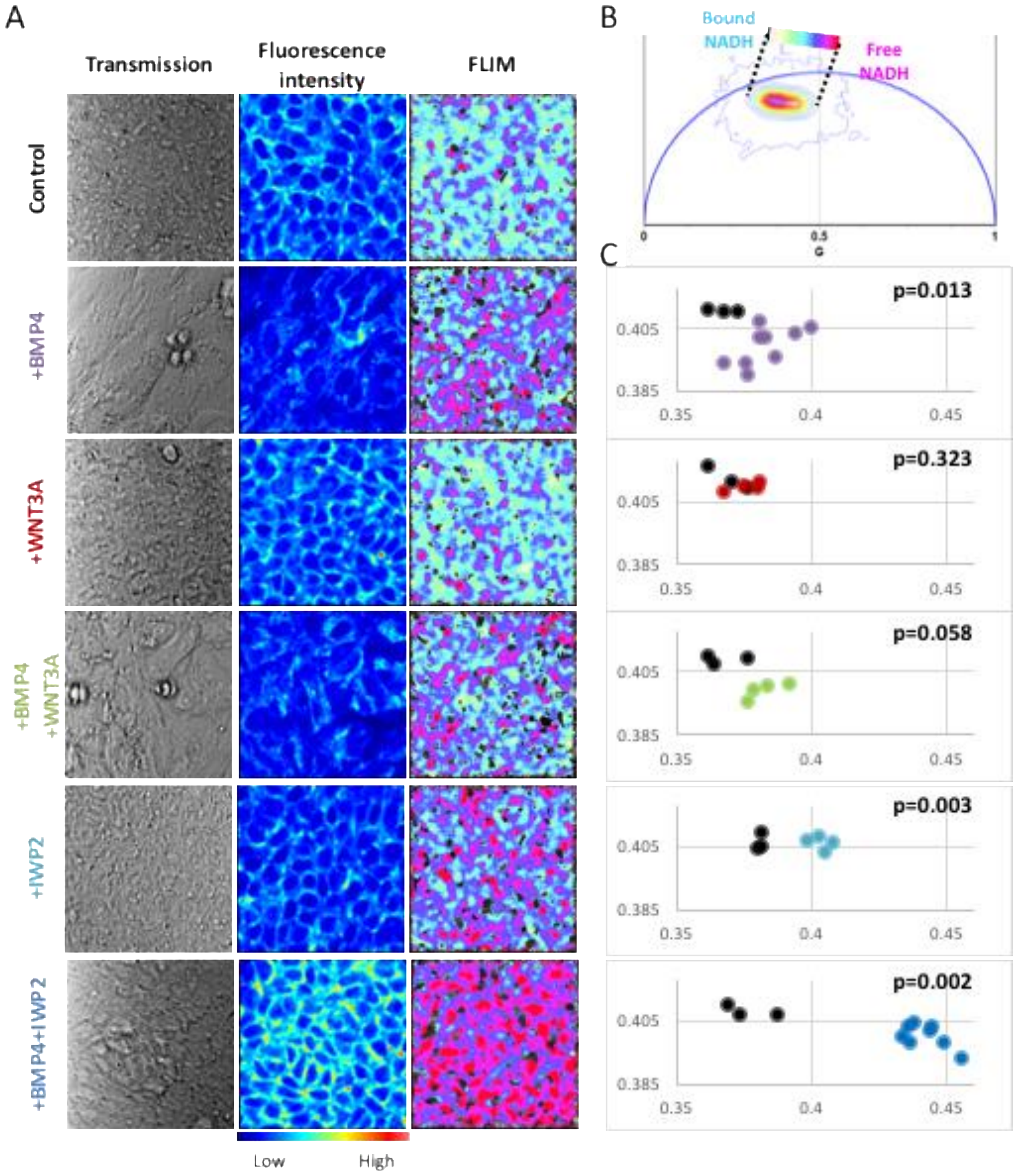

Figure 4. 1 FLIM signature changes within hESCs after growth factor treatment

Figure 4. 1 Fluorescence Lifetime Imaging Microscopy of hESCs detects a shift to glycolysis with BMP4 and WNT3A treatment. A) hESCs culture (H9; in E8 media), were treated with BMP4 (100ng/ml), WNT3A (100ng/ml), BMP4 (100ng/ml) and WNT3A (100ng/ml), IWP2 (100mg/ml), BMP4 (100ng/ml) and IWP2 (100ng/ml) for 96 hours. FLIM analysis was performed on live cultures, using 740nm to excite endogenous NADH fluorescence. Decay lifetimes of the endogenous fluorescence were captured at 40x (1.2NA). The pattern of decay of the NADH fluorescence was color mapped to each pixel of each image according to the Phasor plot color spectrum (panel B). Digital zooms of captured signals show subcellular features of NADH signals (middle). B) Phasor plot analysis showing the distribution of fluorescent lifetimes of NADH for all six conditions. Lifetimes are assigned colors on a spectrum from bound NADH (cyan; indicative of oxidative phosphorylation and most obvious in the cytoplasm) to free NADH (pink; indicating glycolysis) and are used for color mapping the images in panel A. C) Scatter plots for each condition are shown where each point on the plot - Control (black), BMP4 (red), Wnt4a (yellow) and BMP4+Wnt3a (blue) - is the average position of NADH BMP4 and Wnt3a each cause a significant shift in the distribution of NADH fluorescence in the population (p- values shown), the combination of BMP4+IWP2 triggers the most significant and homogeneous shift of NADH fluorescence towards a strong glycolytic signature. In the plot, the x-axis is the g coordinate, the y-axis is the s coordinate. The experiment has been scientifically repeated three times, each experiment shows a similar trend.

4.3.2 Metabolism inhibition studies reveal the GLY and OXPHOS

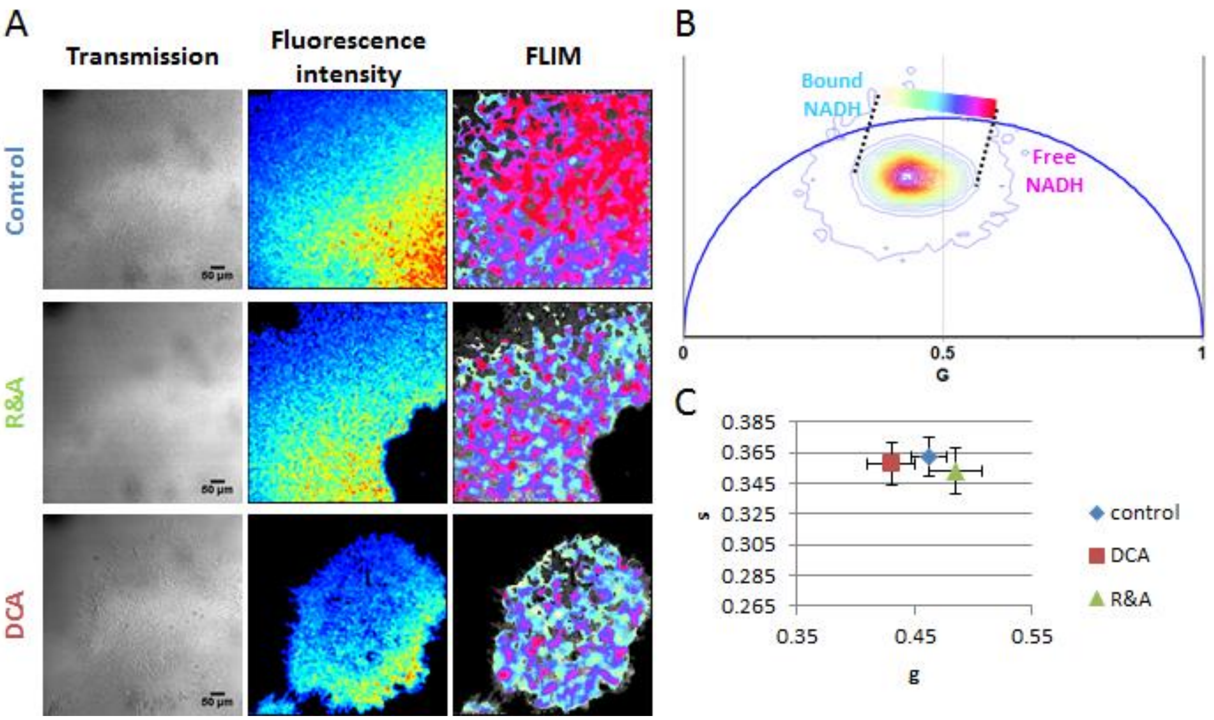

Figure 4. 2 FLIM analysis of human embryonic stem cells with metabolic alteration

Figure 4. 2 Fluorescence Lifetime Imaging Microscopy of hESCs detects the shift due to metabolic modification. A) hESCs culture (H9; in E8 media), were treated with R&A and DCA. FLIM analysis was performed on live cultures, using 740nm to excite endogenous NADH fluorescence. Decay lifetimes of the endogenous fluorescence were captured at 20x (0.8 NA). The pattern of decay of the NADH fluorescence was color mapped to each pixel of each image according to the Phasor plot color spectrum (panel B). B) Phasor plot analysis showing the distribution of fluorescent lifetimes of NADH for all three conditions. Lifetimes are assigned colors on a spectrum from bound NADH (cyan; indicative of oxidative phosphorylation and most obvious in the cytoplasm) to free NADH (pink; indicating glycolysis) and are used for color mapping the images in panel A. C. Scatter plots for each condition are shown where each point on the plot - Control (blue, n=110), DCA (red, n=66), and R&A (green, n=89). The scatters are the average position of each treatment and the error bar shows the standard deviation. Both DCA and R&A cause a significant shift in the distribution of NADH fluorescence in the population (for DCA group g coordinate, p-value=5.07E-19, for R&A group g coordinate, p-value=5.53E-14). The experiment has been scientifically repeated three times, each experiment shows a similar trend.

Given that we proposed that the major components responsible for the phasor-FLIM signature shifts are due to the intracellular NADH changes based on its fundamental role in energy production during the effect with growth factor treatment, we compared the effects of dnLEF/TCF to dichloroacetate (DCA), a well-known small molecule inhibitor of PDK1 (Whitehouse et al, 1974). A 6-h treatment of 100 mM DCA led to the same characteristic shift in the phasor plot toward bound NADH that was seen with expression of dnLEF/TCF, again indicating a decrease in a glycolytic phenotype (Figure 4. 2). We also inhibited complex I and complex III of the electron transport chain with a cocktail of rotenone and antimycin A (R&A) (50nM) for 10 minutes. The FLIM images showed increased fractional contributions of free NADH (shorter lifetimes) when compared to controls (Figure. 4. 2). This shift towards glycolytic metabolism indicates that embryos cultured in R&A have decreased oxidative phosphorylation activity. Thus, we conclude that the phasor FLIM signature we identified within hESCs is partially due to the energy metabolism alteration between oxidative phosphorylation and glycolysis.

4.3.3 Immunostaining results confirm the differentiation induced by growth factors

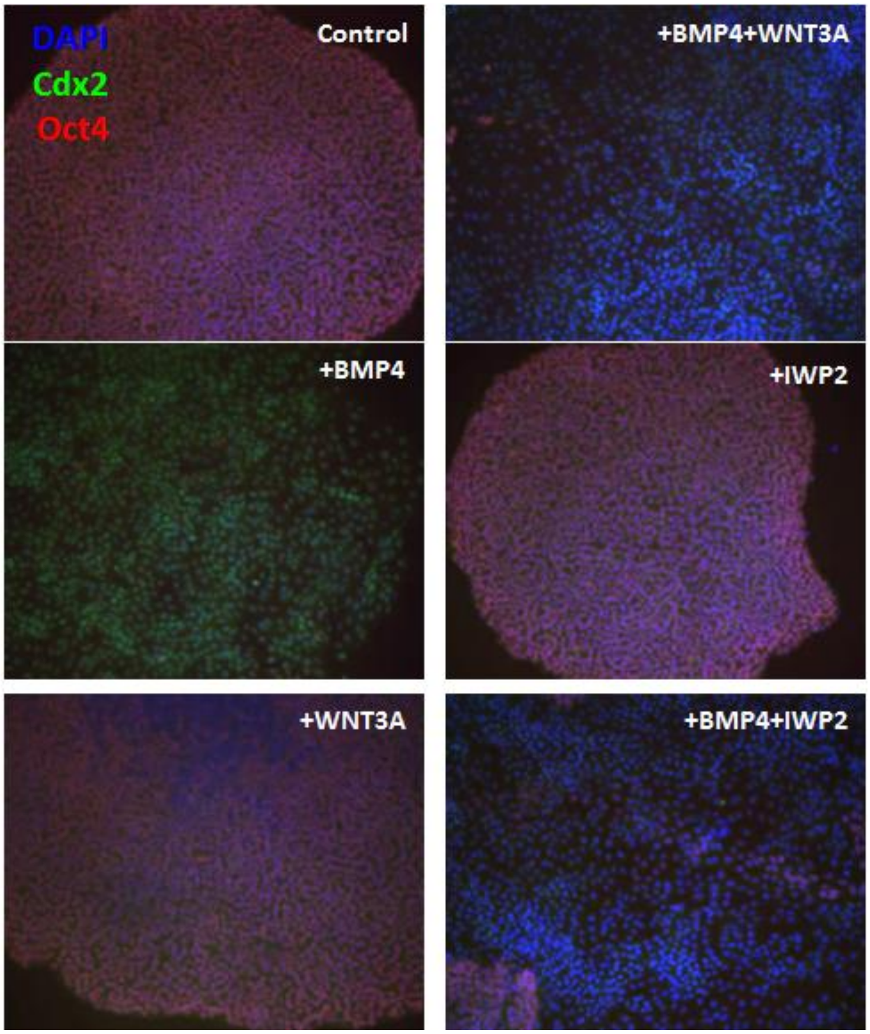

Figure 4. 3 H9 cells immunostaining with DAPI, Cdx2, and Oct4

Figure 4. 3 H9 cells immunostaining with DAPI (blue), Cdx2 (green), and Oct4 (red).

The CDX2 is supposed to stain for cells that have started differentiated into mesendoderm lineage and are no longer pluripotent stem cells. In figure 4. 3, the three groups that have positive CDX2 staining are BMP4, BMP4+IWP2, and BMP4+WNT3A;

indicating that the cells from these group have differentiated. Additionally, the co-staining of OCT4 for those three groups, the areas that are positive CDX2 staining, there is negative OCT4 staining (a marker for hESC pluripotency). And the WNT3A groups did not show any discriminate signal for differentiation which matches the results we got from FLIM study (Figure 4. 1). There is no difference between control and Wnt3A group.

4.3.4 Hyperspectral imaging technique can serve as a novel technique to identify endogenous fluorescent modification with growth factor treatment and metabolism alteration

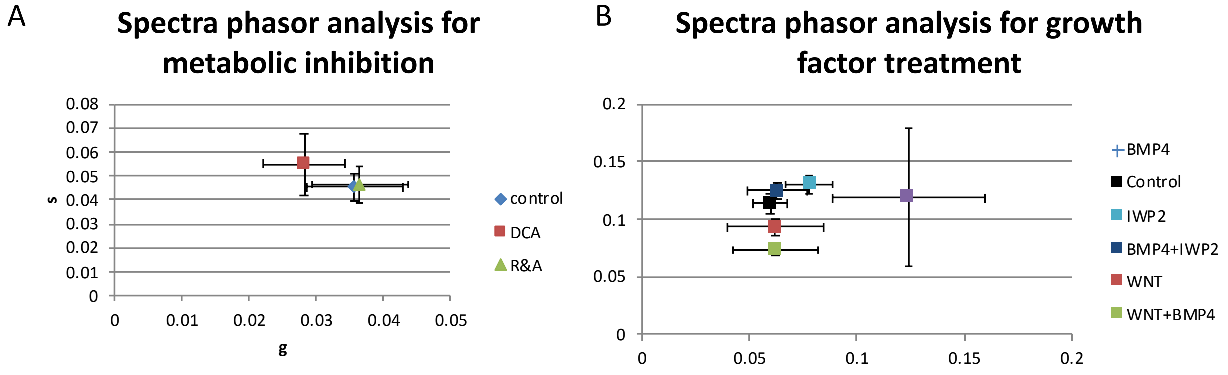

Figure 4. 4 Hyperspectral imaging reveals differentiation activity

Figure 4. 4 Hyperspectral imaging reveals differentiation activity with growth factor treatment. A) Hyperspectral imaging with hESCs detects the shift due to metabolic modification. hESCs culture (H9; in E8 media, n=141), were treated with R&A (n=68) and DCA (n=44). The scatter shows the average hyperspectral phasor coordinates. (for DCA group, p-value=2.93E-12, for R&A group, p-value=9.53E-11) B) Hyperspectral imaging of hESCs detects a shift to glycolysis with BMP4 and WNT3A treatment. hESCs culture (H9; in E8 media, n=30), were treated with BMP4 (100ng/ml) (n=50), WNT3A (100ng/ml) (n=30), BMP4 (100ng/ml) and WNT3A (100ng/ml) (n=30), IWP2 (100mg/ml) (n=30), BMP4 (100ng/ml) and IWP2 (100ng/ml) (n=30) for 96 hours. (p-value for the g coordinate, for BMP4 group, p-value=8.79E-10, for WNT3A group, p-value=0.24, for BMP4+WNT3A group,

p-value=0.17, for IWP2 group, p-value=1.01E-11, for BMP4 and IWP2 group, p-value=0.13). In the plot, the x-axis is the g coordinate, the y-axis is the s coordinate.

Currently, hyperspectral imaging has largely improved for the sensitivity of weak fluorescence detection with both hardware and software improvement. Thus, we also performed hyperspectral imaging in parallel with FLIM acquisition (Section 4.3.1 and 4.3.2), as shown in figure 4. 4. The peak of each emission spectra is represented by the position of the wavelength emitted. We found the emission spectrum of the endogenous fluorophore can also be used to read the metabolism information and identify the difference between the human embryonic stem cell colonies with different inhibition treatment and growth factor treatment. In comparison to the FLIM-phasor approach, this new method of data acquisition and analysis is able to distinguish many other endogenous fluorescence biomarkers which may be cut off by the FLIM approach where emission bandpass filters are applied. Collectively, hyperspectral imaging can be a novel diagnostic tool for the fast, non-invasive tool for metabolic information collection for stem cells.

4.3.5 Post-implantation embryo signature matches the hESCs with growth factor

In this section, we investigate the metabolic changes occurring during the gastrulation stage of mouse embryogenesis. Previous literature shows the mouse egg cylinder epiblast at E6.25 consists of an elongated cup-shaped epiblast, with trophectoderm-derived extraembryonic ectoderm (ExE) sitting on top; both are surrounded by the VE including the specialized signaling region called the anterior VE (AVE). Bone morphogenetic protein

4(BMP4) from the ExE, together with WNT3 from the posterior VE in the posterior epiblast before primitive streak formation[95]. Compare to the BMP4 and WNT3A gradient started at a higher level for posterior side toward the anterior side, from the left side of figure 4. 5, the AVE has longer lifetime than the PE side (right) with more pinkish color with higher amounts of free NADH (emphasizing glycolysis). Importantly, this cell-to-cell heterogeneity changes with the higher amount of BMP4 and WNT has shown in figure 4. 1 as well, which indicates that metabolic states of cells are not uniform and can differ strongly within one-cell distances. These data also indicate our ability to carry out FLIM on living mouse embryos.

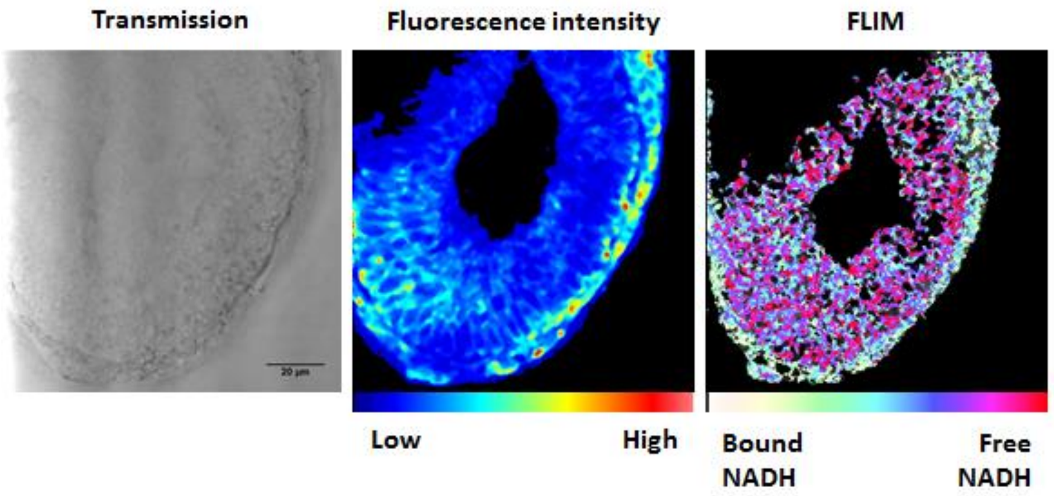

Figure 4. 5 E6.25 embryo highlights a unique metabolic pattern

Figure 4. 5 The transmission image and the fluorescence intensity image of endogenous NADH fluorescence, and the corresponding FLIM map of 740nm excitation of free NADH and bound NADH color mapped according to the phasor plot color spectrum (more cyan color indicates higher bound NADH ratio, pink color indicates higher free NADH ratio.). From left to right indicate the anterior visceral endoderm to posterior visceral endoderm. The anterior visceral endoderm (left) shows highly bound NADH FLIM signature potentially due to the gradient of BMP4 and WNT3A from posterior visceral endoderm.

4.3.6 FLIM can be used to identify the heterogeneity of differentiation

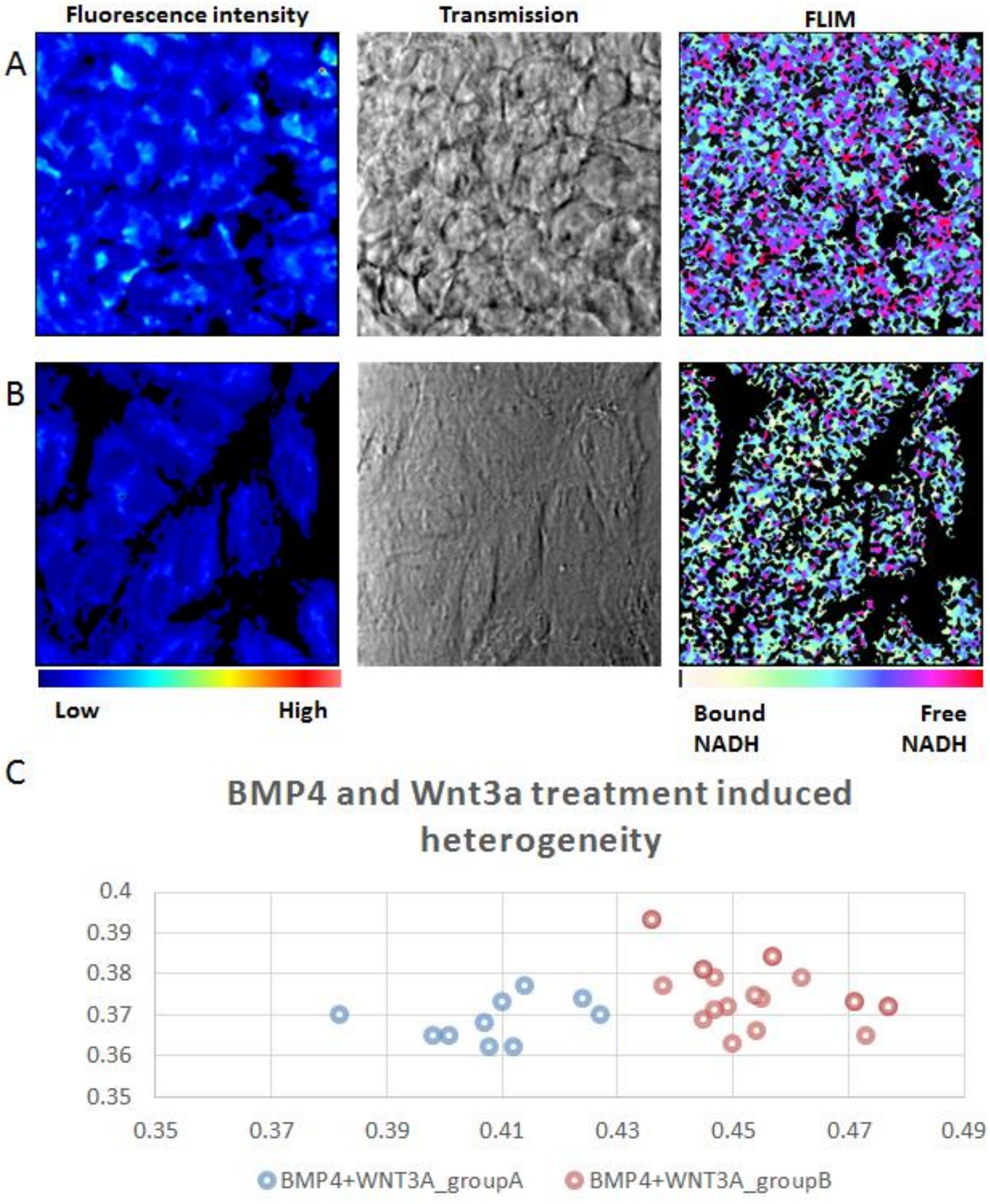

Figure 4. 6 FLIM reveals stem cell heterogeneity with growth factor treatment

Figure 4. 6 A-B) Two H9 colonies identified from the same imaging dish. (left column, fluorescent intensity image with 740nm excitation, middle column, transmission image, right column, FLIM color-coded map) C) Scatter plot shows the difference between two colonies with the same BMP4 and WNT3A treatment. Each scatter shows the average phasor coordinates of one cell. Blue scatters show the results from group A, the red ones reveal the pattern from group B. In the plot, the x-axis is the g coordinate, the y-axis is the s coordinate.

Within the BMP4 and Wnt3a cocktail 96-hour treatment group, we have found two different FLIM signatures from the same imaging dish as shown in Figure 4. 6. Figure 4. 6A and B shows the fluorescence intensity image indicate the concentration of the endogenous biomarkers which has been proved in section 4.3.2 mainly from NADH activity, transmission image, and FLIM image. The pseudo color indicates the group with longer lifetime (more bound NADH) has longer lifetime with cyan. On the other hand, the shorter lifetime indicates by pink color. The stem cell colonies from group A displays a longer lifetime than the ones from group B. The scatter plot from figure 4. 6C can also show that.

Berge group has reported BMP4 induces both trophoblast and, mediated by endogenous or induced WNTs, primitive streak differentiation rises[96-98]. In the presence of WNT inhibitors, BMP4 induces only trophoblast and no primitive streak lineages. Thus, we hypothesis here for the heterogeneity happens with BMP4 and WNT3A double inhibitor treatment, 1) the shorter lifetime signature is from trophoblast differentiation and the longer lifetime signature is from primitive streak lineages. 2) The differentiation level correlates with the FLIM signature. Hypothesis 1 and 2 can happen simultaneously.

To prove our hypothesis, we can perform immunostaining experiment next using mesendoderm markers (EOMES, LHX1, CER1) to confirm increased Brachyury expression and the primitive streak differentiation in parallel with FLIM imaging for the same stem cell colony. To confirm the differentiation level, we can perform pluripotency staining with OCT4 coupled with FLIM at the single colony level. And we can compare the pluripotency decreasing with the FLIM signature.

4.4 Chapter summary

The germline transmits genetic information, epigenetic modifications and cytoplasmic components from one generation to the next. In this chapter, we find phasor-FLIM is a sensitive, non-invasive tool to detect stem cell and post-implantation metabolism, heterogeneity, differentiation happens at single cell level in real time. This approach could provide important insight into the signaling pathways and regulatory networks, which are involved in cell self-renewal differentiation and oncogenesis in a variety of tissue and organs. The ability to observe and isolate cancer cells and stem cells noninvasively based on their metabolic state in living tissues has important implications for early diagnosis and new therapeutic strategies. Label-free discrimination between different response/differentiation with growth factor by a phasor approach to FLIM would be suitable to noninvasively monitor embryonic stem cells and to design new approaches to reprogram somatic cells to a pluripotent stem-cell fate. For example, the human embryonic stem cell with IWP2 treatment can maintain more glycolysis as well as less undesired lineages which could be used to maintain pluripotency in the future. The finding connects the in vivo epiblast signature gradient and the in vitro human embryonic stem cell signature can be used to generate a model for artificial embryo modulation to understand the gastrulation and contribute to organ engineering in the future[99-101]. The phasor approach to FLIM could be of interest to label-free cell sorting and high-throughput screening for drug discovery, cell replacement therapies, and tissue engineering.

Chapter 5

Pre-implantation embryo quality by the phasor-FLIM approach

Chapter overview: Development of quantitative, safe and rapid techniques for assessing embryo quality provides significant advances in Assisted Reproductive Technologies (ART). Instead of assessing the embryo quality by the standard morphologic evaluation, we apply the phasor-FLIM (Fluorescence Lifetime Imaging Microscopy) method to capture endogenous fluorescent biomarkers of pre-implantation embryos as a non-morphological caliber for embryo quality. Here, we identify the unique spectroscopic trajectories at different stages of mouse pre-implantation development, which is referred to as the developmental, or “D-trajectory”, that consists of fluorescence lifetime from different stages of mouse pre-implantation embryos. The D-trajectory correlates with intrinsic fluorescent species from a distinctive energy metabolism and oxidized lipids, as seen with Third Harmonic Generation (THG) that changes over time. In addition, we have defined a non-morphological Embryo Viability Index (EVI) to distinguish pre-implantation embryo quality using the Distance Analysis, a machine learning algorithm to process the fluorescence lifetime distribution patterns. We show that the phasor-FLIM approach provides a much-needed non-invasive quantitative technology for identifying healthy embryos at the early compaction stage with 86% accuracy. This may increase embryo implantation success for *in vitro* fertilization clinics.

5.1 Introduction

Determining embryo quality during *in vitro* fertilization (IVF) is one of the most important steps toward successful pregnancy[102]. The standard non-invasive method to assess embryo quality and viability relies on the visual inspection of embryo morphology according to predefined criteria such as cell division patterns, the number of pronucleoli in cleavage stages[103,104], and the physical characteristics of the blastocyst[105]. Assisted reproduction through morphological evaluation is labor intensive and highly dependent on the performance of individual physicians trained in these techniques. Development of more quantitative and objective means for assessing embryo quality that is simpler, safer, and faster could provide significant advantages in assisted reproduction by enabling single embryo transfers rather than the implantation of multiple embryos in order to increase the likelihood of a successful pregnancy.

Given the limitations of morphological evaluation, several technologies have been explored for the assessment of embryo viability. These include the measurement of metabolites in embryonic culture media, as well as genomic and proteomic profiling of the embryos themselves[106]. For example, spectroscopic approaches have been utilized to measure the number of metabolites such as pyruvate, lactate, and glucose in the media during embryo culture[107,108]. However, these approaches are time-consuming and require highly-trained personnel to analyze the complex data[109]. Both genomic and proteomic profiling are equally time consuming and can cause damage to the embryo during the procedure. Here, we apply the phasor-fluorescence lifetime imaging microscopy (FLIM) method and examine the dynamic endogenous biomarker (metabolites as described below) changes during pre-implantation embryo development. Based on the quantifiable physiological property changes, we correlate the biomarker changes to the embryo viability (Fig. 5. 1). This non-invasive phasor-FLIM analysis is sensitive, quick and intuitive.

FLIM produces an image, based on the exponential decay rates at each pixel from a fluorescent sample. The fluorescence lifetime of the fluorophore signal is measured to create the image via FLIM[80] (Fig. 5. 2A). When FLIM is coupled with two-photon excitation microscopy, molecules are excited at longer wavelengths (with lower energy photons). This prevents photodamage and allows deeper imaging, resulting in superior image quality[110]. Since endogenous molecules such as collagen, retinoids, flavins, folate, and NADH (nicotinamide adenine dinucleotide) are fluorescent in live cells[81,85], we can collect fluorescence lifetime data to identify these intrinsic fluorescent species. The contributions from these different biochemical species are indicators of an embryo's biochemical property[111,112]. In our approach, we measure the fluorescent lifetime signal from integrated images acquired and transform the raw data using the Fourier transformation to the average arrival time of emitted photons in each pixel, represented by polar coordinates "g" and "s" in the transformation function[85] (Fig. 5. 1C, Fig. 5. 2A). This allows us to present the data in a two-dimensional graphical representation of the lifetime distributions, known as the phasor plot, for each pixel in the FLIM image (Fig. 5. 2).

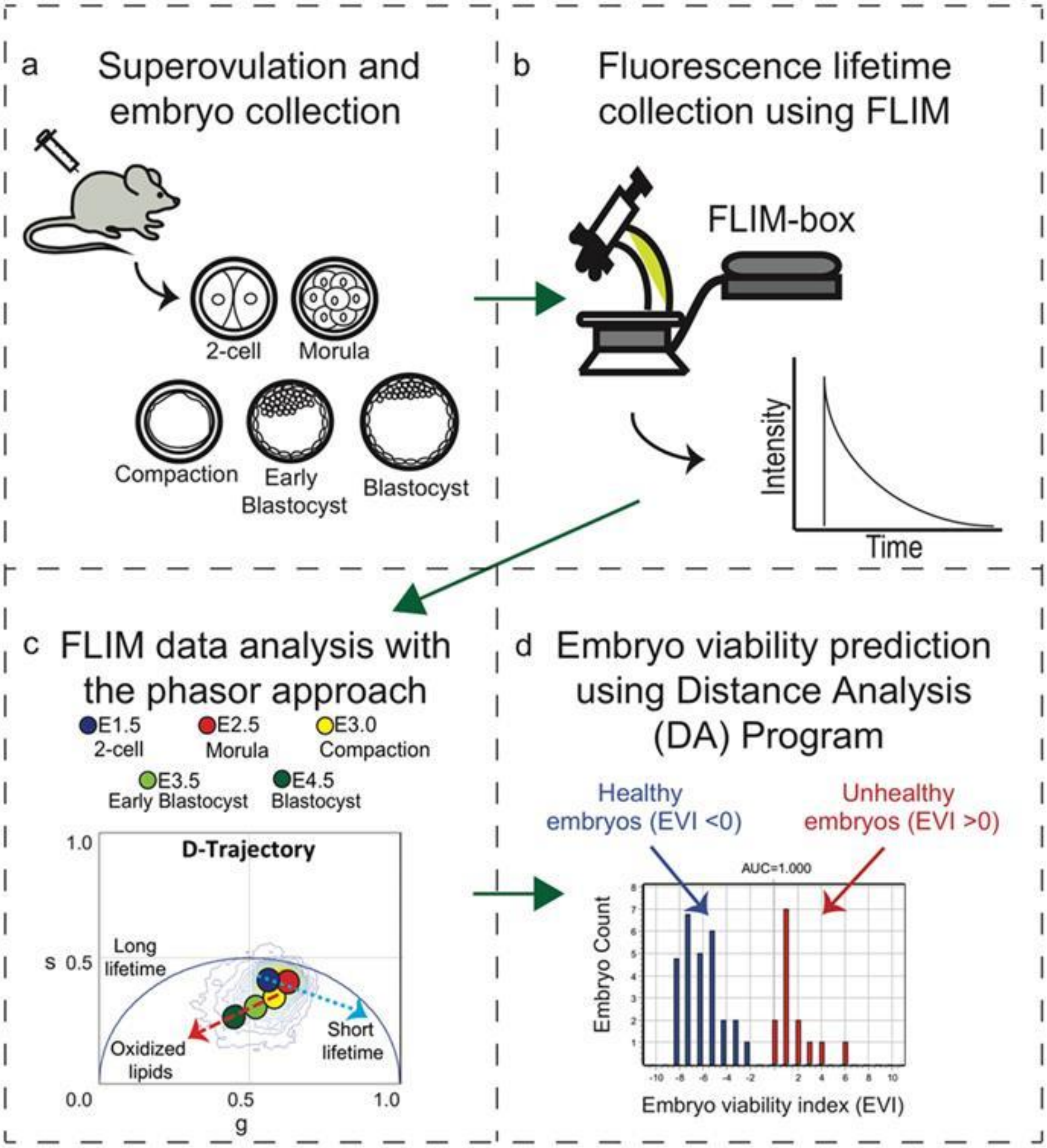

Figure 5. 1 Schematic of the workflow of the experimental design

Figure 5. 1 Schematic of the workflow of the experimental design. A) We collected FLIM images of embryos from superovulated female mice at the following developmental stages: 2-cell, morula, compaction, early blastocyst, and blastocyst. B) Intrinsic fluorescence lifetimes for each embryo are collected using a Zeiss 710 microscope coupled with a FLIM-box. C) The FLIM data analysis of the pre-implantation mouse embryo development was

performed using the phasor approach. D) Distance Analysis (DA) program was applied to predict embryo viability.

Here we have applied the phasor-FLIM approach to pre-implantation mouse embryos and have captured detailed data on their metabolic states at various developmental stages. At each stage, the mouse embryo displays a characteristic phasor-FLIM signature.

For the first time, we defined a unique graphical metabolic trajectory that correlates with energy metabolism and embryo development, which we call the developmental trajectory or "D-trajectory". Initially, embryos uptake pyruvate during glycolysis as their main energy source[113]. As the embryos develop to later stages, the need for ATP increases in order to activate transcription for proliferation. Then, the embryos switch from glycolysis to oxidative phosphorylation, primarily using glucose as their energy source, which also changes the relative redox potential (NAD+: NADH ratio)[114]. The spectroscopic signatures from each of these changes are detected and can be used as criteria to identify healthy embryos at each stage in development. We find that the D-trajectory of pre-implantation embryos cultured in nutrient-deficient media deviates significantly from that of the normal media, indicating that lifetime trajectories can be used to detect metabolic alterations in embryos. We have identified a combination of mathematical parameters that are statistically different between healthy and unhealthy pre-implantation embryos based on machine learning information. Therefore, the phasor-FLIM approach provides an objective, non-invasive, and quantitative method to assess the quality of mammalian embryos.

5.2 Methods

Animals. Animals were treated according to standards set by UC Irvine's University Laboratory Animal Resources (ULAR). CD1 and C57BL/6NCrl females were purchased from Charles River Laboratories. All animal procedures were performed with strict adherence to National Institutes of Health office of laboratory animal welfare (NIH OLAW) and Institutional Animal Care and Use Committee (IACUC) guidelines.

Ethics Statement. Mice used for these experiments were used in accordance with the regulations overseen by the University of California Irvine Institutional Animal Care and Use Committee (IACUC) who assures that the use of live, vertebrate animals in research, testing, teaching or related activities is scientifically justified in accordance to Federal regulations and accreditation standards. All the techniques and procedures in this project have been refined to provide for maximum comfort and minimal stress to the animals. We confirm all experiments were performed in accordance to the guidelines and regulations by the protocol animal welfare assurance number approved by University of California Irvine Institutional Animal Care and Use Committee: A3416-01.UCI has been accredited by the Association for the Assessment and Accreditation of Laboratory Animal Care, International (AAALAC) since 1971.

Pre-implantation mouse embryo collection. Females at 21-24 days old were superovulated with pregnant mare serum gonadotropin (PMSG, Sigma) and 48 hours later with human chorionic gonadotropin (HCG, Sigma). Matings were set each evening after hCG injections. The following morning a vaginal plug was considered 0.5 days post fertilization and embryos were collected at desired stages by flushing oviducts or uterine horns. For our time course collection (intrinsic fluorescence FLIM and THG measurements) superovulation and matings were staggered and all the embryos were collected the same day except late blastocysts (E4.5) were generated by dissecting at E3.5 (one day before imaging) and cultured till next day.

Fluorescence lifetime imaging microscopy (FLIM). Fluorescence lifetime images of the pre-implantation embryos were acquired on Zeiss LSM710 (Carl Zeiss, Jena, Germany), a multi-photon microscope coupled with a Ti: Sapphire laser (Spectra-Physics Mai Tai, Mountain View, CA) with 80 MHz repetition rate. The FLIM data detection was performed by the photomultiplier tube (H7422p-40, Hamamatsu, Japan) and a320 FastFLIM FLIMbox (ISS, Champaign, IL). The pre-implantation mouse embryos were excited at 740nm; an average power of ~3.5 mW was used as previously in live cells and tissue[115]. A Zeiss EC Plan-Neofluar 20x/0.5 NA objective (Cart Zeiss, Jena, Germany) was used. The following settings were used for the FLIM data collection: image size of 256x256 pixels, scan speed of 25.21μs/pixel. A dichroic filter at 690nm was used to separate the fluorescence signal from the laser light. And the emission signal is split with 496nm LP filter and detected in two channels using a band pass filter 460/80 and a 540/50 filter. Every FLIM image was acquired for 50 frames of the same field of view with 256X256 per frame. Only the blue channel (460/80) data was used for this study. FLIM calibration of the system was performed by measuring the known lifetime of a fluorophore coumarin 6 (dissolved in ethanol), which has a known fluorescence lifetime of τ=2.5 ns[116,117]. Embryos were kept in standard culture conditions, 37 °C and at 5% CO_2. FLIM data were acquired and processed by the SimFCS software developed at the Laboratory of Fluorescence Dynamics (LFD).

Converting FLIM data onto phasor coordinates: All FLIM images are transformed onto the phasor plot by the equations below. The g and s coordinates are generated from the fluorescence intensity decay of each pixel in the FLIM image using the following Fourier transformation equations (Fig. 5. 2A):

$$g_i(\omega) = \int_0^\infty I(t)\cos(\omega t)dt \,/ \int_0^\infty I(t)dt$$
$$s_i(\omega) = \int_0^\infty I(t)\sin(\omega t)dt \,/ \int_0^\infty I(t)dt$$

Thus, the phasor approach is a fit-free analysis of FLIM imaging, and the g and s coordinates represent the decay curve at each pixel of the image. Therefore, a phasor analysis transforms complicated spectrum and decay of every single pixel into a unique position on the phasor plot.

Third Harmonic Imaging. The third harmonic generation images and the associated FLIM images of the same field of view were collected using the homebuilt Deep Imaging via Enhanced-Photon Recovery (DIVER) microscope. DIVER microscope is an upright laser scanning microscope, the unique feature is the application of wide photocathode area detector which allows collection of photons from a wide area and angle for high efficiency. The third harmonic generation images and intrinsic fluorescence FLIM images were collected using 40x water immersion objective (Olympus Plan Apo) with 1040nm and 740nm excitation respectively. And UG11 and Blue5543 filters were used for THG and endogenous fluorescence FLIM images collection. An a320 FastFLIM FLIMbox (ISS, Champaign, IL) was used to transfer the data to the phasor plot. Rho110 was used for calibration with known lifetime τ=4 ns[117].

Inhibition of oxidative phosphorylation and glycolysis. Embryos were placed in 25μl microdroplets of KSOMaa (Invitrogen) with the appropriate inhibitors covered in mineral oil (Sigma). Both of the two chemical inhibitors, rotenone and antimycin A cocktail (R&A) and 2-Deoxyglucose (2DeoxyG) were dissolved in KSOMaa. For R&A, we prepare the inhibitor to perform dose dependence measurements for a final concentration of 100nM and 500nM. For 2DeoxyG the inhibitor has a final concentration of 1mM. KSOMaa was used as a solvent and culture media for the control group and treatment group embryos.

H2AXs139 staining. CD1 and C57BL/6NCrl post-imaged embryos are rinsed with Tyrode's acid (Sigma) 3 times and placed in holding and flushing media for 5 minutes to allow embryos to acclimate before 30-minute fixation in 4% paraformaldehyde on ice. Embryos were permeabilized using 0.2% Triton X-100 (Fisher). And then embryos were incubated with H2AXs139 (Genetex) at 1:1000 for 1 hour at room temperature. Embryos were rinsed in 1X PBT three times and then stained with AlexaFluor555 at 1:200. Embryos were rinsed in 1X PBS three times before processing for the Hoechst (Sigma) staining for 10minutes to stain the DNA. Finally, embryos were rinsed and imaged in 1X PBS using 780 Zeiss microscope and Zen 2012 software.

DCF-DA Staining. Embryos are rinsed in Acid Tyrode 3x, washed in KSOMaa 3x, transferred to 5 uM DCF-DA in 1X PBS. Embryos were incubated in DCF-DA solution for 25 min at 5% CO_2 and 37 °C. Embryos were then transferred to Hoechst stain solution for 8 min. Then embryos were placed in KSOMaa and imaged with LSM780 at 5% CO_2 at 37 °C.

Antibody Staining Image analysis for cell number calculation. We used a 3D segmentation pipeline (as previously described)[118] to do a 3D reconstruction of embryos and conduct cell number analysis.

Time-lapse FLIM imaging. Bright-field time-lapse images and FLIM data of *in vitro* cultured embryos were collected every 4 hours for a period of approximately 60 hours starting from the 2-cell stage (E1.5) until the blastocyst stage (E4.5). All FLIM images were collected using the Zeiss LSM710 confocal microscope within stage incubator to obtain the normal *in vitro* culture conditions (37 °C, 5% CO_2).

Distance Analysis Program. The FLIM data collected from individual embryos are placed in either of two categories the H (control group has FLIM signature from the embryos developed to the blastocyst stage) and UH (sample group has FLIM signature from the embryos arrested at compaction stage or even earlier). The distance algorithm can generate a “spectra” from the given (up to 24 parameters) of phasor FLIM distributions corresponding to individual embryos. The 24 parameters are the 2 coordinates for the center of mass g and s, 2 second axial moments a and b after diagonalization, the angle of the distribution from the diagonalization and the total number of pixels in the phasor plot from the 4 slices of the 3D phasor histogram. For each parameter set, we calculate the average of the parameters and the standard deviation. Then we construct a function that we call "distance" in which we calculate the difference of the average of the two sets weighted by the variance of the parameter in each set for the group H and UH respectively. Using distance analysis, a training set can be generated based on the best weight set that has been chosen to separate the H and UH set embryos according to the distance from the average of each set. Finally, after the training set has been generated, the rest of the embryos were tested, and an embryo viability index (EVI) is calculated for each embryo. Using the EVI index for the spectra of the training set, we can build the histogram and determine if a member is a true positive (below 0) or a false positive (above 0). Statistical methods such as the area under the curve (AUC) are then used to determine the quality of the training set. If the AUC is close to one, the two groups are more separable since there are less false positives. The Distance approach has been used previously to determine the separation of spectra in human cancer tissues[119]. More details of the distance analysis calculation can be found in Dr. Ranjit's recent publication (LFD)[119].

Statistical analysis. Data are presented as mean ± standard deviation. For the FLIM data, the statistical analyses were performed using student t-test for the g value only, $p<0.05$ was considered as statistically significant.

The box-whisker plot showing the prediction ability represents the median ± min/max from each indicated group (Training set H and UH group, Tested H and UH group).

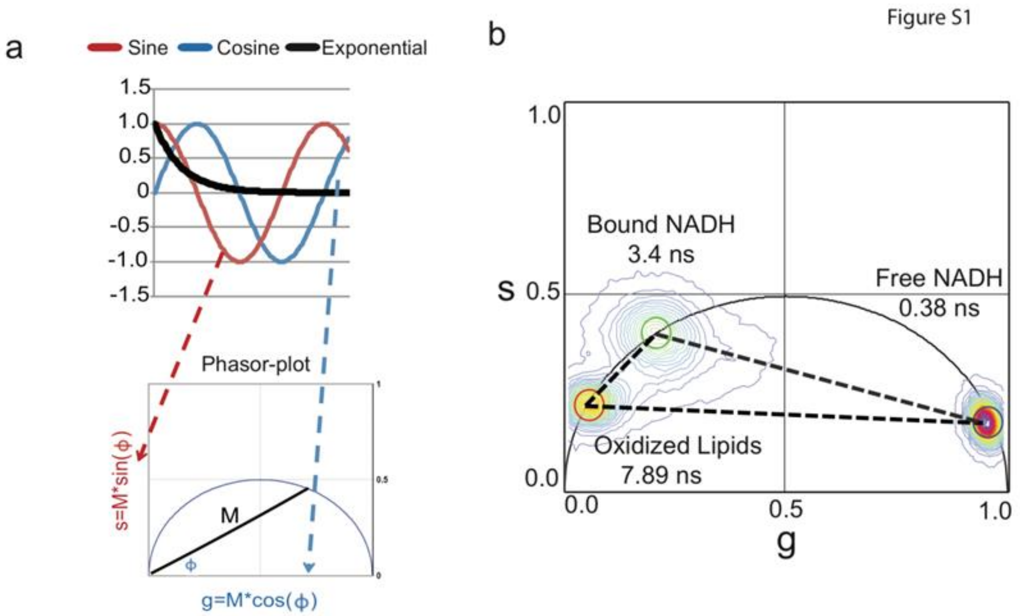

Figure 5. 2 Phasor FLIM analysis

Figure 5. 2 Phasor FLIM analysis. A) Phasor FLIM analysis. During FLIM collection, a pulsed 2-photon laser is used to measure the intensity at short time windows (time arrival of the photons) as a function of time. Instead of fitting the decay curve into an exponential equation (black line), the raw data (intensity at each pixel) is transformed into polar coordinates by plotting the sine (red line) and cosine (blue line) using Fourier transformation, for every pixel in the object, the fluorescence lifetime can be obtained as "phasor lifetime". B) Phasor fingerprint of pure intrinsic biomarkers of free NADH in solution, bound NADH in the presence of lactate dehydrogenase, and a long lifetime species derived from lipid droplets. Given that the free form of NADH exhibits a compact structure with a low fluorescence quantum yield (φ=0.019) and a short lifetime of 0.4ns and the extended form of NADH bound to lactate dehydrogenase with a much higher quantum yield (φ= 0.099) with a longer fluorescence lifetime up to ~3.4ns, the lifetimes of these two states can be easily distinguished[51]. Based on the law of phasor addition, any sample contains the combination signature of these three species will fall within the triangle joining the three phasors.

5.3 Results

5.3.1 The lifetime D-trajectory of pre-implantation embryos

Two different mouse strains (a non-inbred CD1 and an inbred C57BL/6NCrl) were used to acquire a comprehensive representation of the phasor-FLIM distribution patterns of embryos during pre-implantation development (Fig. 5. 3 and Fig. 5. 5A). Fluorescent lifetimes of endogenous fluorescent species, excited at 740nm, were collected at the 2-cell (E1.5), morula (E2.5), compaction (E3.0), early blastocyst (E3.5) and blastocyst stage (E4.5), and pseudo-colored according to the phasor coordinates (Fig. 5. 3A, B). The phasor coordinates, which is the averaged fluorescent lifetime, of the 2-cell and morula stage embryos have a unique lifetime distribution pattern distinct from all other cell and tissue types measured (blue arrow, Fig. 5. 3B)[81]. This unique phasor lifetime position may reflect special characteristics of totipotent cells, which mirror low oxygen consumption and preferential utilization of pyruvate oxidation[120]. On the other hand, compaction to blastocyst stages display average phasor coordinates typically observed in pluripotent cells (red arrow, Fig. 5. 3B)[63,92]. We refer to this characteristic developmental time course lifetime distribution pattern as the developmental trajectory or "D-trajectory". Phasor-FLIM lifetime distributions of individual embryos from both outbred and inbred mouse strains (Fig. 5. 3C, D) follow a similar developmental trend, D-trajectory. In order to examine whether the genetic background of mice influences the D-trajectory, we compared the trajectories of both CD1 and C57BL/6NCrl strains (Fig. 5. 3C, D). While the average lifetimes (g and s values) at specific embryonic stages are somewhat variable, the overall D-trajectory distribution (blue and red arrows) of C57BL/6NCrl is similar to that of CD1 mice. We conclude that the D-trajectory is a characteristic distribution behavior observed among pre-implantation mouse embryos. Lastly, we have applied time-lapse FLIM imaging to individual embryos (n=16), and continuously followed at 3-hour time intervals from 2-cell (E1.5) to blastocyst stage (E4.5) for approximately 60 hours. The *in vitro* developmental trajectory (Fig. 5. 5C) of each embryo mirrors the D-trajectory (Fig. 5. 3B, with blue and red arrows). In sum, the combined two lifetime trajectories (blue and red arrows) encompass the overall D-trajectory for normal pre-implantation embryo development.

Reactive oxygen species (ROS) plays a key role in cellular metabolism and homeostasis[121,122] and ROS production has been linked to an increase in oxidized lipids[123]. The red arrow (the right to left-downward shift, Fig. 5. 3B) in the D-trajectory is presumably due to an increasing fractional contribution of ROS as well as the oxidized lipids which have a fluorescence lifetime distribution of 7.89ns and fall on the same published location (coordinates) of the semi-circle in the phasor plot (Fig. 5. 2B) [85]. This behavior is consistent with the model that an increase in aerobic respiration and metabolism as well as β-oxidation during pre-implantation mouse development [85] requires more efficient energy production from oxidative phosphorylation [124,125]. We have confirmed the presence of active ROS production with fluorogenic marker 2’, 7’-dichlorofluorescin diacetate (DCF-DA, also known as H_2DCFDA) staining (Fig. 5. 5B).

In order to better characterize the lipid droplets distribution during embryonic development, we have employed third-harmonic generation (THG) microscopy imaging (Fig.5. 4) with Deep Imaging Via Emission Recovery (DIVER) microscope (Fig.5. 4). The interfaces heterogeneity can be detected with the third order nonlinearity χ^3. Given that the process is ultra-fast for structures with THG signals, the lifetime is approximately zero. Figure 5. 4A shows the representative THG intensity images acquired in the same field of view as that of the FLIM images of Figure 5. 4B. The phasor plot of the THG images appears at the coordinate of s = 0 and g = 1. The 3D structure of the lipid droplets of embryos from different stages[126]. Furthermore, we quantify the co-localization correlation of the long lifetime specie in the FLIM images (red) with the lipid droplets (green) in THG images (Fig. 5. 4C, D). During embryonic development, the oxidized lipid signature, color-coded in red for the long lifetime species, (same direction as red arrow in Figure 5. 3B) accumulated. The Mander's split co-localization correlation coefficients increase from 0.0099 to 0.3907 (where a coefficient of 1 is perfect correlation and 0 is complete lack of correlation) with embryonic development, suggesting that the phasor-FLIM distribution changes during these stages are due to increased lipid accumulation. We also characterized the lipid droplets distribution during embryonic development using the 3D THG image (Fig. 5. 4A, E). Cleavage stage embryos have a large amount of small, densely packed lipid droplets, whereas post-cleavage stage embryos have large lipid droplets of the low density. And the dramatic changes for both the lipid oxidation and lipid volume decreasing start happening after compaction stages. These findings demonstrate that the dynamic difference in lipid oxidation can be detected by phasor-FLIM.

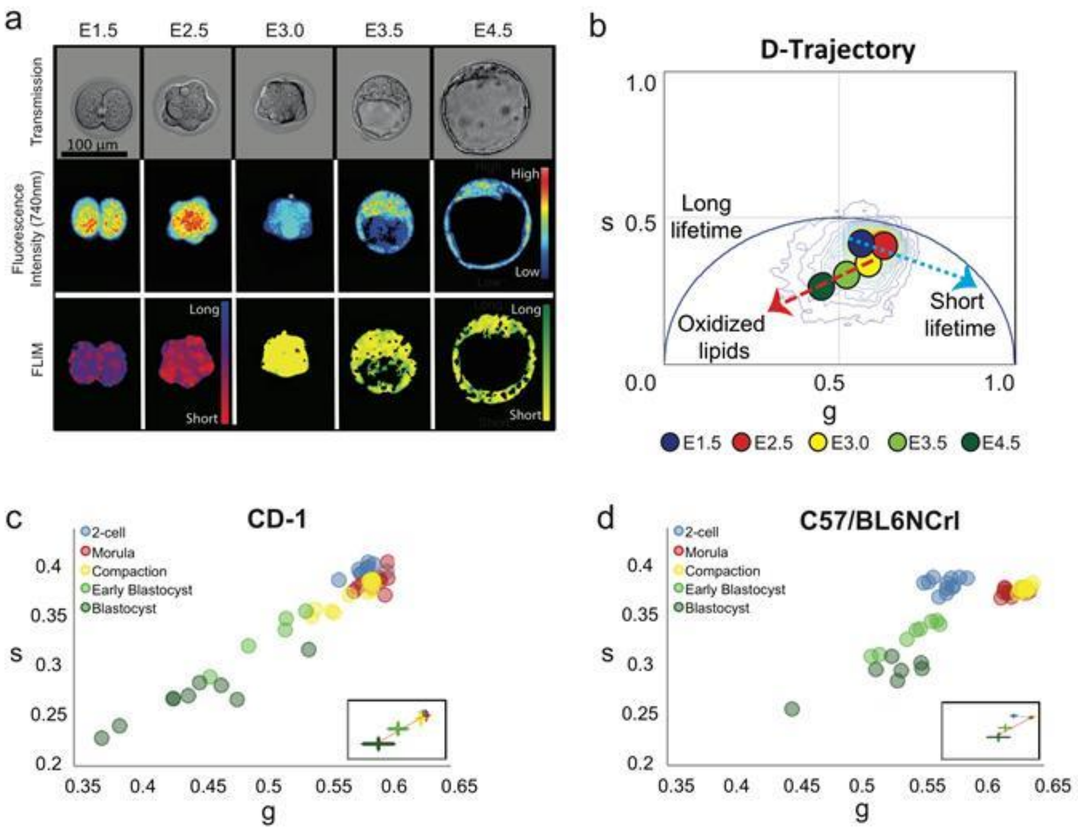

Figure 5. 3 The developmental trajectory of pre-implantation embryos

Figure 5. 3 The lifetime trajectory of pre-implantation embryos correlates with embryonic development. A) Transmission (top row), fluorescence intensity (middle row, 740nm excitation) and FLIM (bottom row) images of representative pre-implantation CD1 mouse embryos at 2-cell, morula, compaction, early blastocyst, and blastocyst stage. In the FLIM images, the pseudo color displays the fluorescence lifetime. B) Phasor-plot of average fluorescence lifetime of CD1 embryos at the indicated developmental stages demonstrating the D-trajectory (D for development). A blue arrow indicates the fluorescence lifetime change from E1.5 to E2.5 and a red arrow shows the change from E3.0 to E4.5. C-D) Scatter plots show the D-trajectory for CD1 and C57BL/6NCrl embryos. The small window shows the average and standard deviation of each stage. CD1: 2-cell (n=29), morula (n=11), compaction (n=33), early blastocyst (n=50) and blastocyst stage (n=35); C57BL/6NCrl: 2-cell (n=25), morula (n=22), compaction (n=21), early blastocyst (n=38) and blastocyst stage (n=42). c) D-trajectory of CD1 embryos (2-cell, n=8; morula, n=8; compaction, n=12; early blastocyst, n=5; blastocyst, n=8. and d) D-trajectory of C57BL/6NCrl embryos (2-cell, n=7; morula, n=3; compaction, n=17, early blastocyst, n=8; blastocyst, n=21). N= number of embryos analyzed.

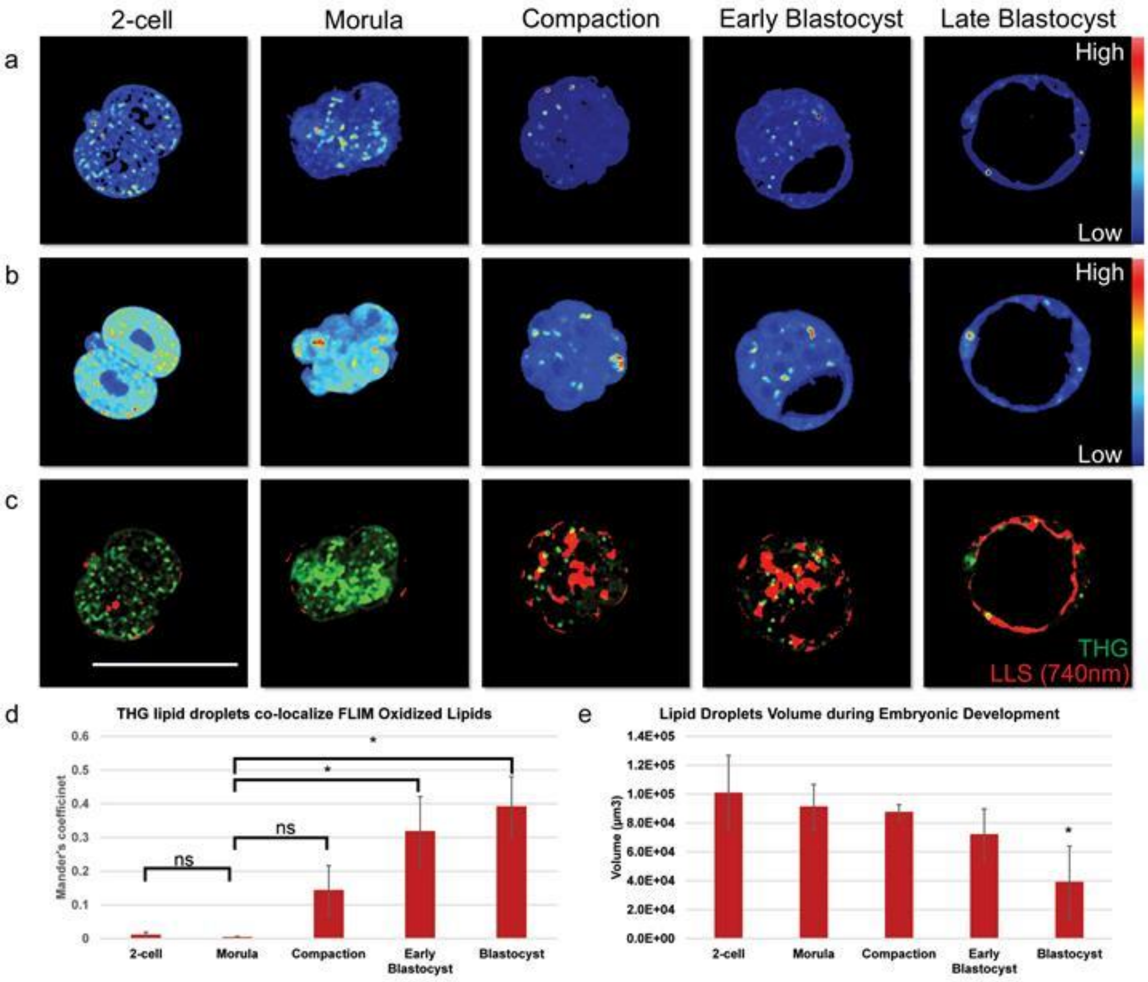

Figure 5. 4 THG and intrinsic fluoresce signal show increasing oxidized lipids

Figure 5. 4 THG and intrinsic fluoresce signal show increasing oxidized lipids during embryonic development. A) Representative third harmonic generation images and B) FLIM images during pre-implantation embryonic development, 2-cell, morula, compaction, early blastocyst and blastocyst stage for the same field of view. From blue to red shows the intensity increase. C) Representative optical sections show co-localization (yellow) of the lipid droplet signal (green) in THG images with long lifetime species (red) in FLIM images. Scale bar sets at 100µm. D) Mander's coefficient of the co-localization results during embryo development which shows the proportion co-localization region of the THG channel and FLIM channel correspondence with long lifetime species-oxidized lipids. 2-cell (n=5), morula (n=3), compaction (n=3), early blastocyst (n=4) and blastocyst stage (n=3). Student t-test results (p-value) for morula to 2-cell, compaction, early blastocyst and blastocyst are 0.1923, 0.0823, 0.0091, and 0.0174 respectively. e) Lipid droplets volume

characterization during pre-implantation embryo development. 2-cell (n=5), morula (n=5), compaction (n=4), early blastocyst (n=4) and blastocyst stage (n=6). Student t-test results (p-value) for morula to 2-cell, compaction, early blastocyst and blastocyst are 0.5066, 0.6367, 0.1416, and 0.0072 respectively.

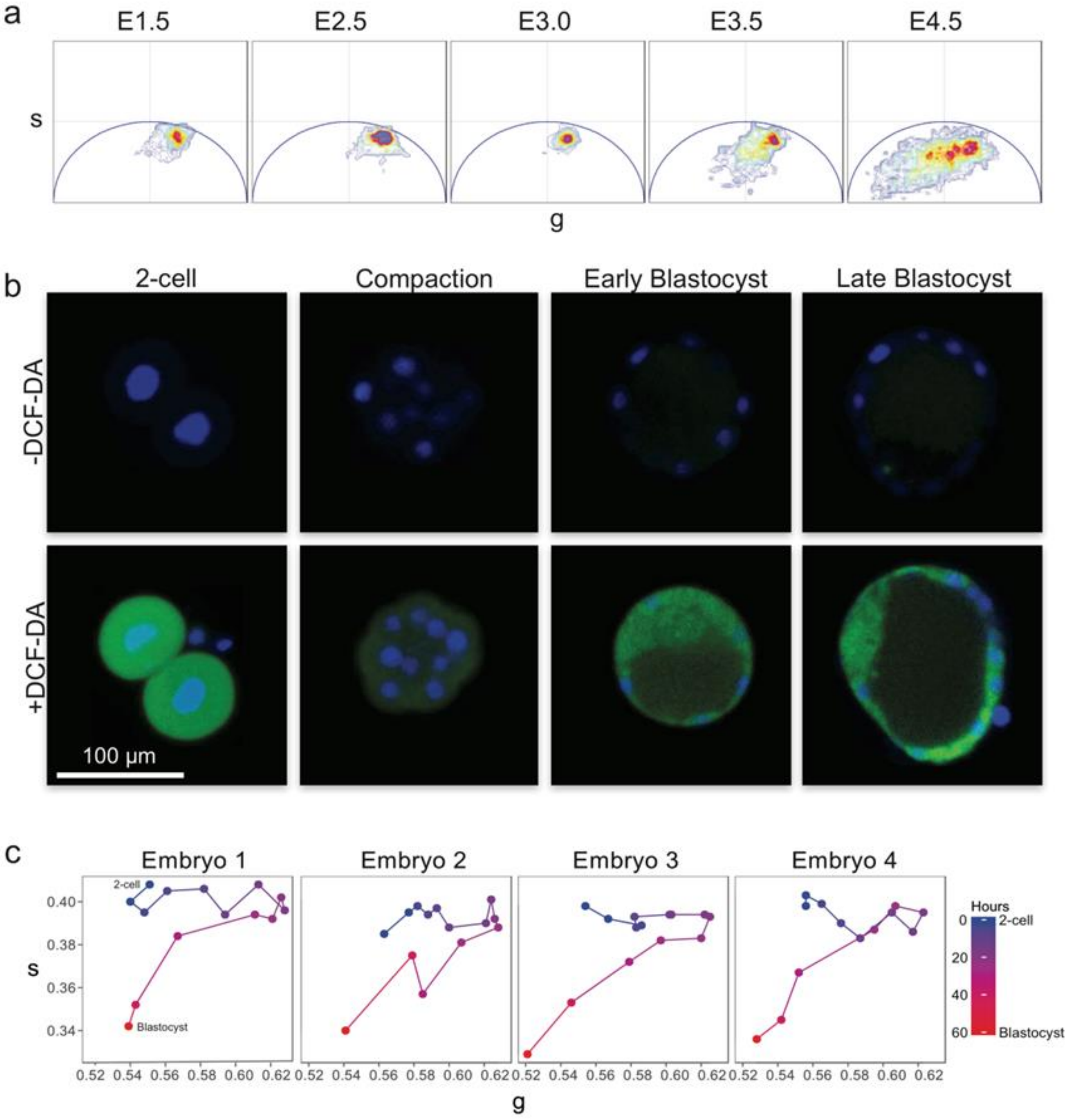

Figure 5. 5 Developmental trajectory correlate with the metabolism of embryo stages

Figure 5. 5 D-trajectory composed of two distinct trajectories that correlate with the metabolism of embryo stages. A) Representative phasor plots for the pre-implantation

mouse embryo from early cleavage stage to blastocyst stage. B) *Detection of reactive oxygen species in pre-implantation mouse embryos.* 2', 7'-ichlorodihydrofluorescein diacetate (DCF-DA) stain across pre-implantation mouse embryos. C) Four examples of the D-Trajectory observed throughout pre-implantation stages (E1.5-E4.0).

5.3.2 Fluorescence lifetime trajectories reveal metabolic states of pre-implantation mouse embryos

The D-trajectory is complex because it is composed of lifetimes from various endogenous fluorescent biochemical species. We first hypothesized that the major component responsible for the shifts in the D-trajectory is intracellular NADH changes based on its fundamental role in energy production during embryogenesis. To test this, we first measured the metabolic activity of intracellular NADH[127]. The bound form of NADH is linked to energy production through oxidative phosphorylation, whereas the free form of NADH is associated with glycolysis[128]. The phasor coordinates of free NADH maps on the right side of the plot with a lifetime of 0.38 ns and the protein bound form of NADH (bound with lactate dehydrogenase) maps on the left at 3.4ns (Fig. 5. 2B). This lifetime distribution of the free and bound forms of NADH in the phasor plot was previously described as the metabolic or M-trajectory[81].

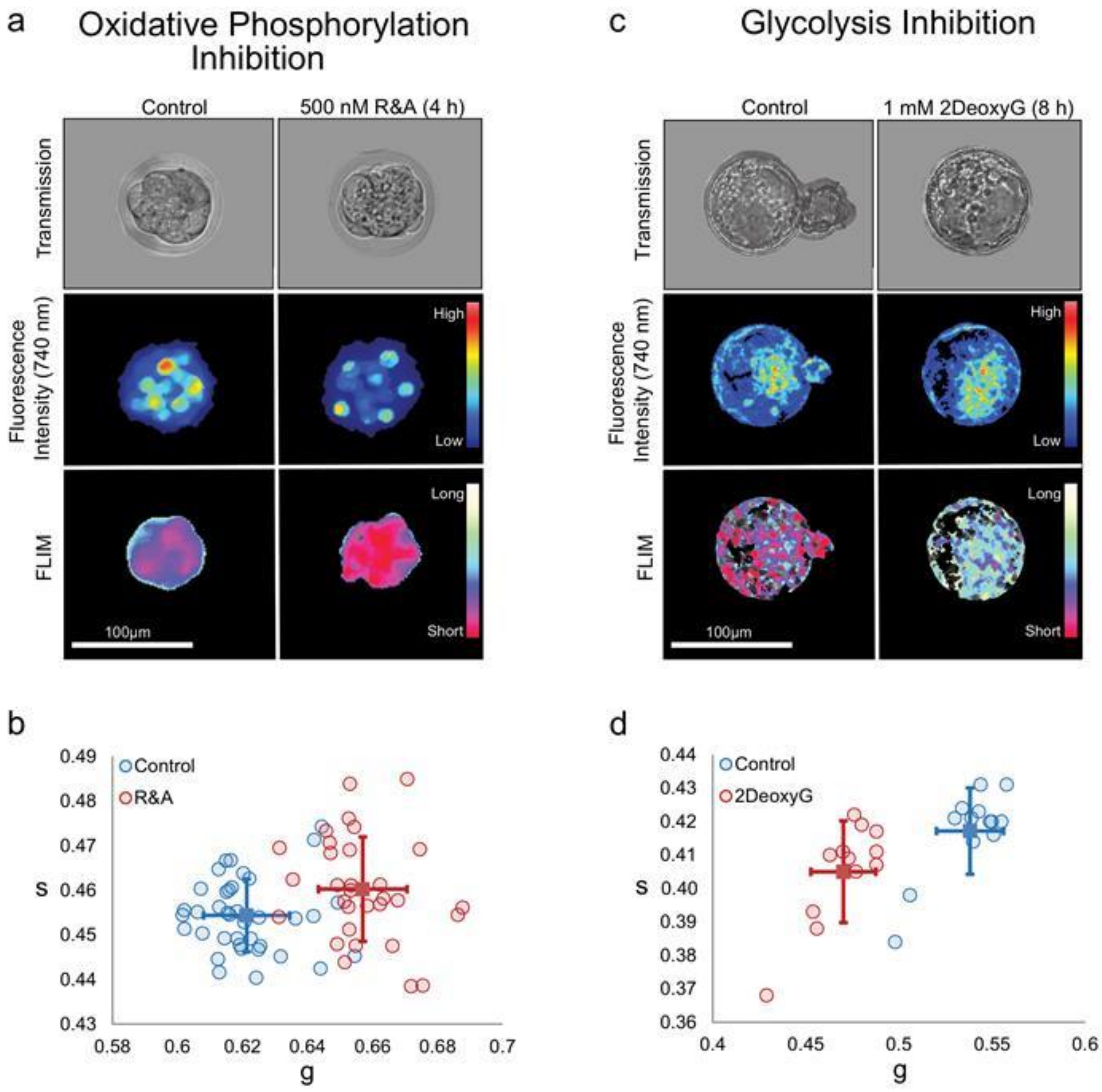

Figure 5. 6 FLIM reveals metabolic states of pre-implantation mouse embryos

Figure 5. 6 Fluorescence lifetime trajectories reveal metabolic states of pre-implantation mouse embryos. A) Transmission (top), fluorescence intensity (middle) and FLIM (bottom) images for control and 4-hour rotenone and antimycin A (R&A) treated embryos. Note a shift from long to short lifetimes (blue to red in FLIM image). B) g and s values of control and R&A-treated embryos for individual embryos. Blue circles are controls (n= 38), red circles are R&A-treated embryos (n= 31), and solid squares and the error bars in the figures means the average and variation of each group (student t-test for g value: p-value= 2.86E-16). FLIM images indicate a rightward shift from long to short lifetimes. C) Transmission (top), fluorescence intensity (middle) and FLIM (bottom) images for control

and 2DeoxyG-treated embryos. Note a shift from long to short lifetimes (red to white in FLIM image). D) g and s values of control and 2DeoxyG-treated embryos. Blue squares are controls (n= 12), red circles are 2DeoxyG -treated embryos (n= 13), and the average of each group can be found in the solid colored squares (student t-test for g value: p-value= 3.88E-09). Fluorescence and FLIM images indicate a leftward shift from long to short lifetimes.

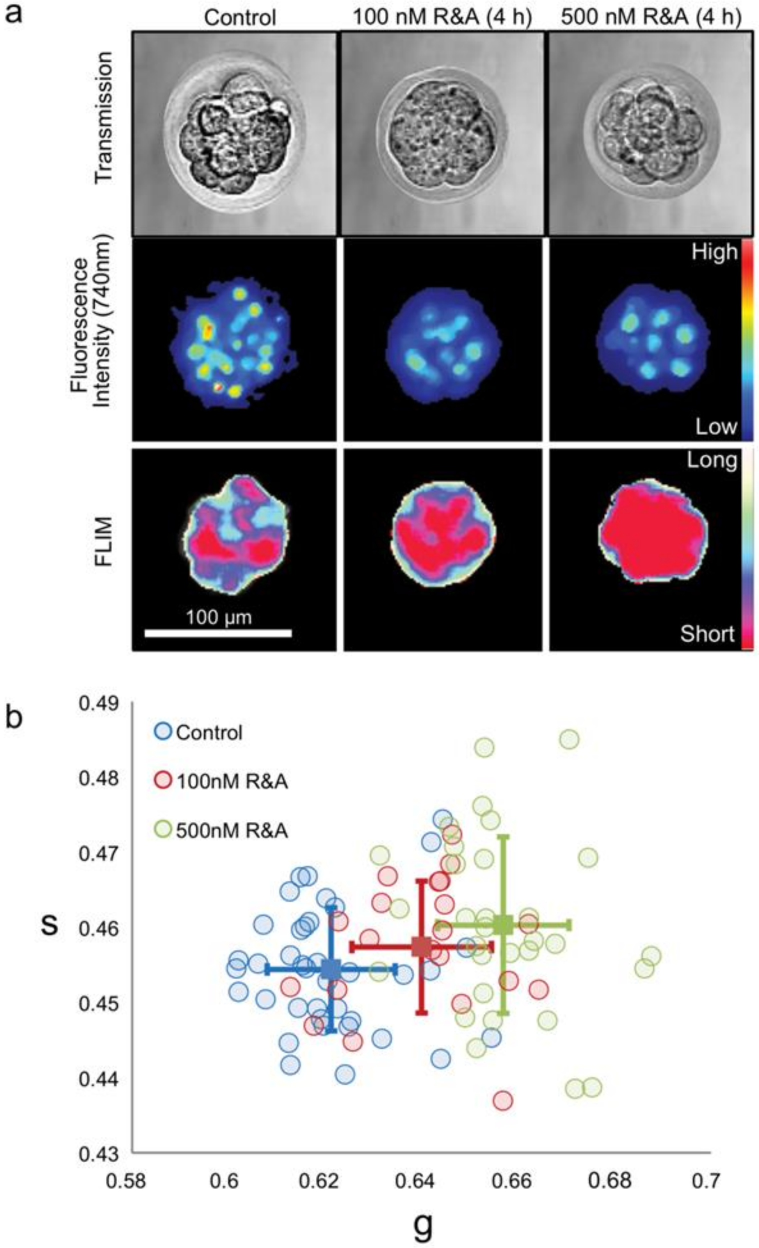

Figure 5. 7 FLIM reveals dose-dependent metabolism change

Figure 5. 7 Fluorescence lifetime trajectories reveal metabolic states changes of pre-implantation mouse embryos and show a dose-dependent manner. A) Transmission (top), fluorescence (middle) and FLIM (bottom) images for control and 4-hour 100nM and 500nM rotenone and antimycin A (R & A) treated embryos, indicating a shift from long to short lifetimes. B) g and s values of control and 4-hour 100nM and 500nM R&A-treated

embryos for individual embryos. Blue circles are controls (n= 38), red circles are 4-hour 100nM R&A-treated embryos (n= 21), and green circles are 4-hour 500nM R&A-treated embryos (n=31). And the average of each group can be found in the solid blue and red circles (for g value of 100nM treatment group and 500nM group compared with control group, p-value=1.76E-5, and 2.86E-16, respectively). FLIM images indicate a rightward shift from long to short lifetimes. Student T-Test, two-tailed tests.

Next, embryos were treated with known biochemical inhibitors of oxidative phosphorylation and glycolysis[128]. Oxidative phosphorylation was inhibited at the early compaction stage with a cocktail of rotenone and antimycin A (R&A) (500nM) by inhibiting complex I and complex III of the electron transport chain. Embryos were imaged after a 4-hour culture period (Fig. 5. 6A). The FLIM images showed increased fractional contributions of free NADH (shorter lifetimes) when compared to controls (Fig. 5. 6A). This shift towards glycolytic metabolism is seen in a dose-dependent manner (Fig. 5. 7), indicating that embryos cultured in R&A have decreased oxidative phosphorylation activity (Fig. 5. 6A, B). We also cultured the early blastocyst stage embryos in 1mM 2-Deoxy-D-Glucose (2DeoxyG), an analog of glucose, to inhibit glycolysis (Fig. 5. 6C). The glucose analog treatment shifted the phasor-FLIM distribution to longer lifetime (an increase of bound NADH) (Fig. 5. 6C), which correlates with a decrease in glycolysis (Fig. 5. 6C, D). These findings suggest that the source of the changes seen in the phasor coordinates throughout the pre-implantation stages in the D-trajectory is in part due to the contribution from metabolic shifts of NADH.

5.3.3 FLIM does not disrupt embryonic development

In order to ensure the safety of the FLIM imaged embryos, we determined the optimum laser power to avoid DNA damages[129], while allowing the rapid and robust acquisition of the FLIM signal on mouse pre-implantation embryos. We exposed 2-cell (E1.5) and morula (E2.5) stage CD1 and C57/BL6NCrl embryos to varying laser powers (1.5, 3.5, 10, and 15mW) and examined the effect on the developmental progression of embryos until the blastocyst stage (Fig. 5. 8A-D). In order to capture FLIM-signals of embryos taken with 1.5mW laser power, 4 times longer exposure time was required than the embryos collected at 3.5mW, 10mW, 15mW laser powers due to their low signal to noise ratio. The majority of embryos exposed to 1.5 mW and 3.5 mW laser power developed to the blastocyst and there were no significant differences between the control (non-imaged) and embryos imaged at the 2-4cell stage or morula-compaction stage, irrespective of strain differences (CD1 or C57BL/6NCrl) (Fig. 5. 8A-D). However, at 10mW, approximately 20% and 35% of CD1 embryos imaged at the 2-cell and compaction stages, respectively, fail to progress to the blastocysts. At 15mW, nearly 50% of CD1 and C57BL/6NCrl embryos imaged at the 2-cell stage were arrested before the compaction stage, while approximately 30% of CD1 and 12% of C57/BL6NCrl embryos imaged at the compaction stage failed to develop to blastocysts. We conclude that CD1 embryos are more sensitive to the laser damage and 3.5mW is the ideal laser power for our FLIM analysis.

Next, we examined the activation of the DNA repair pathway in the embryo by conducting immunofluorescence staining for anti-phosphorylated Histone 2AX (H2AXs139), a novel marker for DNA-double strand breaks [130,131]. Both the non-imaged and imaged embryos were indistinguishable and did not show any signs of DNA repair pathway activation at 3.5mW (Fig. 5. 8E). However, embryos exposed to 1.5mW laser power, which required longer laser exposure time (12 minutes, instead of ~3 minutes) showed the sign of DNA damage (Fig. 5. 8E). We conclude that FLIM imaging of the morula stage embryo at 3.5mW excitation is safe to use and employed in the subsequent experiments.

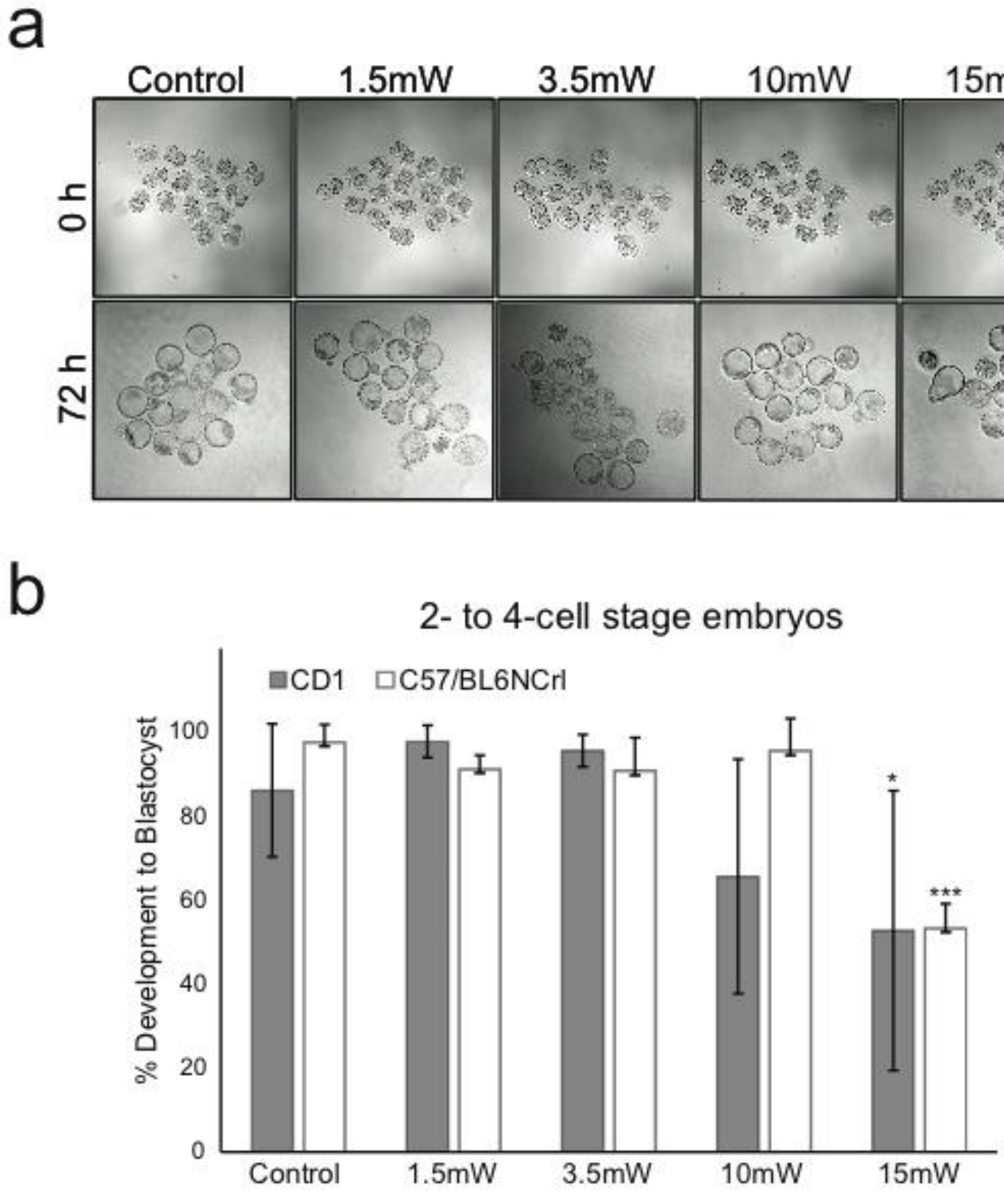
a
Control
1.5mW
3.5mW
10mW
15mW
0 h
72 h
b
2- to 4-cell stage embryos
■CD1 □C57/BL6NCrl
% Development to Blastocyst
0
20
40
60
80
100
*
***
Control
1.5mW
3.5mW
10mW
15mW

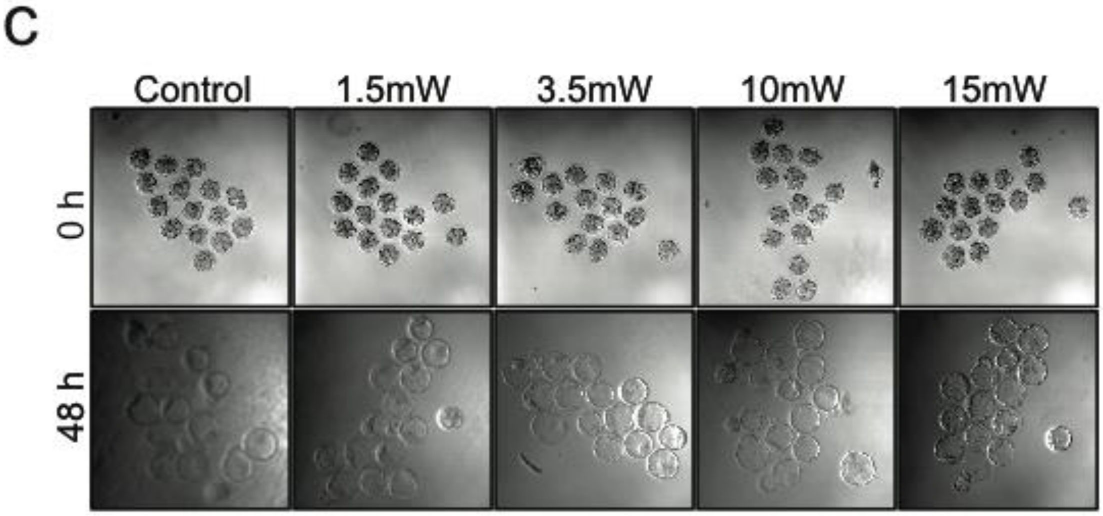
c
Control
1.5mW
3.5mW
10mW
15mW
0 h
48 h

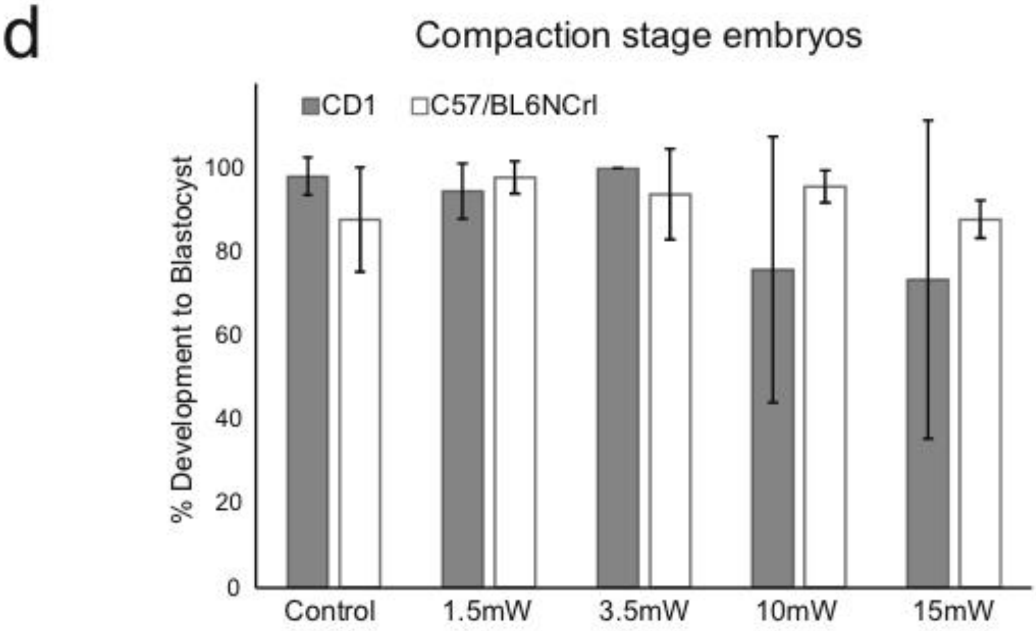
d
Compaction stage embryos
▨CD1
☐C57/BL6NCrl
% Development to Blastocyst
0
20
40
60
80
100
Control
1.5mW
3.5mW
10mW
15mW

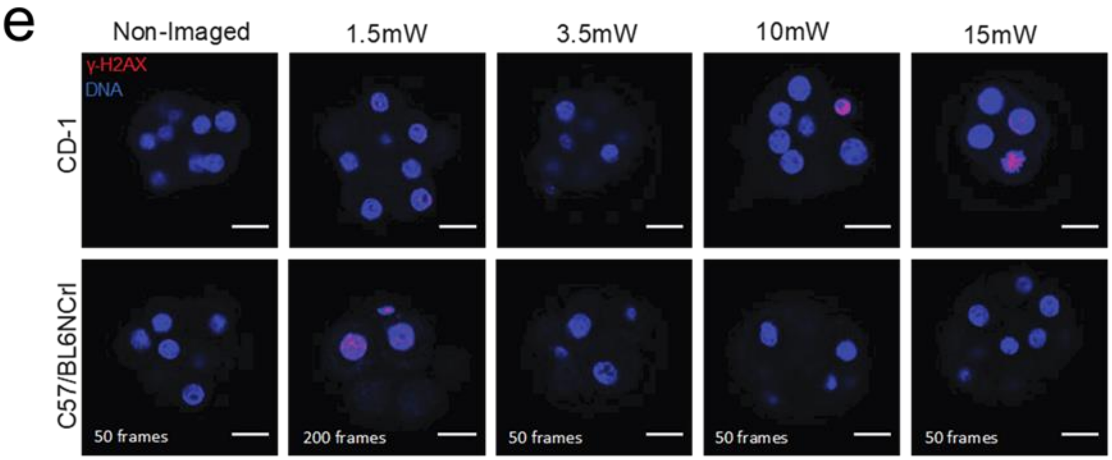

Figure 5. 8 FLIM does not cause development perturbation or DNA damage

Figure 5.8 a, b) Validating the safety of FLIM-imaging of E1.5 pre-implantation mouse embryos. a) Transmission images of embryos before and after imaging and culturing for 72 hours till E4.5. b) Assessment of embryonic development after imaging and 72-hour in vitro culture reported as percent development. For CD1: E1.5 non-image control (n=72); 1.5mW(n=42); 3.5mW(n=42), 10mW(n=31), 15mW(n=45). For C57BL/6NCrl: E1.5 non-image control (n=37); 1.5mW(n=37); 3.5mW(n=36), 10mW(n=38), 15mW(n=37). Image size is 708.49*708.49 µm.
c, d) Validating the safety of FLIM-imaging of E2.5 pre-implantation mouse embryos. c) Transmission images of embryos before and after imaging and culturing for 48 hours till E4.5. d) Assessment of embryonic development after imaging and 48-hour in vitro culture reported as percent development. For CD1: E2.5 non-image control (n=53); 1.5mW(n=43); 3.5mW(n=43), 10mW(n=28), 15mW (n=28, $p<0.05$ *). For C57/BL6NCrl: E2.5 non-image control (n=75); 1.5mW(n=42); 3.5mW(n=47), 10mW(n=44), 15mW (n=41 $p<0.001$ ***). Student T-Test, one tailed test. Everything is nonsignificant except the ones annotated. Image size is 708.49*708.49 µm.
e) Validating the safety of FLIM-imaging of pre-implantation mouse embryos by H2AX staining for Assessment of DNA Damage response initiation of DNA repair pathways. Hoechst (blue) and H2AX (red) stain of E2.5 non-imaged and imaged embryos. For CD1: E2.5 control (n=3); 1.5mW(n=3); 3.5mW(n=3), 10mW(n=3), 15mW(n=3) For C57/BL6NCrl: E2.5 control (n=9); 1.5mW(n=9); 3.5mW(n=8), 10mW(n=6), 15mW(n=8). Scale bar set to 20µm.

5.3.4 FLIM distinguishes pre-implantation embryos under stress conditions

Given that early cleave stage embryos utilize aspartate, pyruvate, and lactate for energy metabolism[132] we tested whether the unique lifetime distribution patterns of an embryo cultured under altered physiological states can be detected by the changes in spectroscopic distributions of phasor-FLIM.

We cultured 2-cell and morula stage embryos in standard mouse embryo culture media (KSOMaa), flushing and holding media (FHM: DMEM-pyruvate free with HEPES), and saline solution (PBS). Brightfield images and FLIM data were collected at 4 hours and 24 hours after treatment (Fig. 5. 9). The FLIM data were collected only once at the first time-point (4 hours)., The 2-cell stage embryos cultured under KSOMaa, FHM and PBS are morphologically normal (Fig. 5. 9A, top). However, the embryos in high-stress conditions (FHM and PBS) show distinct lifetime distribution patterns on the phasor-plot when compared to that of KSOMaa cultured embryos (Fig. 5. 9 B, C, Fig 5. 10A). Subsequently, we find that the embryos under high-stress conditions fail to cleave normally and remain at the 2-cell stage, unlike KSOMaa controls (Fig. 5. 9B, Fig. 5. 10A). We performed the similar analysis using morula stage embryos and found that within a few hours under highstress culture conditions, the phasor-FLIM lifetime trajectories of embryos deviate from those cultured in KSOMaa even before the embryos show any signs of abnormal morphology (Fig. 5. 9D-F, Fig 5. 10B). The cell division in FHM and PBS cultured embryos also slowed down significantly (Fig. 5. 10B). We conclude that phasor-

FLIM is a sensitive method to detect the changes in embryo metabolism upon cellular stress.

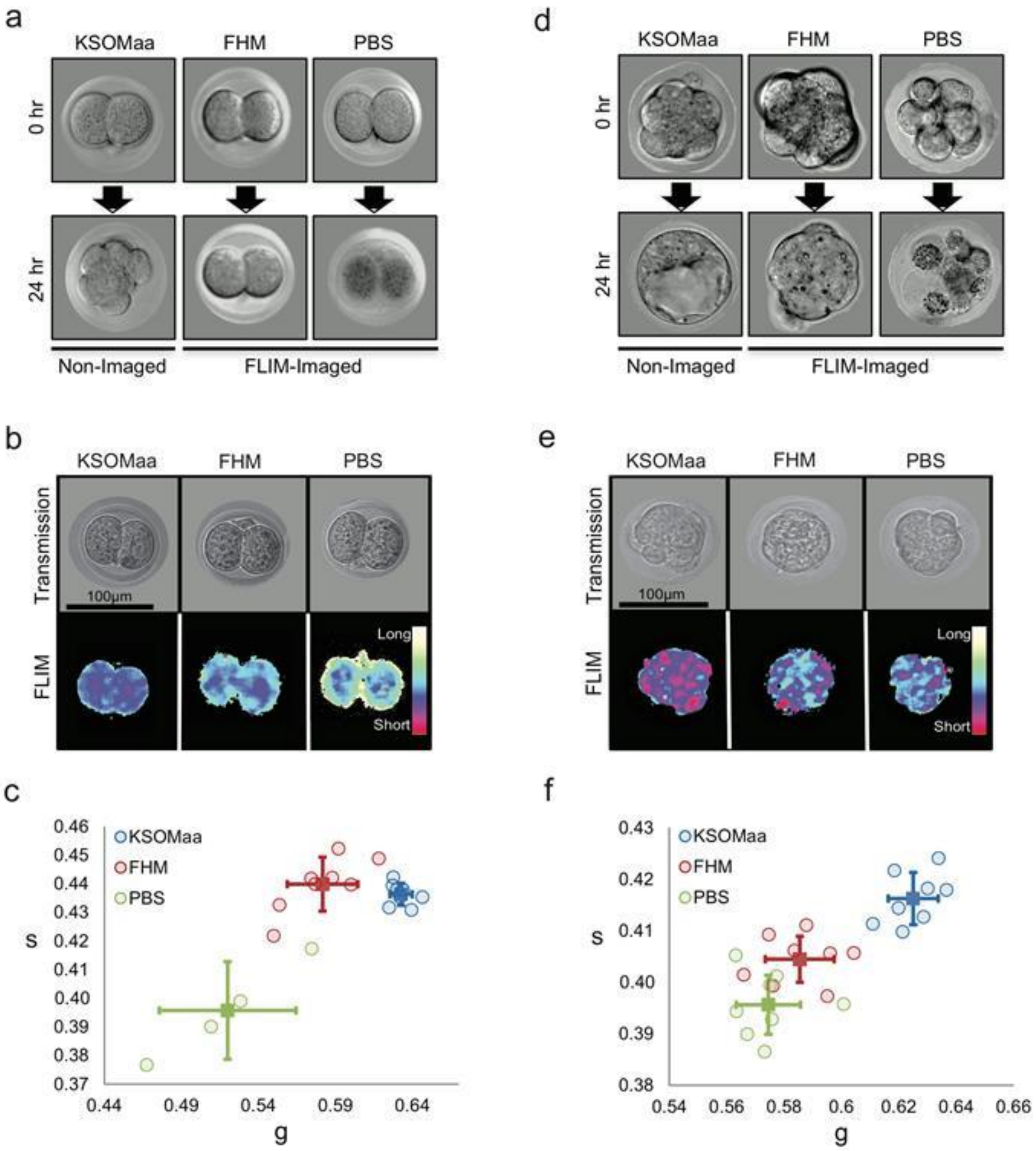

Figure 5. 9 Deviation of FLIM signature under high-stress condition

Figure 5. 9 Deviation of intrinsic lifetime trajectory of embryos cultured in nutrient-depleted media. A) Transmission images of embryos collected at the 2-cell stage and

cultured in KSOMaa, FHM, or PBS for 24 hours. B) Representative transmission and FLIM images of embryos in KSOMaa, FHM, or PBS for 4 hours. C) Scatter plot of g and s lifetimes collected from a group of embryos cultured in KSOMaa (n=10), FHM (n=10) and PBS (n=4) for 4 hours. p-value= 0.0002** and 0.01* (student t-test of g value) for the FHM and PBS group compare with KSOMaa group. D) Transmission images of embryos collected at the compaction stage and cultured in KSOMaa, FHM, or PBS for 24 hours. E) Representative transmission and FLIM images of embryos in KSOMaa, FHM, or PBS for 4 hours. F) Scatter plot of g and s of lifetimes collected from a group of embryos cultured in KSOMaa (n= 8), FHM (n=8), and PBS (n=8). p-value = 9.29E-06** and 3.21E-07** (student t-test of g value) for the FHM and PBS group compare with KSOMaa group.

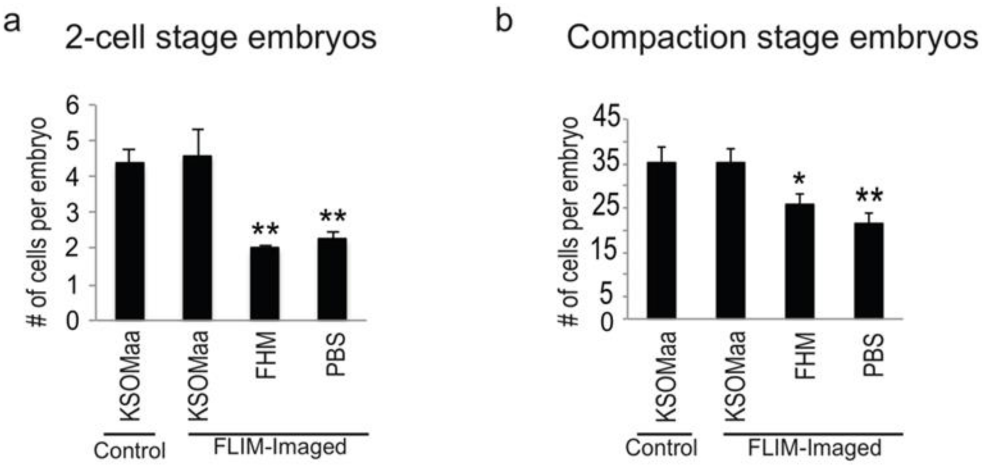

Figure 5. 10 Average number of cells per embryos cultured under high-stress conditions

Figure 5. 10 Average number of cells per embryos cultured under high-stress conditions. A) Bar graph with the average number of cells per embryo after the culturing period for embryos starting at the 2-cell stage (KSOMaa non-image control (n=8), KSOMaa (n=10), FHM (n=11), PBS (n=11), p-value = 0.004** and 0.001**). B) Bar graph with the average number of cells per embryo after the culturing period for embryos starting at the morula stage (KSOMaa non-image control (n=10), KSOMaa (n=18), FHM (n=11), PBS (n=11), p-value = 0.002** and 0.02*).

5.3.5 Derivation of the embryo viability index (EVI) for assessing the developmental potential of the pre-implantation embryo

The phasor distribution analysis of pre-implantation mouse embryos allows us to distinguish between normal and highly stressed embryos (Fig. 5. 9). Therefore, we determined whether the developmental potential of pre-implantation embryos is predictable through phasor-FLIM analysis. We first performed time-lapse phasor-FLIM imaging of embryos from the 2-cell stage for ~60 hours to identify the most desirable stage to predict the developmental potential of embryos (Fig. 5. 10A). At the end of the 60-hour culture period, we classified embryos as healthy (H) if they reached the normal full expanded blastocyst with tightly packed ICM with many and cohesive epithelium shaped TE stage or not healthy (NH) if embryos were arrested before reaching the blastocyst stage or displaying some abnormal morphology at the blastocyst (Fig. 5. 10A). We then applied the distance analysis (DA) algorithm[119] to identify key spectroscopic parameters that could differentiate healthy (H) from unhealthy (UH) embryos by machine learning. Using the DA algorithm, the 3D phasor histogram was separated into 4 sections based on the phasor coordinates (g, s) intensity, from which, 6 parameters were extracted from each section, generating a total of 24 parameters (see Methods). The healthy embryos (H group) were used as the control set and the unhealthy embryos (UH group) were used as the sample set. Each of these sets included images from multiple embryos from each stage in development. Next, we calculated the average and variance of the training set, which includes two groups (H and UH), and weighted only 20 parameters (g, s, the secondary moment a, b and angle from 4 sub-layers, intensity excluded) in each set from 3D phasor plot. After optimizing the weights to maximize the difference between unhealthy and healthy group embryos, we applied these weights to index a new score called the EVI or Embryo Viability Index (Methods). This partition metric defines the degree of separation of the test embryos from the average of the training set where -1 to -10 are unhealthy embryos, and +1 to +10 are healthy embryos.

Next, we examined the DA data from 2-cell, 4-cell, and the early compaction stage to determine the best binary classification model using receiver operating characteristic (ROC) curves (Fig. 5. 11B, C, Fig. 5. 12A, B). We have classified the embryos predicted to be healthy in positive values (EVI<0, in blue), and embryos predicted to be unhealthy in negative values (EVI>0, in red). The plot of true positive rates against false positive rates gives an area under the ROC curve (AUC) for 2-cell, 4-cell, and the early compaction stage embryos, which were 0.739, 0.728, and 0.916, respectively. We conclude that the spectroscopic characteristics of the early compaction stage embryos (prediction accuracy with the highest AUC) possess the best parameters for separating embryos that will develop into normal blastocysts (Fig. 5. 11B, C, Fig. 5. 12A, B).

An embryo viability prediction pipeline was developed based on the DA of phasor-FLIM images of the early compaction stage embryos (Fig. 5. 11D). We have FLIM imaged embryos at the early compaction stage and all of these embryos were allowed to develop to the blastocyst equivalent stage. The resulting embryos were classified as H or UH. We then selected a small number of healthy (H) and unhealthy (UH) embryos and obtained an EVI training data set. The remaining unselected embryos were also subjected to the DA program as “unknowns” (test set) to test the predictability of EVI. In experiment 1, we followed the development of 35 morphologically healthy-looking early compaction stage embryos (pooled from 4 mating pairs), until the blastocyst stage (Fig. 5. 11E, F). Of the 34 embryos, 18 developed to normal blastocysts and thus assigned as healthy (H), and 16 embryos that failed to reach the blastocyst were assigned as unhealthy (UH). When we applied EVIs that were determined by the training set, 83.3% of healthy embryos (15 out of 18 embryos) and 75.0% of unhealthy embryos (12 out of 16 embryos) were correctly predicted by EVI (Fig. 5. 11E, F). Subsequently, we performed another 4 biologically independent experiments using a total of 134 embryos and the results are shown in Table 2 and Figure 5. 12C, D. We achieved 85.9% accuracy (n=134) where a total of 88.5% healthy embryos (n=96) and 73.7% unhealthy embryos (n=38) were identified. Based on the results, we conclude that the DA program is able to predict the development potential of pre-implantation embryos at the early compaction stage.

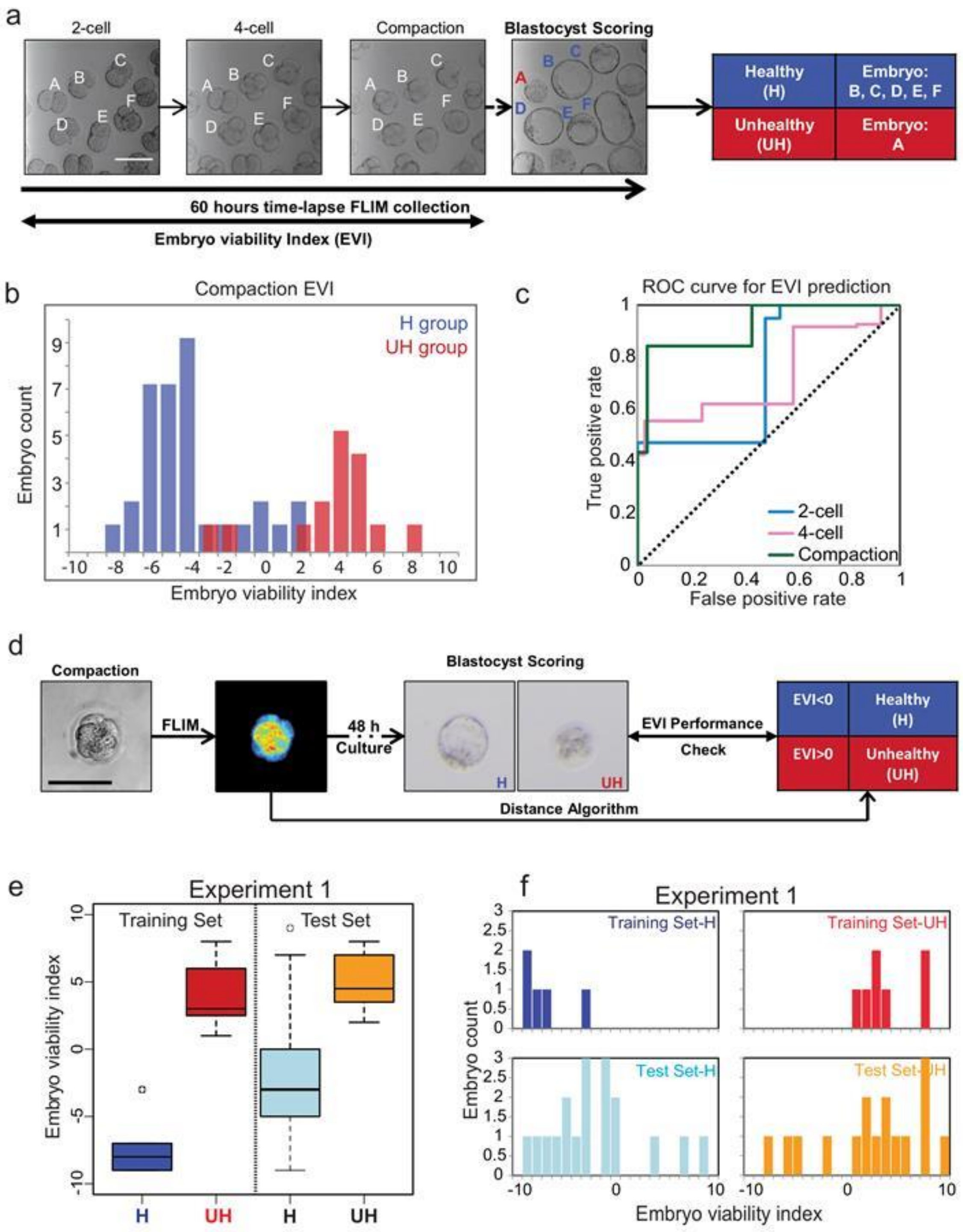

Figure 5. 11 Derivation of the embryo viability index (EVI) gauging embryo quality

Figure 5. 11 Derivation of the embryo viability index (EVI) gauging embryo quality. A) Schematic of our experimental setup. Individual embryos (A-F) were followed from the 2-cell to blastocyst stage and classified as healthy (H) and unhealthy (UH) group according to their morphology at E4.5. B) Histogram of embryo viability index (EVI) of early compaction embryos from one representative experiment (H group, n=37; UH group, n=27). The blue and red bars represent the embryo condition determined as healthy and unhealthy at ~60 hours after FLIM imaging at the pre-compaction stage. C) Receiver operating characteristic (ROC) curve shows the performance of the binary classification model developed from lifetime distribution patterns of early developmental stage embryos (2-cell, 4-cell, and early compaction stage). The area under a curve for each stage is 0.739 (2-cell), 0.728 (4-cell) and 0.916 (early compaction). The dashed line in the diagonal is presented as a random bi-classification model. D) Schematic of FLIM-Distance Analysis Pipeline. E) Box-whisker plots of experiment 1 showing a training set of healthy (n=5) and unhealthy (n=7) groups and tested unknowns of healthy (n=18) and unhealthy (n=16) embryos. (F) Bar graph of embryo viability index of experiment 1. Training set H is in navy, training set UH is in red. Testing set H is in light blue, and Testing set U is in orange.

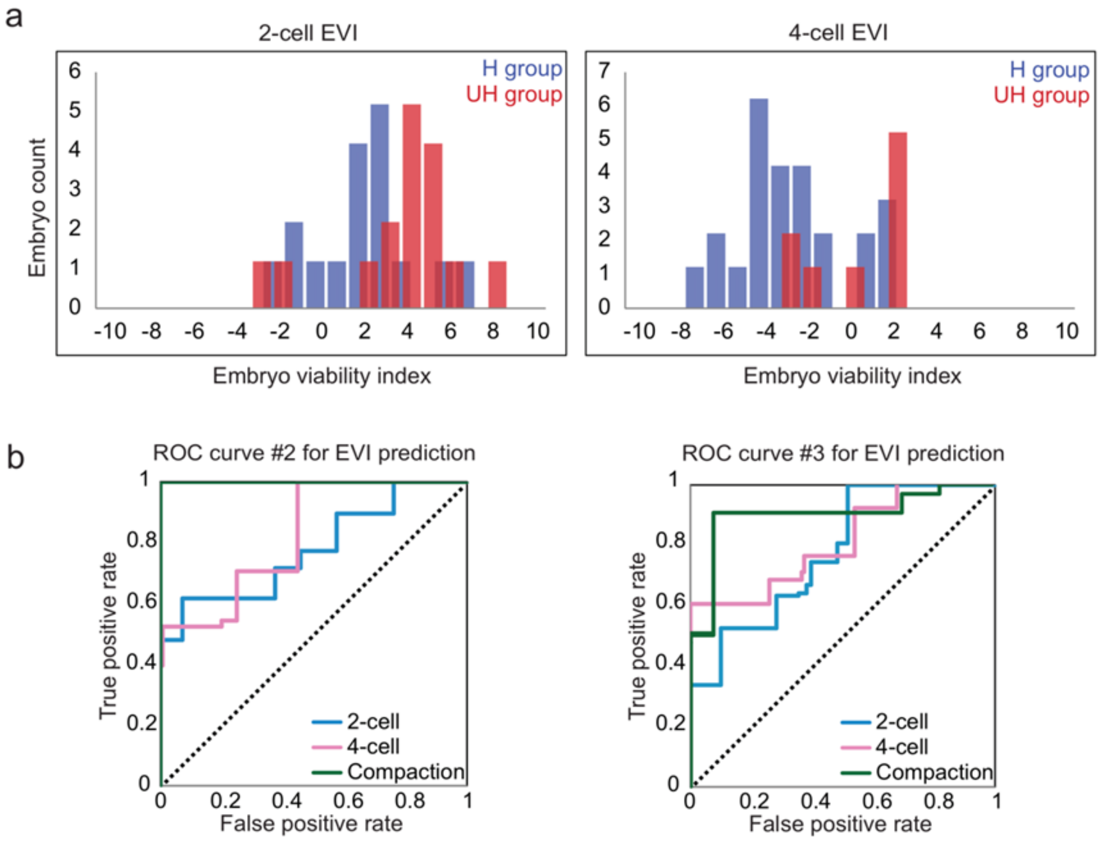

Figure 5.12 1 EVI shows the potential to distinguish healthy and unhealthy embryos

Figure 5. 12 1 Embryo viability index of morula shows the potential to distinguish healthy and unhealthy pre-cleavage stage embryos. A) Histogram of embryo viability index of 2-cell and morula embryos from one representative experiment (2-cell, H group, (n=18), UH group, (n=17). 4-cell, H group, (n=25), UH group, (n=9)). The blue and red bars represent the morula stage FLIM-fingerprints of healthy (H) and unhealthy (UH) embryos after image ~60 hours, respectively. B) Receiver operating characteristic (ROC) curve shows the performance of the binary classification model developed from lifetime distribution patterns of pre-compaction stage embryos (2-, 4-, and early compaction) of two time-lapse FLIM tracking experiment. The area under curve for each stage is 0.777 (2-cell, H, n=37, UH, n=8), 0.823 (4-cell, H, n=45, UH, n=8) and 1.000 (early compaction, H, n=30, UH, n=2) for experiment 2 and 0.777 (2-cell, H, n=38, UH, n=10), 0.813 (4-cell, H, n=39, UH, n=7) and 0.945 (early compaction, H, n=39, UH, n=6) for experiment 3.

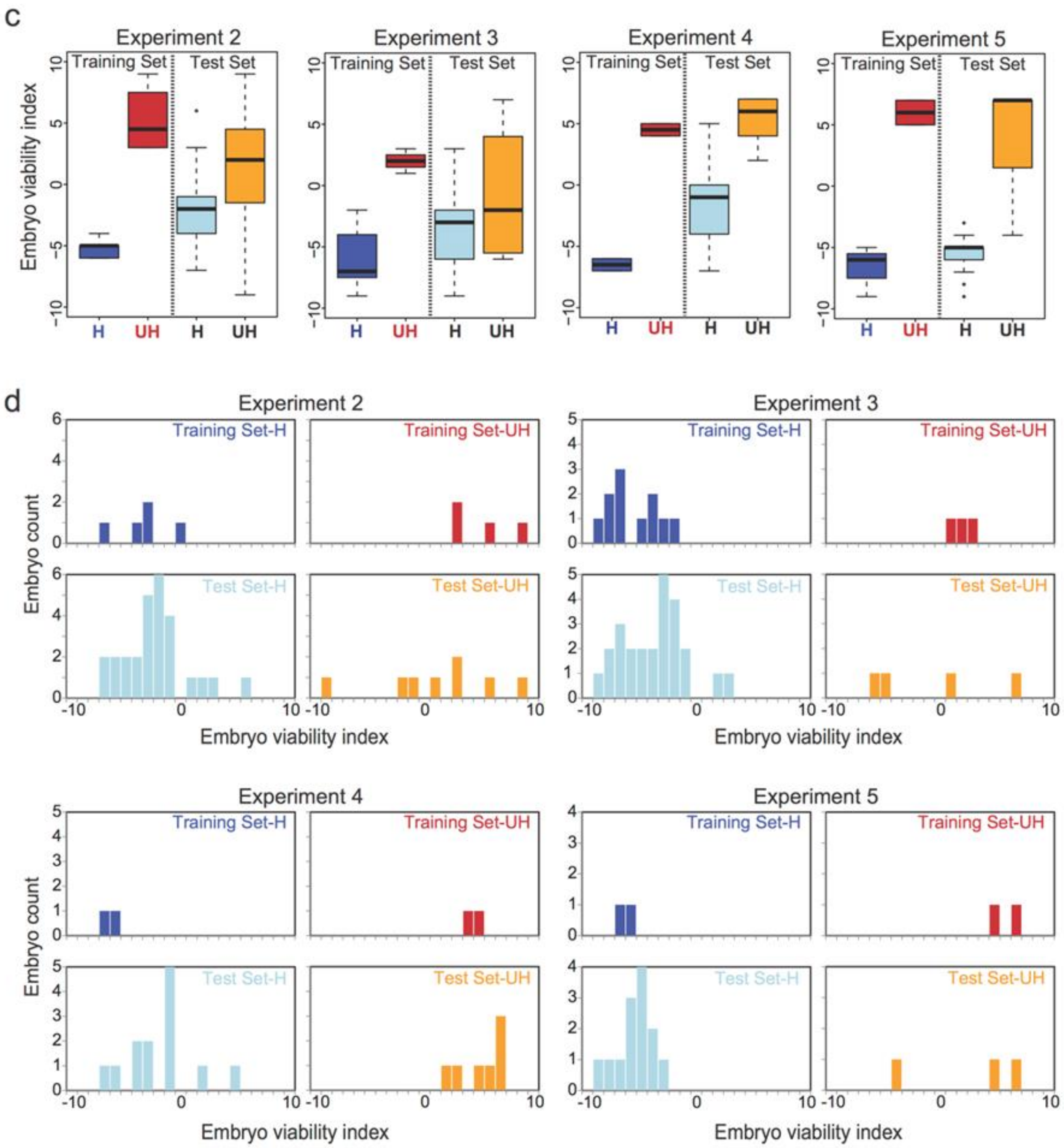

Figure 5.12 2 EVI predicts healthy and unhealthy embryos from 4 experiments

Figure 5.12 2 Embryo viability index predicts healthy and unhealthy embryos from 4 experiments. C) Box-whisker plot showing training set of healthy (H) and unhealthy (UH) groups and tested unknowns of healthy (H) and unhealthy (UH) embryos for experiment 2, 3, 4, and 5. Training set H are in navy, Training set UH is in red, Healthy in light blue, and Unhealthy in orange. The n number for the training set healthy group was n= 5, 11, 2, 3. The n number for the training set unhealthy group was n= 4, 3, 2, 2. The n number for the test unknown healthy group was n= 27, 25, 13, 13. The n number for the test unknown unhealthy group was n= 8, 4, 7, 3. D) Bar graph of embryo viability index of experiment 2, 3, 4 and 5. Training set H are in navy, Training set UH is in red, Healthy in light blue, and Unhealthy in orange.

Table 2 Statistical analysis of DA program as a means to predict embryo viability

	False positive rate	True positive rate	Accuracy	Presicion	Sensitivity	Specificity
Experiment 1	0.250	0.833	0.794	0.789	0.833	0.750
Experiment 2	0.375	0.852	0.800	0.885	0.852	0.625
Experiment 3	0.500	0.920	0.862	0.920	0.920	0.500
Experiment 4	0.000	0.846	0.900	1.000	0.846	1.000
Experiment 5	0.333	1.000	0.938	0.929	1.000	0.667
	0.292	0.890	0.859	0.905	0.890	0.708

5.3.6 Hyperspectral imaging distinguish aneuploidy embryos

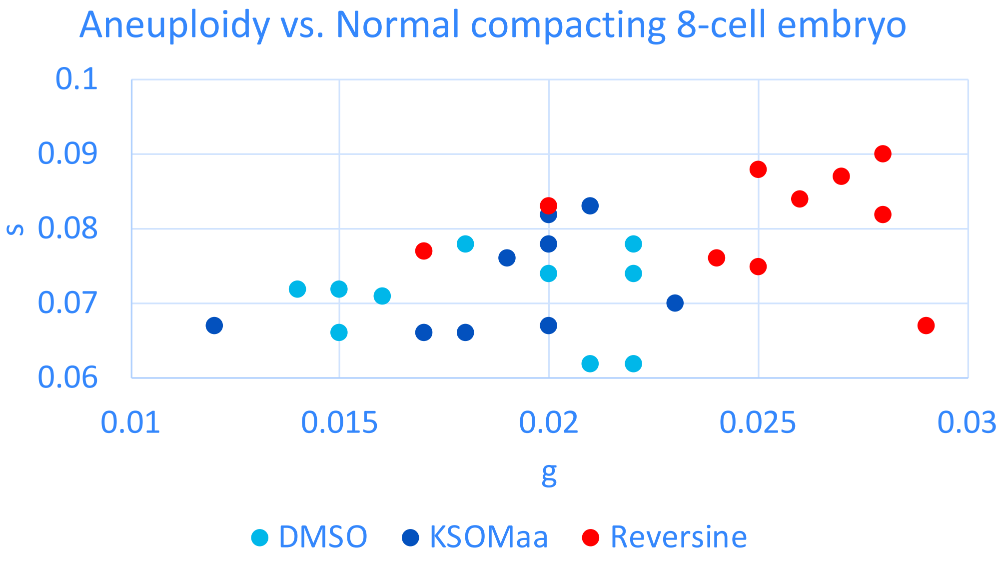

Figure 5. 12 Hyperspectral imaging distinguish aneuploidy embryos

Figure 5.13 Hyperspectral imaging distinguish aneuploidy embryos. Scatter plots shows the hyperspectral imaging results for the compacting 8-cell stage under regular culture condition (KSOMaa, dark blue, n=10), the vehicle control condition (DMSO, light blue, n=10) and Reversine treated group for chromosome abnormal (Reversine, red, n=10). The scatters show the average hyperspectral imaging pattern for each embryo with different treatment. There is a significant difference between reversine and control group on the g coordinate, compare to DMSO group, p-value=0.0008, compare to KSOMaa group, p-value=0.001.

Aneuploidy is common and may be a natural occurrence in early human embryos. Selecting against embryos containing aneuploid cells for embryo transfer has been reported to increase clinical pregnancies per transfer in some studies, but not others. In this section, we are trying to test the capability to use hyperspectral imaging technique to identify the aneuploidy embryos. Reversine is a small molecule can be used for spindle assembly checkpoint inhibitor and induce aneuploidy within the pre-implantation embryos[133]. And KSOMaa is the regular pre-implantation embryo culture media, DMSO group is the vehicle control group. As indicated in the above figure, the preliminary data shows reversine group has a blueshift toward clockwise compared to the regular culture control and vehicle control which indicate the potential to use FLIM to identify the endogenous biomarker change due to genetic background modulation.

5.4 Discussion

Here we report that the phasor-FLIM represents a promising new approach for assessing the quality of pre-implantation mouse embryos. First, we have applied the phasor-FLIM analysis to capture developmental states during pre-implantation development. The spectroscopic trajectory, which we are calling the “D-trajectory” (D for development), is attributed to a combination of metabolic fluorescent species and production of ROS in conjunction with oxidized lipid metabolism within the embryo (Fig. 5. 3C, D), and this trajectory correlates well with other measurements of embryonic development. Second, the intrinsic lifetime trajectory of pre-implantation embryos cultured in nutrient-deficient media deviates from the normal lifetime distribution, indicating that the lifetime trajectory can be used to detect metabolic changes in embryos. Third, we have applied the DA program that uses spectroscopic parameters from 3D phasor histograms of embryos and shown that EVI is a non-morphological, quantitative index that can provide useful information on the quality of pre-implantation embryos.

Other spectroscopic technologies have emerged as a non-invasive means of revealing embryo viability via detection of various metabolic states of common molecules associated with embryo development. Raman, near-infrared, Nuclear Magnetic Resonance (NMR), and Fourier-transform infrared spectroscopy can also detect the metabolic states of pyruvate, lactate, glucose, and oxygen during pre-implantation mammalian development [29-31]. However, at the present time, these technologies suffer from a number of shortcomings. It is challenging for these approaches to analyze the data in the short time window needed for the host transfer of embryos. The data analyses are technically demanding and may not be intuitively obvious for the general clinical use. The technologies require fluid samples collected from the embryo culture media and the data are inherently noisier. Nonetheless, in the future, with improvements, these spectroscopic approaches are likely to provide physicochemical parameters that will be useful in quantitating the influence of ovulation induction, oocyte retrieval, and *in vitro* culture procedures.

Development of qualitative and objective means for assessing embryo quality and viability that are safer and faster will provide significant advances in IVF and animal breeding facilities. If phasor-FLIM is to be applied for diagnostic purposes, it will be crucial to establish that the procedure does not perturb gene expression after the procedure. To date, embryos subjected to phasor-FLIM analysis appeared to be morphologically normal, and we did not detect signs of apoptosis or aberrations in nuclear morphology. However, it is possible that the phasor-FLIM procedure causes other alterations that cannot be easily detected by these morphological criteria. In the future, it will be important to perform additional molecular characterizations (i.e., DNA sequencing) to eliminate the possibility. As a means of ensuring that phasor-FLIM does not affect implantation efficacy of embryos and embryonic development, it will be also useful to determine the birth rates arising from implantation of phasor-FLIM-treated embryos and follow the developmental processes of newborns. Overall, this work has the potential to improve our understanding of energy metabolism in developing mammalian embryos and advance the ART field directly.

Chapter 6

Metabolic Identification of Cells in Microfluidic devices

Chapter overview: Characterization of single cell metabolism is imperative for understanding subcellular functional and biochemical changes associated with healthy tissue development and the progression of numerous diseases. However, single-cell analysis often requires the use of fluorescent tags and cell lysis followed by genomic profiling to identify the cellular heterogeneity. Identifying individual cells in a non-invasive and label-free manner is crucial for the detection of energy metabolism which will discriminate cell types and most importantly critical for maintaining cell viability for further analysis. In this chapter, we have developed a robust assay using the droplet microfluidic technology together with the phasor FLIM to study cell heterogeneity within and among the human leukemia cell lines (K-562, and Jurkat). We have extended these techniques to characterize metabolic differences between proliferating and quiescent cells - a critical step toward label-free single cancer cell dormancy research. The result suggests a droplet-based non-invasive and label-free method to distinguish individual cells based on their metabolic states, which could be used as an upstream phenotypic platform to correlate with genomic statistics.

6.1 Introduction

Single-cell analysis is important to study heterogeneity among individual cells which can lead to an improvement in disease diagnosis and treatment strategies[134,135]. The ability to confine single cells in individual droplets enabled microfluidic devices to evolve as a valuable tool for single cell analysis[52]. In general, single-cell encapsulation in droplets is performed randomly by optimizing the concentration of cells in the sample solution such that no droplets contain more than one cell in them. In such cases, the encapsulation efficiency is as low as 5%, which is dictated by Poisson statistics. However, the deterministic single cell encapsulation involves both active and passive methods[136]. Active techniques include both laser-induced optical trapping[137] and pico-ejection techniques[138]. These techniques can deliver 100% single cell encapsulation efficiency; however, the throughput is very low (<1 Hz). Passive techniques utilize hydrodynamic concepts to perform high-efficiency single cell encapsulation. One of the passive techniques utilizes the Raleigh-Plateau instability jet breakup at the flow focusing junction such that the droplets with a single cell will be larger than the empty ones. The lateral induced drift caused by the unequal oil flow rates and steric interaction at the bifurcation enable droplet sorting at 79.2% efficiency[139]. Another method utilizes inertial microfluidic principles to order the cells along the channel wall in a curved channel or in a long, high aspect ratio microchannel to perform single cell encapsulation at 80% efficiency[140,141]. Recently, our group has reported a microvortex based technique that can perform both high-efficiency single cell encapsulation (~50%) and size-selective cell capture in a single microfluidic device at low cell loading density[142]. In this study, we used Poisson-based single cell encapsulation in droplets. The cell concentration and the flow rates are optimized to achieve maximum encapsulation efficiency with no doublets or triplets.

Encapsulating single cells is merely the first step in single cell analysis. Once cells are captured, identification becomes difficult given that they no longer exhibit a phenotypic profile or significant morphological difference. Current platforms to perform single-cell studies includes flow cytometry[143], and automated microscopy[144]. Examples of single cell analysis in droplets include screening single cells against the library of drug compounds[145], genome-wide expression profiling using Dropseq[146] and inDrop[147] methodologies. Notably, the single-cell analysis in droplets mostly involves cell lysis and genomic analysis including PCR and sequencing to identify the gene expression level. However, genotyping relies on end results, and fluorescent labeling or cell lysis is not desirable for continuous and dynamic single cell monitoring.

To meet the unmet need for single cell detection and identification, we have developed Fluorescence lifetime imaging microscopy (FLIM) which is a non-invasive, label-free assay that measures energy metabolism in encapsulated cells. Metabolism is fundamentally important for identification between healthy and unhealthy cells, tumor heterogeneity, wound healing, diabetes, and neurodegenerative disorders2-5. The quantitative measurement of the metabolites can be applied as a diagnostic and drug screening tool due to the reflection of the changes during disease development and treatment response[7-9]. The accurate determination of metabolites from a single cell is critical.

The pioneering work of Britton Chance has opened the field of spectroscopy and optical imaging to detect metabolic intrinsic fluorescent co-factors in cells and tissues

[148,149]. These spectroscopic techniques provide information of the natural biomarkers involved in different stages of the electron transport chain, such as the reduced form of nicotinamide adenine dinucleotide (NADH), nicotinamide adenine dinucleotide phosphate(NADPH) and flavins (FAD)[150,151]. Skala et al. have used fluorescence intensity of FAD divided by the fluorescence intensity of NADH to characterize the redox ratio in living cells[46]. FLIM has also been used to determine the changes in metabolism from fluorescence lifetime of NADH and FAD[46,152-154]. We also apply the phasor analysis with FLIM, in which the Fourier cosine and sine transforms of the experimental decay are computed and represented by polar coordinates "g" and "s" in the transformation function on a polar coordinate graph termed the 'phasor plot'.[53,80] Phasor approach provides fit-less and graphical data analysis which is more intuitive[80,91,94,128]. We apply 740nm to excite the intrinsic fluorescent species which can give the maximum excitation for NAD(P)H[45]. Given that endogenous molecules such as collagen, retinoids, flavins, folate, and NAD(P)H are intrinsically fluorescent in live cells[81,85], fluorescence lifetime data can have a mixture of all these species making it difficult to identify these components. Using a short pass filter to collect the emission of NAD(P)H and the phasor method, contributions from these different biochemical species are easily identified and separated. Our previous work has showed a leukemia screening platform combines FLIM and microfluidic single-cell trapping which can successfully distinguish the white blood cells and leukemia cells[155]. However, it has been demonstrated cell-environment may contribute to the leukemia cell metabolism, survival rate, proliferation rate, etc.[19,156] The novel microfluidic single encapsulated oil

droplet can be used to isolate and maintain the cell metabolic signature. And this design can also help with the future personal therapeutic drug introduction and FLIM screening [145]. Compared to the single cell fluorescence-activated cell sorting (FACS) which has been largely used in clinic, the presented metabolic screening platform doesn't have to use the fluorescent tag with expensive antibodies which also might cause cell damage and cell behavior alteration.

Here we have applied the phasor-FLIM approach to leukemia cells and serum-free treated fibroblasts encapsulated one-to-one in droplets and have captured detailed data on their metabolic states. The encapsulated leukemia cells display heterogeneous phasor-FLIM signatures due to different proliferation rates. However, the difference between the metabolic lifetimes of the two leukemia cell types used, are still distinguishable. Furthermore, we found that serum-starved fibroblasts, under a quiescent state, deviate significantly from that of the fibroblasts cultured under normal condition, indicating that lifetime trajectories can be used to detect metabolic alterations during different stages of cell cycle. Our results show that under serum-free treatment, there is a higher free NADH and NADPH production due to increased glycolysis through the pentose phosphate pathway which may contribute to detoxify free radicals or to synthesize fatty acids[157-159]. In summary, our non-invasive phasor-FLIM approach provides an intuitive, sensitive, quantitative method to assess metabolic response in encapsulated single cell droplets which can be applied for fast screening of the cancer cells and drug development.

6. 2 Experimental details

Microfluidic Device Preparation. Microfluidic devices were fabricated in polydimethylsiloxane (PDMS, Sylgard 184, Dow Corning) using soft lithography[160]. The PDMS molded imprints and the plain glass slide is plasma treated (Harrick Plasma Inc) for 2 minutes and were brought together to form a permanent seal. The device is left in the oven at 120 o C overnight to regain its natural hydrophobicity.

Fluidic setup, Leukemia cell preparation and Imaging. In the experiments,Novec 7500 mixed with Picosurf surfactant (5 % w/w) (Dolomite) constitute the continuous phase, and the cells suspended in the culture media forms the dispersed phase. Both the K-562 cells and Jurkat cells (American Type Culture Collection (ATCC®)) were cultured in a T-75 cell culture flask using RPMI 1640 as a basal medium to which fetal bovine serum (FBS) was added (10% by volume). The cell culture media is changed every three days until the cells proliferate to the desired confluency. The cells containing medium were then transferred to a 10 mL Eppendorf tube, centrifuged at 1000 rpm for 5 min and the pellet was re-suspended in the freshly prepared aqueous/dispersed phase. The cell concentration in the resulting suspension was determined using an automated cell counter (ThermoFisher Scientific) and appropriately diluted to the desired concentration.

We used constant pressure source via high-speed solenoid valves controlled by a custom-built lab view program to automate the fluid injection into the microfluidic chip. The single cell encapsulation process was monitored using Nikon 100-S inverted microscope and recorded using Phantom camera, V-310 (Vision Research). To analyze the videos frame by frame to yield the encapsulation data, we used ImageJ, a public domain java based image processing software developed at National Institutes of Health[161].

Fluorescence Lifetime Imaging Microscopy. Fluorescence lifetime images of the cells encapsulated in high-efficiency microdevice were acquired on Zeiss LSM880 (Carl Zeiss, Jena, Germany), a multi-photon microscope coupled with a Ti:Sapphire laser (Spectra-Physics Mai Tai, Mountain View, CA) with 80 MHz repetition rate. The FLIM data detection was performed by the photomultiplier tube (H7422p-40, Hamamatsu, Japan) and a320 FastFLIM FLIMbox (ISS, Champaign, IL). The cells encapsulated in droplets were excited at 740nm. A Zeiss EC Plan-Neofluar 20x/0.8 NA objective (Cart Zeiss, Jena, Germany) was used. The following settings were used for the measurement: image size of 256x256 pixels, with a scan speed of 16μs/pixel. A dichroic filter at 690nm was used to separate the fluorescence signal from the laser light. And the emission signal is split with 496nm LP filter and detected in two channels using a bandpass filter 460/80 and a 540/50 filter. Only the blue channel (460/80) data was used for this study. FLIM calibration of the system was performed by measuring the known lifetime of a fluorophore coumarin 6 which has a known fluorescence lifetime of τ=2.5 ns when dissolved in ethanol. FLIM data were acquired and processed by the SimFCS software developed at the Laboratory of Fluorescence Dynamics (LFD).

Human Foreskin Fibroblast cells preparation. Human foreskin fibroblast cells were cultured and maintained in a 37°C incubator humidified at 5% CO2 atmosphere in Dulbecco's modified Eagle's medium/F12(D-MEM) (1:1) (11320-033, Life Technologies, Carlsbad, CA), supplemented with 10% fetal bovine serum and 1% penicillin streptomycin. The cells were freshly trypsinized and plated onto 35 mm glass bottom dishes (Mattek Corporation, Ashland, Massachusetts) for imaging. The phasor-FLIM signature of NADH bound to lactate dehydrogenase and NADH and NADPH (free form) are shown in figure 6. 6.

Serum Starvation treatment. Dulbecco's modified Eagle's medium/F12(D-MEM) (1:1) (11320-033, Life Technologies, Carlsbad, CA), supplemented with 0.1% fetal bovine serum and 1% penicillin streptomycin were prepared for the serum starvation treatment. The Q2 and Q4 cells were serum starved for 24 hours and 72 hours respectively.

Statistical analysis. Data are presented as mean ± standard deviation. For the FLIM data, the statistical analyses were performed using student t-test for the g value and the value of the ratio of bound NAD(P)H to total NAD(P)H, $p<0.05$ was considered as statistically significant.

6.3 Results and Discussion

6.3.1 Single Cell Encapsulation in Droplets

The microfluidic device has an expansion flow focusing geometry as shown in Fig. 6. 1A. This design has been used by our group for droplet-based applications since 2006 [162]. The device consists of two inlets: Cells suspended in the culture media is injected through the left inlet while the oil phase enters the device through the other inlet. Both the inlets have filters (20 μm) to prevent the debris from clogging the flow-focusing junction. The microfluidic channel height is made comparable to the cell diameter such that no two cells roll over each other. Figure 6.1B illustrates the microfluidic device made from Polydimethylsiloxane (PDMS). It has a unique droplet collection chamber design to prevent the droplet motion throughout the data acquisition process for FLIM.

The process of encapsulation of cells one-to-one into the droplets is illustrated in Fig. 6. 2A. The droplet diameter and droplet generation frequency is adjusted according to the cell influx to ensure that maximum encapsulation efficiency is achieved. This is achieved by precisely tuning the aqueous phase to the oil phase pressure ratio (Pa/Po). At a cell concentration of 2 x 106 per ml, we achieved a maximum encapsulation efficiency of 27 %, with a cell doublet rate of 8 % (Fig 6. 2 C). There is a trade-off between the cell doublet rate and single cell encapsulation efficiency. If no droplets contain more than one cell (no doublets), then the single cell encapsulation efficiency decreases to <10 %. The critical parameters that influence the 1-1 efficiency are the droplet diameter, droplet generation frequency, cell concentration, and difference in cell-media density.

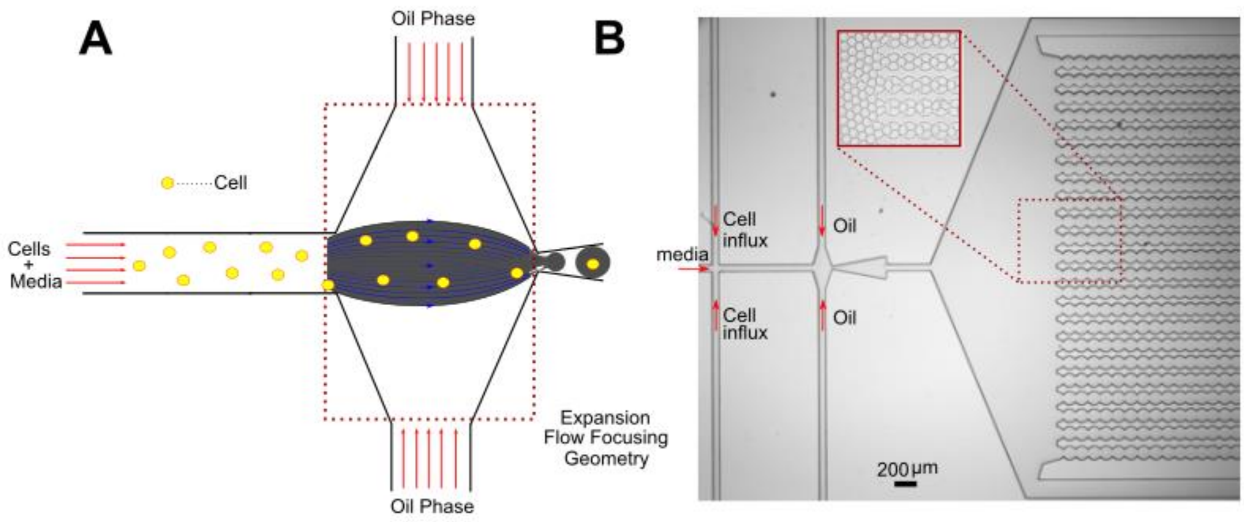

Figure 6. 1 Single cell encapsulation in droplets

Figure 6. 1 A) Device schematic: Cells introduced from the left inlet are encapsulated 1-1 into the droplets which is dictated by the Poisson statistics. B) Microfluidic device made of PDMS, which is used for single cell encapsulation as well as FLIM characterization. Inset shows the droplets if collected in the uniquely designed collection chamber. It prevents the droplet motion during FLIM measurements to a considerable extent.

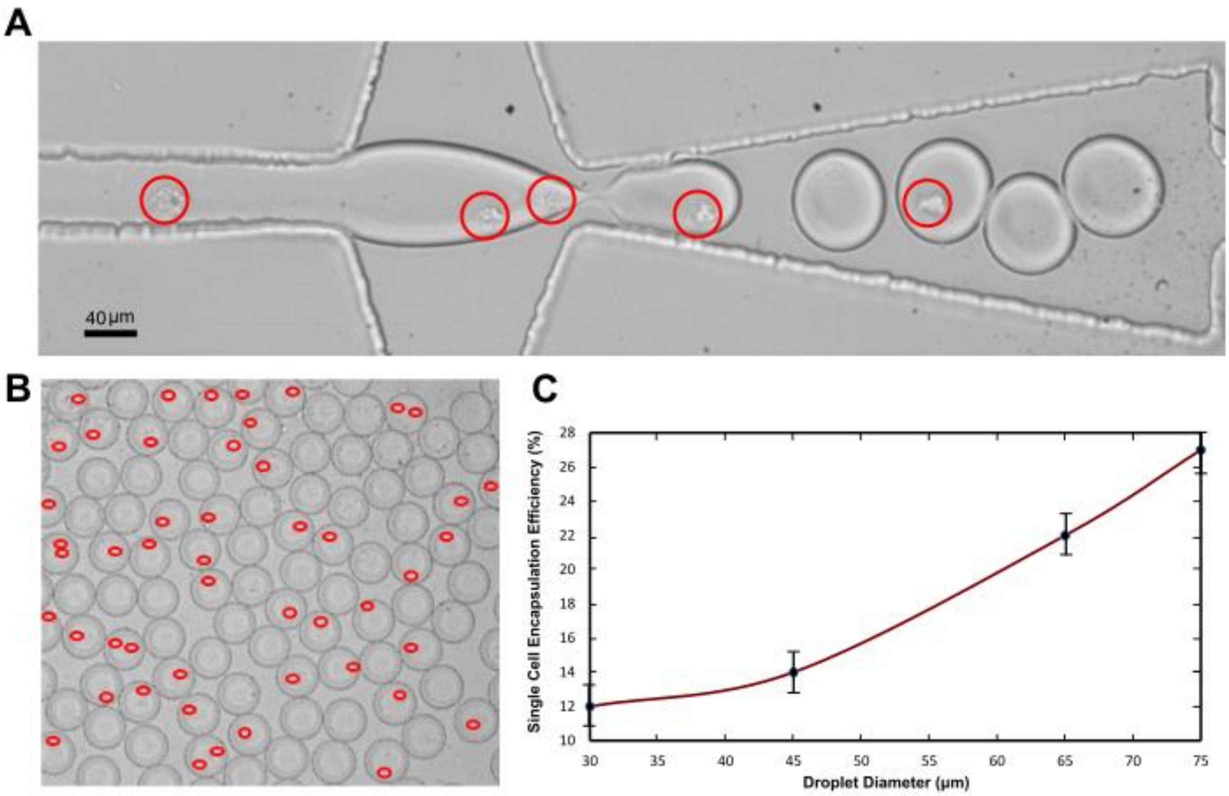

Figure 6. 2 The single cell encapsulation process

Figure 6. 2 A) Demonstration of the single cell encapsulation process. The red circle indicates the presence of one cell. B) Droplets collected after the encapsulation process. The presence of cells is highlighted in red. C) Graphic illustrating the encapsulation efficiency of k-562 cells in droplets. Efficiency increases with the droplet diameter and peaks at an optimum diameter. However, it is observed that the efficiency decreases beyond a threshold diameter due to multiple encapsulations (doublets/triplets) (not shown).

6.3.2 Oil Phase Characterization for best FLIM performance

In order to ensure the FLIM performance, we determined the optimum oil phase to avoid background signal from oil phase, while allowing the rapid and robust acquisition of the FLIM signal on cells encapsulated in the droplets. We screened four different oil phase solution, Novec 7500 mixed with Dolomite picosurf (mix in the ratio of 4:1), ethyl oleate and Ebil EM90, heavy mineral oil with 2% Ebil EM90 and 0.1% Triton X-100 as well as oleic acid with 2% Span 80. To quantify the fluorescence intensity and emission spectra from the oil phase, we expose the 740nm 2-photon laser to the solutions. The emission spectra (Fig. 6. 3) shows that Novec 7500 mixed with Dolomite picosurf (mix in the ratio of 4:1) and heavy mineral oil with 2% Ebil EM90 and 0.1% Triton X-100 present lowest fluorescence intensity which will not interfere with the FLIM imaging collection. Novec 7500 has been used in pharmaceutical and chemical manufacturing processes since its property of cell-friendly and stability which is optimal for live imaging and the down-stream PCR test in the future. Therefore, we choose Novec 7500 as our oil phase for the high-efficiency one-one droplet encapsulation platform.

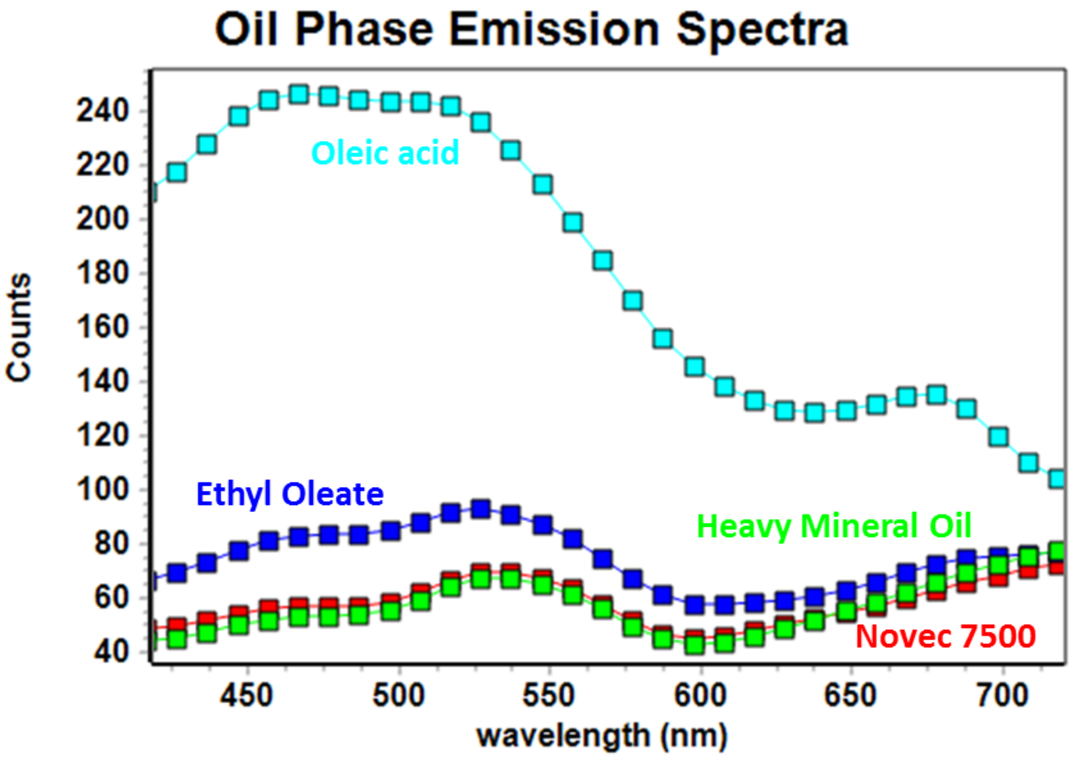

Figure 6. 3 Oil phase characterization

Figure 6. 3 Oil Phase Emission Spectra test (740nm excitation) for Oil 1(red)- Novec 7500 mixed with Dolomite picosurf (mix in the ratio of 4:1), Oil 2(blue)- ethyl oleate and Ebil EM90, Oil 3(green)- heavy mineral oil with 2% Ebil EM90 and 0.1% Triton X-100, Oil 4(cyan)- oleic acid with 2% Span 80.

6.3.3 Differentiation of Leukemia Cell lines in Droplets using FLIM

Two different types of human leukemia cells K562 erythromyeloid and Jurkat T-cell leukemia were encapsulated one-to-one in the droplets (Fig. 6. 4). FLIM images were collected at 740 nm excitation wavelength. The transmission images of the cells in the device, the fluorescence intensity images of the single cells with and without droplet are shown in Figure 4A and 4B. We distinguish the different leukemia cell lines by morphology and phasor-FLIM signature (Fig. 6. 6, Fig. 6. 4C, D).

Most of the normal leukemia cells have a diameter ranging from 8μm to 20μm, and there exist significant size overlap based on our measurement of the leukemia cell lines we investigated, K562 and Jurkat cells (Fig.6. 6). The diameter of the K562 and Jurkat cells are 11.15 μm and 10.48 μm, respectively, which shows no significant difference and cannot be distinguished based on morphology. While leukemia cells cannot be differentiated by size and shape, the FLIM phasor shows significant difference without any label. We applied phasor transformation to the acquired FLIM data and plotted the representative scatter plot of phasor-FLIM signature of the leukemia cells in droplets (Fig. 6. 4C), the Jurkat cells (blue) and K562 cells (red) show a significant difference.

To further quantify the difference of the phasor-FLIM signatures between different cell populations and the cellular heterogeneity within the same population, we apply Distance analysis to plot the 3D phasor information of individual cells of Jurkat (blue), and K562 (red) in the bar graph of Fig. 6. 4D[119]. Both of K562 erythromyeloid cells and Jurkat T-cell leukemia cells demonstrate a relatively shorter lifetime compare to normal cells and tissues[91], and as shown, the index shows the cell phasors of the Jurkat cells are significantly different from the group of K562 cells. These can be explained by the Warburg Effect, in which rapid-proliferating tumor-like cells, i.e., leukemia cells, have stronger glycolysis in glucose metabolism to support fast ATP consumption and biosynthesis of macromolecules and there is tumor heterogeneity due to different metabolic rate.

Phasor-FLIM measurement of regular and quiescent fibroblast cells in droplets

After identification of the difference in the phasor-FLIM fingerprints of different leukemia cell lines (Jurkat and K562), we conducted the rapid label-free single-cell screening to understand the quiescent and proliferation metabolic activity and to further observe the rapid treatment response. The model we used to monitor the metabolic difference between cellular quiescence is human foreskin fibroblast model. Cells from human foreskin fibroblasts cell line were treated for 24 hours(Q2) and 72 hours(Q4) with non-serum media, and the phasor-FLIM signature of each condition was measured (Fig. 6. 5). We collected the NAD(P)H fluorescence emission of encapsulated single cells and fluorescence lifetime images at 740nm excitation and pseudo-colored the higher bound/free-NAD(P)H-ratio group as cyan and the higher free/bound-NAD(P)H-ratio group as pink (Fig. 6. 5A, B). The human foreskin fibroblasts with different treatment type of serum starvation were clearly distinguished from the cells treated using normal condition as highlighted in phasor plot (Fig. 6. 5B) as serum-starved human foreskin fibroblast cells have more components in the color indicating a higher fraction of free NAD(P)H, while normal human foreskin fibroblasts consist of more white color pixels indicating a higher fraction of bound NAD(P)H. The fraction of bound NAD(P)H/total NAD(P)H shows the quantification of significant increase of the free-form of NAD(P)H with serum-free treatment or the induction of cells in a quiescent state. The 72 hours serum-starvation (Q4) group has a significant shift from high NADPH bound fraction to a lower bound fraction (Fig. 6. 5c). This shift, toward a higher free fraction of NADPH and shorter lifetime, in the quiescent group

(Q4) compared to the proliferating group (P) may be caused by the metabolic shift towards the Warburg effect (increased glycolysis in the presence of oxygen) and the pentose phosphate pathway (PPP) pathway[157,163]. Under this glycolytic state, introduced by serum-starvation, there would be a higher lactate production that can create an acidic microenvironment for gene expressions regulation [164-166]. This is important in tumor progression and wound healing promotion. In addition, the PPP pathway can produce more ribose-5-phosphate and NADPH which is needed for the biosynthesis of nucleotides and macromolecules including fatty acids. Given that previous reports have correlated a link between human newborn fibroblasts and cancer cells in regards to similar migratory properties, the screening between cellular state might open a new window of further understanding of the basic mechanisms involved in communication between tumor cells and fibroblasts as well as cancer dormancy for targeted cancer therapy[167].

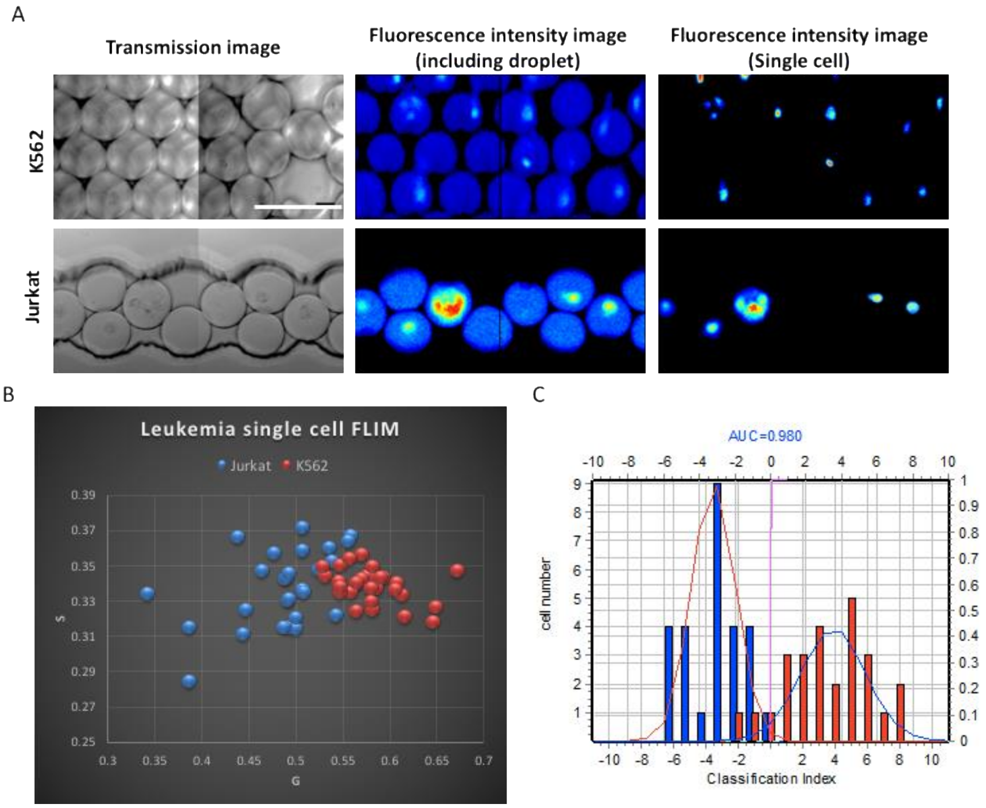

Figure 6. 4 FLIM reveals heterogeneity of leukemia cells

Figure 6. 4 A) Transmission images, fluorescence intensity images of the K562 and Jurkat cells respectively within droplets and without droplets. Scale bar: 100 μm. B) Scatter plot shows the zoomed in phasor-FLIM results of the single leukemia cells in the high efficiency encapsulated droplets for both K562 (red) and Jurkat (blue) cells. The different leukemia cell lines K562 and Jurkat have significant difference, with a p-value for g, 0.025 and s, 0.0002. C) Bar graph of classification index of leukemia cell lines. K562 cells are shown in red, Jurkat cells are in blue. The area under curve (AUC) is 0.980. (K562 group, n=33, Jurkat group, n=32).

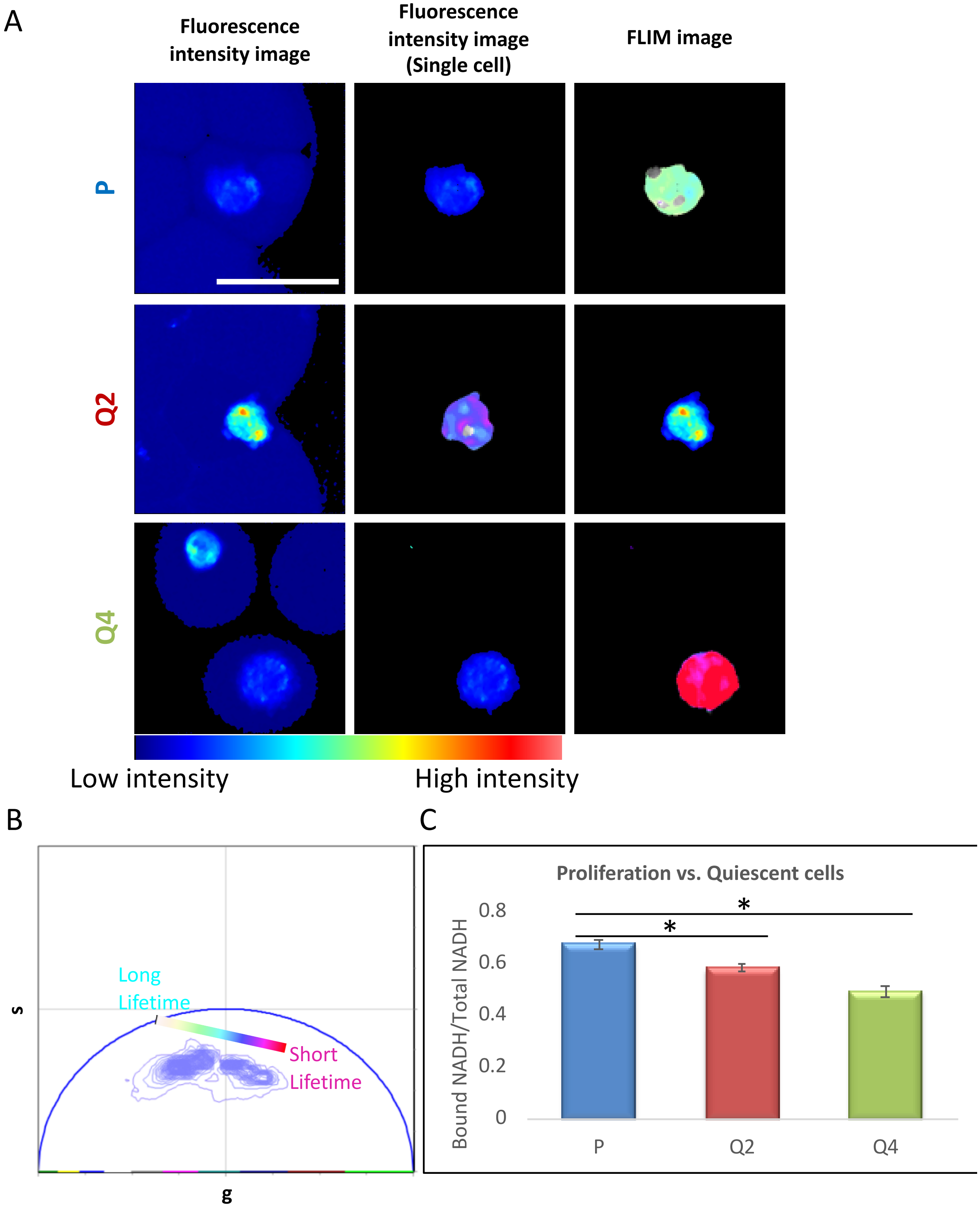

Figure 6. 5 FLIM identifies cell cycle difference

Figure 6. 5 A) Fluorescence intensity images of the single cell within droplets, and FLIM images of the human foreskin fibroblast under regular proliferation condition(P), serum starved for 2 days(Q2), and serum starved for 4 days(Q4). The FLIM images were pseudocolored by the color bar in Fig. 5B, scale bar: 50 μm. B) Phasor plot shows the FLIM signature distribution of the P, Q2 and Q4 conditions. From Cyan to Pink, the color shows the signature move from the long lifetime (higher Bound/Free NAD(P)H) to the short lifetime (lower Bound/Free NAD(P)H). **(C)** Bar graph shows the bound NAD(P)H/Total NAD(P)H ratio of the P, Q2 and Q4 conditions. The Q2 and Q4 group shows significant decreasing of Bound NAD(P)H, p-value for P and Q2 groups is 0.001, p-value for P and Q4 group is 0.002 (P group, n=21, Q2 group, n=4, Q4 group, n=19).

6.4 Concluding remarks

In summary, here we present a non-invasive, label-free single cell analysis platform combining the droplet microfluidic technology and the Fluorescence Life Time Imaging Microscopy. The single cell encapsulation technique is passive, controlled only by flow rates of the two phases and not requiring complex structures or on-chip active devices, and the label-free phasor-FLIM characterization is non-invasive without micro-environment influence. To identify between encapsulated leukemia cell types (Jurkat and K562 cells) we used the phasor-FLIM analysis and showed that excellent bi-classification (AUC: 0.980) in calculating the degree of separation between the two cell types. In another example, the differences between proliferating versus quiescence states also showed statistically significant separation in the phasor-FLIM plots. Given that cells can exhibit a quiescence state where they can exit the cell cycle by reducing their size, DNA syntheses and different metabolic activity, it would seem feasible to distinguish them from their metabolic state. Indeed, our phasor-FLIM analysis showed that the fingerprint of the proliferating versus quiescent human fibroblasts under exhibit higher free NADPH under quiescent state versus proliferative state. This may be due to the production of citrate from the conversion of α-ketoglutarate through NADPH shuttling through the mitochondria. In quiescence, NADPH is generated as a means to utilize this co-factor to synthesize fatty acids. This would indicate a higher production of NADPH would be produced to detoxify free radicals or to synthesize fatty acids under a quiescent state. The phasor analysis proved to be effective in identifying between a proliferative versus a quiescent state that can be coupled to our single cell encapsulation design[157]. The future directions of this project would be to further improve and optimize the parameters to maximize the encapsulation efficiency, perform large-scale FLIM characterization, and to incorporate the genotyping unit downstream to correlate with the phenotypic signature. Our finding suggests that FLIM-single oil droplet technique is promising as it expands the capabilities of droplet microfluidics to address applications related to single-cell high throughput early stage tumor and leukemia screening and personalized therapy by targeting quiescent tumor cells.

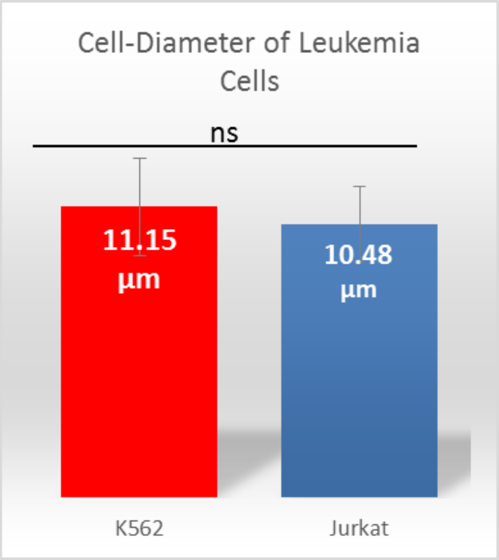

Figure 6. 6 Cell size of leukemia cell lines

Figure 6. 6 The bar graph of the single-cell diameter of K562 and Jurkat cells with no significant difference, showing the overlap of cell diameter among the different types of leukemia cells.

Chapter 7

Conclusion

“Where do we come from? What are we? Where are we going? “

These are tremendous mystery for majority of the scientists. Our study of pre- and post-implantation embryos as well as human embryonic stem cells gives me the chance to learn our origin through my thesis. From the engineering perspective, we applied fluorescence lifetime imaging microscopy technique with the different biosystems and understand the cellular metabolism, its regulation, and its influence on normal and pathological cells and tissue. In addition, we have developed a theory to quantitatively measure the concentration of the endogenous biomarkers. To bridge FLIM technique with clinical application, we also invented the widefield multi-frequency fluorescence lifetime imaging using a two-tap CMOS camera with lateral electric field charge modulators to perform FLIM imaging in a fast, 3D manner. In the end, we explore the possibility for coupling FLIM with microfluidics device for biomedical research which could be the future for disease diagnosis and targeted therapy.

In Chapter 3, we propose a graphical method that will resolve the issue of the two different quantum yields of NADH and provide absolute values of the NADH concentration using a single calibration with a solution of free NADH of known concentration. The proposed method makes use of the phasor representation of the fluorescence lifetime and of a graphical solution of the changes of the phasor position at each pixel of an image when a given amount of unmodulated light is added to the entire image. The addition of light to the lifetime decay does not require the physical addition of light in the detection pathway. In fact, it can be achieved mathematically by adding a constant value to the decay at each pixel. To our knowledge, this is the first time that such graphical approach is proposed.

We have distinguished the different FLIM signature among human embryonic stem cells with and without growth factor treatments in chapter 4. We have found the correlation of different metabolism status with distinct differentiation potential for either trophoblast differentiation or primitive streak differentiation. And we found the similar trend in post-implantation embryos. These findings could provide novel technique to select specific human embryonic stem cells differentiation type which can be used on understanding of human embryonic development, building artificial embryo model, informing us about the risks to embryos during gastrulation as well as organ transplantation research

For the FLIM application on pre-implantation embryos, we have investigated the embryonic phenotypes and achieved a quantitative metabolism interpretation of the pre-implantation mouse embryos during development based on fluorescence lifetime and absolute concentration of NADH. In addition, we develop a library to assess the physiological score in the pre-implantation mouse embryo based on NADH fluorescence lifetime and absolute concentration via an artificial intelligence algorithm. We have demonstrated that the application of the fluorescence lifetime coupled with the phasor analysis provides a non-subjective tool to assess embryo viability. This approach is noninvasive and is capable of identifying viable embryos during natural pre-implantation mouse embryo development. In addition, the EVI library data coupled with FLIM can be a foundation for IVF clinics in the future. Overall, this work has the potential to improve our understanding of metabolism in the pre-implantation embryos and advance the ART field directly or at least provide a foundation for future work that will take advantage of technologies in ways that have not been done before. At the current stage, researchers can extend the work to human embryos as well as other species for animal stock maintenance and breeding purposes.

Lastly, in chapter 6, we have explored the application combine FLIM technique with two types of microfluidic device, single cells in droplets and high-density microfluidic trapping array to signature the blood sample and the circulating tumor cells at different stage of cell cycle. Different circulating leukemia cells and blood cells can be quantitatively distinguished, and we also found the proliferating cells and quiescent cells can be differentiated as well. Positive trends have been shown for microfluidic technology development and application in the future. No matter the exact purpose (whether it be cancer diagnosis, targeted therapy, embryo selection for IVF clinics and animal husbandry or other study of immune therapy, neuron degenerative, cardiovascular disease, etc.), I believe the microfluidic technology is currently the best platform for diagnosis and treatment tests. The fast-FLIM system we have invented together with microfluidic devices for fast imaging would enhance its capabilities for detection.

Recently, we extended the phasor-FLIM technique in metabolic fingerprinting of the bovine embryo. And the preliminary data shows the FLIM signature can be used to identify the different metabolic states as well as the health of the bovine embryo, we anticipated to explore more potential in developmental biology research. Embryo viability index can be applied to mouse embryo developmental potential assessment and this technique can be used as a foundation of the embryo assessment technique for non-invasive embryo screening for in vitro fertilization, animal husbandry and potential application for genetic edited embryo and other tissue screening.

Overall, the instrumentation and imaging strategies advance of FLIM for a fast, quantitative, 3D manner and the application with developmental biology systems and microfluidic device illustrates the potential of FLIM for unveiling complex physiological processes by direct visualization of the main elements in play, focused here on the cellular metabolism. In conclusion, FLIM is a promising technique in the field of biomedical optics and can bring about tremendous advance of biomedicine as well as translational medicine. I hope my thesis can be a small step in understanding the beauty of detection and disease diagnosis through non-invasive optical imaging technique, as well as advancing the embryo screening field.

References

1 Wikipedia. *Metabolism --- {Wikipedia}, The Free Encyclopedia*, <https://en.wikipedia.org/wiki/Metabolism#History> (2019).

2 Di Cianni, G., Miccoli, R., Volpe, L., Lencioni, C. & Del Prato, S. Intermediate metabolism in normal pregnancy and in gestational diabetes. *Diabetes/metabolism research and reviews* **19**, 259-270 (2003).

3 Hsu, P. P. & Sabatini, D. M. Cancer cell metabolism: Warburg and beyond. *Cell* **134**, 703-707 (2008).

4 Hunt, T. K., Conolly, W. B., Aronson, S. B. & Goldstein, P. Anaerobic metabolism and wound healing: an hypothesis for the initiation and cessation of collagen synthesis in wounds. *The American Journal of Surgery* **135**, 328-332 (1978).

5 Weydt, P. *et al.* Thermoregulatory and metabolic defects in Huntington's disease transgenic mice implicate PGC-1α in Huntington's disease neurodegeneration. *Cell metabolism* **4**, 349-362 (2006).

6 Leese, H. J. Metabolism of the preimplantation embryo: 40 years on. *Reproduction* **143**, 417-427, doi:10.1530/REP-11-0484 (2012).

7 Gerlinger, M. *et al.* Intratumor heterogeneity and branched evolution revealed by multiregion sequencing. *New England journal of medicine* **366**, 883-892 (2012).

8 Sottoriva, A. *et al.* A Big Bang model of human colorectal tumor growth. *Nature genetics* **47**, 209 (2015).

9 White, R. E. High-throughput screening in drug metabolism and pharmacokinetic support of drug discovery. *Annual review of pharmacology and toxicology* **40**, 133-157 (2000).

10 DeBerardinis, R. J. & Thompson, C. B. Cellular metabolism and disease: what do metabolic outliers teach us? *Cell* **148**, 1132-1144 (2012).

11 Haard, N. F. (ACS Publications, 1984).

12 Lehninger, A. L., Nelson, D. L. & Cox, M. M. *Lehninger principles of biochemistry*. (Macmillan, 2005).

13 Wamelink, M., Struys, E. & Jakobs, C. The biochemistry, metabolism and inherited defects of the pentose phosphate pathway: a review. *Journal of Inherited Metabolic Disease: Official Journal of the Society for the Study of Inborn Errors of Metabolism* **31**, 703-717 (2008).

14 Rich, P. (Portland Press Limited, 2003).

15 Liberti, M. V. & Locasale, J. W. The Warburg effect: how does it benefit cancer cells? *Trends in biochemical sciences* **41**, 211-218 (2016).

16 Lunt, S. Y. & Vander Heiden, M. G. Aerobic glycolysis: meeting the metabolic requirements of cell proliferation. *Annual review of cell and developmental biology* **27**, 441-464 (2011).

17 Newsholme, E., Crabtree, B. & Ardawi, M. The role of high rates of glycolysis and glutamine utilization in rapidly dividing cells. *Bioscience reports* **5**, 393-400 (1985).

18 Clemens, M. J. Targets and mechanisms for the regulation of translation in malignant transformation. *Oncogene* **23**, 3180 (2004).

19 Vander Heiden, M. G., Cantley, L. C. & Thompson, C. B. Understanding the Warburg effect: the metabolic requirements of cell proliferation. *science* **324**, 1029-1033 (2009).

20 Ananieva, E. A. & Wilkinson, A. C. Branched-chain amino acid metabolism in cancer. *Current opinion in clinical nutrition and metabolic care* **21**, 64 (2018).

21 Reaven, G. M. & Chen, Y. D. I. Role of insulin in regulation of lipoprotein metabolism in diabetes. *Diabetes/metabolism reviews* **4**, 639-652 (1988).

22 Wang, Z. *et al.* Gut flora metabolism of phosphatidylcholine promotes cardiovascular disease. *Nature* **472**, 57 (2011).

23 Filiano, J. J., Goldenthal, M. J., Harker Rhodes, C. & Marin-Garcia, J. Mitochondrial dysfunction in patients with hypotonia, epilepsy, autism, and developmental delay: HEADD syndrome. *Journal of Child Neurology* **17**, 435-439 (2002).

24 Beal, M. F. Does impairment of energy metabolism result in excitotoxic neuronal death in neurodegenerative illnesses? *Annals of Neurology: Official Journal of the American Neurological Association and the Child Neurology Society* **31**, 119-130 (1992).

25 Krebs, H. A. & Henseleit, K. Untersuchungen uber die Harnstoffbildung im Tierkörper. *Hoppe-Seyler s Zeitschrift für physiologische Chemie* **210**, 33-66 (1932).

26 Calvin, M. The path of carbon in photosynthesis. *Angewandte Chemie International Edition in English* **1**, 65-75 (1962).

27 Tweeddale, H., Notley-McRobb, L. & Ferenci, T. Effect of slow growth on metabolism of Escherichia coli, as revealed by global metabolite pool ("metabolome") analysis. *Journal of bacteriology* **180**, 5109-5116 (1998).

28 Alonso, A., Marsal, S. & Julià, A. Analytical methods in untargeted metabolomics: state of the art in 2015. *Frontiers in bioengineering and biotechnology* **3**, 23 (2015).

29 Seli, E. *et al.* Noninvasive metabolomic profiling of embryo culture media using Raman and near-infrared spectroscopy correlates with reproductive potential of embryos in women undergoing in vitro fertilization. *Fertil Steril* **88**, 1350-1357, doi:10.1016/j.fertnstert.2007.07.1390 (2007).

30 Vergouw, C. G. *et al.* Metabolomic profiling by near-infrared spectroscopy as a tool to assess embryo viability: a novel, non-invasive method for embryo selection. *Hum Reprod* **23**, 1499-1504, doi:10.1093/humrep/den111 (2008).

31 Seli, E. *et al.* Noninvasive metabolomic profiling as an adjunct to morphology for noninvasive embryo assessment in women undergoing single embryo transfer. *Fertil Steril* **94**, 535-542, doi:10.1016/j.fertnstert.2009.03.078 (2010).

32 Smyth, E. C. & Shah, M. A. Role of (18F) 2-fluoro-2-deoxyglucose positron emission tomography in upper gastrointestinal malignancies. *World journal of gastroenterology: WJG* **17**, 5059 (2011).

33 Qu, W. *et al.* Synthesis of optically pure 4-fluoro-glutamines as potential metabolic imaging agents for tumors. *Journal of the American Chemical Society* **133**, 1122-1133 (2010).

34 Golman, K. & Thaning, M. Real-time metabolic imaging. *Proceedings of the National Academy of Sciences* **103**, 11270-11275 (2006).

35 Ferrick, D. A., Neilson, A. & Beeson, C. Advances in measuring cellular bioenergetics using extracellular flux. *Drug discovery today* **13**, 268-274 (2008).

36 Salabei, J. K., Gibb, A. A. & Hill, B. G. Comprehensive measurement of respiratory activity in permeabilized cells using extracellular flux analysis. *Nature protocols* **9**, 421 (2014).

37 Scott, T. G., Spencer, R. D., Leonard, N. J. & Weber, G. Synthetic spectroscopic models related to coenzymes and base pairs. V. Emission properties of NADH. Studies of fluorescence lifetimes and quantum efficiencies of NADH, AcPyADH,[reduced acetylpyridineadenine dinucleotide] and simplified synthetic models. *Journal of the American Chemical Society* **92**, 687-695 (1970).

38 Ramanujam, N. Fluorescence spectroscopy of neoplastic and non-neoplastic tissues. *Neoplasia* **2**, 89-117 (2000).

39 Berezin, M. Y. & Achilefu, S. Fluorescence lifetime measurements and biological imaging. *Chemical reviews* **110**, 2641-2684 (2010).

40 Leenders, R., Kooijman, M., van Hoek, A., Veeger, C. & Visser, A. J. Flavin dynamics in reduced flavodoxins: A time-resolved polarized fluorescence study. *European journal of biochemistry* **211**, 37-45 (1993).

41 Balu, M., Mikami, H., Hou, J., Potma, E. O. & Tromberg, B. J. Rapid mesoscale multiphoton microscopy of human skin. *Biomedical optics express* **7**, 4375-4387 (2016).

42 Heikal, A. A. Intracellular coenzymes as natural biomarkers for metabolic activities and mitochondrial anomalies. *Biomarkers in medicine* **4**, 241-263 (2010).

43 Bird, D. K. *et al.* Metabolic mapping of MCF10A human breast cells via multiphoton fluorescence lifetime imaging of the coenzyme NADH. *Cancer Res* **65**, 8766-8773, doi:10.1158/0008-5472.CAN-04-3922 (2005).

44 Scholz, R., Thurman, R. G., Williamson, J. R., Chance, B. & Bücher, T. Flavin and Pyridine Nucleotide Oxidation-Reduction Changes in Perfused Rat Liver I. ANOXIA AND SUBCELLULAR LOCALIZATION OF FLUORESCENT FLAVOPROTEINS. *Journal of Biological Chemistry* **244**, 2317-2324 (1969).

45 Huang, S., Heikal, A. A. & Webb, W. W. Two-photon fluorescence spectroscopy and microscopy of NAD (P) H and flavoprotein. *Biophysical journal* **82**, 2811-2825 (2002).

46 Skala, M. C. *et al.* In vivo multiphoton microscopy of NADH and FAD redox states, fluorescence lifetimes, and cellular morphology in precancerous epithelia. *Proc Natl Acad Sci U S A* **104**, 19494-19499, doi:10.1073/pnas.0708425104 (2007).

47 Rocheleau, J. V., Head, W. S. & Piston, D. W. Quantitative NAD (P) H/flavoprotein autofluorescence imaging reveals metabolic mechanisms of pancreatic islet pyruvate response. *Journal of Biological Chemistry* **279**, 31780-31787 (2004).

48 Skala, M. & Ramanujam, N. in *Advanced Protocols in Oxidative Stress II* 155-162 (Springer, 2010).

49 Quinn, K. P. *et al.* Quantitative metabolic imaging using endogenous fluorescence to detect stem cell differentiation. *Scientific reports* **3**, 3432 (2013).

50 Lakowicz, J. R., Szmacinski, H., Nowaczyk, K. & Johnson, M. L. Fluorescence lifetime imaging of free and protein-bound NADH. *Proc Natl Acad Sci U S A* **89**, 1271-1275 (1992).

51 Datta, R., Alfonso-García, A., Cinco, R. & Gratton, E. Fluorescence lifetime imaging of endogenous biomarker of oxidative stress. *Sci Rep* **5**, 9848, doi:10.1038/srep09848 (2015).

52 Joensson, H. N. & Andersson Svahn, H. Droplet Microfluidics—A Tool for Single-Cell Analysis. *Angewandte Chemie International Edition* **51**, 12176-12192 (2012).

53 Ma, N., Digman, M. A., Malacrida, L. & Gratton, E. Measurements of absolute concentrations of NADH in cells using the phasor FLIM method. *Biomedical optics express* **7**, 2441-2452 (2016).

54 Blacker, T. S. *et al.* Separating NADH and NADPH fluorescence in live cells and tissues using FLIM. *Nature communications* **5** (2014).

55 Reiss, P. D., Zuurendonk, P. F. & Veech, R. L. Measurement of tissue purine, pyrimidine, and other nucleotides by radial compression high-performance liquid chromatography. *Analytical biochemistry* **140**, 162-171 (1984).

56 Blinova, K. *et al.* Distribution of mitochondrial NADH fluorescence lifetimes: steady-state kinetics of matrix NADH interactions. *Biochemistry* **44**, 2585-2594 (2005).

57 Bonda, D. J. *et al.* The sirtuin pathway in ageing and Alzheimer disease: mechanistic and therapeutic considerations. *The Lancet Neurology* **10**, 275-279 (2011).

58 Chance, B. in *Methods in enzymology* Vol. 385 361-370 (Elsevier, 2004).

59 Kasimova, M. R. *et al.* The free NADH concentration is kept constant in plant mitochondria under different metabolic conditions. *The Plant Cell* **18**, 688-698 (2006).

60 Mayevsky, A. & Chance, B. in *Oxygen Transport to Tissue* 239-244 (Springer, 1973).

61 Plotegher, N. *et al.* NADH fluorescence lifetime is an endogenous reporter of α-synuclein aggregation in live cells. *The FASEB Journal* **29**, 2484-2494 (2015).

62 Stringari, C. *et al.* Metabolic trajectory of cellular differentiation in small intestine by Phasor Fluorescence Lifetime Microscopy of NADH. *Scientific reports* **2**, 568 (2012).

63 Stringari, C., Nourse, J. L., Flanagan, L. A. & Gratton, E. Phasor fluorescence lifetime microscopy of free and protein-bound NADH reveals neural stem cell differentiation potential. *PLoS One* **7**, e48014, doi:10.1371/journal.pone.0048014 (2012).

64 Torno, K. *et al.* Real-time analysis of metabolic activity within Lactobacillus acidophilus by phasor fluorescence lifetime imaging microscopy of NADH. *Current microbiology* **66**, 365-367 (2013).

65 Wright, B. K. *et al.* Phasor-FLIM analysis of NADH distribution and localization in the nucleus of live progenitor myoblast cells. *Microsc Res Tech* **75**, 1717-1722, doi:10.1002/jemt.22121 (2012).

66 Wright, B. K. *et al.* NADH distribution in live progenitor stem cells by phasor-fluorescence lifetime image microscopy. *Biophysical journal* **103**, L7-L9 (2012).

67 Wright, B. K. *et al.* Phasor-flim analysis of NADH distribution and localization in the nucleus of live progenitor myoblast cells. *Microscopy research and technique* **75**, 1717-1722 (2012).

68 Waters, J. C. (Rockefeller University Press, 2009).

69 Jameson, D. M., Thomas, V. & Zhou, D. M. Time-resolved fluorescence studies on NADH bound to mitochondrial malate dehydrogenase. *Biochim Biophys Acta* **994**, 187-190 (1989).

70 Kierdaszuk, B., Malak, H., Gryczynski, I., Callis, P. & Lakowicz, J. R. Fluorescence of reduced nicotinamides using one-and two-photon excitation. *Biophysical chemistry* **62**, 1-13 (1996).

71 Sánchez, S. A., Brunet, J. E., Hazlett, T. L. & Jameson, D. M. Aggregation states of mitochondrial malate dehydrogenase. *Protein science* **7**, 2184-2189 (1998).

72 Skala, M. C. *et al.* In vivo multiphoton fluorescence lifetime imaging of protein-bound and free nicotinamide adenine dinucleotide in normal and precancerous epithelia. *Journal of biomedical optics* **12**, 024014 (2007).

73 Provenzano, P. P., Eliceiri, K. W. & Keely, P. J. Multiphoton microscopy and fluorescence lifetime imaging microscopy (FLIM) to monitor metastasis and the tumor microenvironment. *Clinical & experimental metastasis* **26**, 357-370 (2009).

74 Blacker, T. S. *et al.* Separating NADH and NADPH fluorescence in live cells and tissues using FLIM. *Nature communications* **5**, 3936 (2014).

75 Venkateswaran, A. *et al.* The NADH oxidase ENOX1, a critical mediator of endothelial cell radiosensitization, is crucial for vascular development. *Cancer research* **74**, 38-43 (2014).

76 Kalinina, S. *et al.* Correlative NAD (P) H-FLIM and oxygen sensing-PLIM for metabolic mapping. *Journal of biophotonics* **9**, 800-811 (2016).

77 Kang, C. *et al.* Quantitative fluorescence kinetic analysis of NADH and FAD in human plasma using three-and four-way calibration methods capable of providing the second-order advantage. *Analytica chimica acta* **910**, 36-44 (2016).

78 Meleshina, A. V. *et al.* Probing metabolic states of differentiating stem cells using two-photon FLIM. *Scientific reports* **6**, 21853 (2016).

79 Yu, Q. & Heikal, A. A. Two-photon autofluorescence dynamics imaging reveals sensitivity of intracellular NADH concentration and conformation to cell physiology at the single-cell level. *Journal of Photochemistry and Photobiology B: Biology* **95**, 46-57 (2009).

80 Digman, M. A., Caiolfa, V. R., Zamai, M. & Gratton, E. The phasor approach to fluorescence lifetime imaging analysis. *Biophysical journal* **94**, L14-L16 (2008).

81 Stringari, C. *et al.* Phasor approach to fluorescence lifetime microscopy distinguishes different metabolic states of germ cells in a live tissue. *Proc Natl Acad Sci U S A* **108**, 13582-13587, doi:10.1073/pnas.1108161108 (2011).

82 Kolb, D. A. & Weber, G. Quantitative demonstration of the reciprocity of ligand effects in the ternary complex of chicken heart lactate dehydrogenase with nicotinamide adenine dinucleotide and oxalate. *Biochemistry* **14**, 4471-4476 (1975).

83 Jameson, D. M. & Mocz, G. in *Protein-Ligand Interactions* 301-322 (Springer, 2005).

84 Digman, M. A., Caiolfa, V. R., Zamai, M. & Gratton, E. The phasor approach to fluorescence lifetime imaging analysis. *Biophys J* **94**, L14-16, doi:10.1529/biophysj.107.120154 (2008).

85 Datta, R., Alfonso-Garcia, A., Cinco, R. & Gratton, E. Fluorescence lifetime imaging of endogenous biomarker of oxidative stress. *Sci Rep* **5**, 9848, doi:10.1038/srep09848 (2015).

86 Folmes, C. D., Dzeja, P. P., Nelson, T. J. & Terzic, A. Metabolic plasticity in stem cell homeostasis and differentiation. *Cell stem cell* **11**, 596-606 (2012).

87 Panopoulos, A. D. & Belmonte, J. C. I. Anaerobicizing into pluripotency. *Cell metabolism* **14**, 143-144 (2011).

88 Shyh-Chang, N., Daley, G. Q. & Cantley, L. C. Stem cell metabolism in tissue development and aging. *Development* **140**, 2535-2547 (2013).

89 Zhang, J. *et al.* UCP2 regulates energy metabolism and differentiation potential of human pluripotent stem cells. *The EMBO journal* **30**, 4860-4873 (2011).

90 Zhang, J. *et al.* Measuring energy metabolism in cultured cells, including human pluripotent stem cells and differentiated cells. *Nature protocols* **7**, 1068 (2012).

91 Stringari, C. *et al.* Phasor approach to fluorescence lifetime microscopy distinguishes different metabolic states of germ cells in a live tissue. *Proceedings of the National Academy of Sciences* **108**, 13582-13587 (2011).

92 Stringari, C., Sierra, R., Donovan, P. J. & Gratton, E. Label-free separation of human embryonic stem cells and their differentiating progenies by phasor fluorescence lifetime microscopy. *J Biomed Opt* **17**, 046012, doi:10.1117/1.JBO.17.4.046012 (2012).

93 Pate, K. T. *et al.* Wnt signaling directs a metabolic program of glycolysis and angiogenesis in colon cancer. *EMBO J* **33**, 1454-1473, doi:10.15252/embj.201488598 (2014).

94 Colyer, R. A., Lee, C. & Gratton, E. A novel fluorescence lifetime imaging system that optimizes photon efficiency. *Microscopy research and technique* **71**, 201-213 (2008).

95 Brivanlou, A. H. (ELSEVIER ACADEMIC PRESS INC 525 B STREET, SUITE 1900, SAN DIEGO, CA 92101 …, 2018).

96 Ying, L., Mills, J. A., French, D. L. & Gadue, P. OCT4 coordinates with WNT signaling to pre-pattern chromatin at the SOX17 locus during human ES cell differentiation into definitive endoderm. *Stem cell reports* **5**, 490-498 (2015).

97 Kurek, D. *et al.* Endogenous WNT signals mediate BMP-induced and spontaneous differentiation of epiblast stem cells and human embryonic stem cells. *Stem cell reports* **4**, 114-128 (2015).

98 Figueiredo, G. S., De Havilland, J. R., Lako, M. & Figueiredo, F. C. Cell Therapy in Practice. *Bioprocessing cell-based therapies* (2017).

99 Martyn, I., Kanno, T., Ruzo, A., Siggia, E. & Brivanlou, A. Self-organization of a functional human organizer by combined WNT and NODAL signalling. *bioRxiv*, 234633 (2017).

100 Yoney, A. *et al.* WNT signaling memory is required for ACTIVIN to function as a morphogen in human gastruloids. *eLife* **7**, e38279 (2018).

101 Sozen, B. *et al.* Self-assembly of embryonic and two extra-embryonic stem cell types into gastrulating embryo-like structures. Report No. 1476-4679, (Nature Publishing Group, 2018).

102 Baczkowski, T., Kurzawa, R. & Głabowski, W. Methods of embryo scoring in in vitro fertilization. *Reprod Biol* **4**, 5-22 (2004).

103 De Sutter, P., Dozortsev, D., Qian, C. & Dhont, M. Oocyte morphology does not correlate with fertilization rate and embryo quality after intracytoplasmic sperm injection. *Human Reproduction* **11**, 595-597 (1996).

104 Scott, L. A. & Smith, S. The successful use of pronuclear embryo transfers the day following oocyte retrieval. *Human Reproduction* **13**, 1003-1013 (1998).

105 Gardner, D. K., Lane, M., Stevens, J., Schlenker, T. & Schoolcraft, W. B. Blastocyst score affects implantation and pregnancy outcome: towards a single blastocyst transfer. *Fertility and sterility* **73**, 1155-1158 (2000).

106 Scott, R. *et al.* Noninvasive metabolomic profiling of human embryo culture media using Raman spectroscopy predicts embryonic reproductive potential: a prospective blinded pilot study. *Fertil Steril* **90**, 77-83, doi:10.1016/j.fertnstert.2007.11.058 (2008).

107 González, R. R. *et al.* Leptin and leptin receptor are expressed in the human endometrium and endometrial leptin secretion is regulated by the human blastocyst 1. *The Journal of Clinical Endocrinology & Metabolism* **85**, 4883-4888 (2000).

108 Sher, G., Keskintepe, L., Nouriani, M., Roussev, R. & Batzofin, J. Expression of sHLA-G in supernatants of individually cultured 46-h embryos: a potentially valuable indicator of 'embryo competency'and IVF outcome. *Reproductive biomedicine online* **9**, 74-78 (2004).

109 Botros, L., Sakkas, D. & Seli, E. Metabolomics and its application for non-invasive embryo assessment in IVF. *Molecular human reproduction* **14**, 679-690 (2008).

110 Squirrell, J. M., Wokosin, D. L., White, J. G. & Bavister, B. D. Long-term two-photon fluorescence imaging of mammalian embryos without compromising viability. *Nat Biotechnol* **17**, 763-767, doi:10.1038/11698 (1999).

111 Gardner, D. K. & Wale, P. L. Analysis of metabolism to select viable human embryos for transfer. *Fertil Steril* **99**, 1062-1072, doi:10.1016/j.fertnstert.2012.12.004 (2013).

112 Wale, P. L. & Gardner, D. K. The effects of chemical and physical factors on mammalian embryo culture and their importance for the practice of assisted human reproduction. *Hum Reprod Update* **22**, 2-22, doi:10.1093/humupd/dmv034 (2016).

113 Leese, H. J. & Barton, A. M. Pyruvate and glucose uptake by mouse ova and preimplantation embryos. *J Reprod Fertil* **72**, 9-13 (1984).

114 Dumollard, R., Carroll, J., Duchen, M., Campbell, K. & Swann, K. in *Seminars in cell & developmental biology.* 346-353 (Elsevier).

115 König, K., So, P. C., Mantulin, W., Tromberg, B. & Gratton, E. Two-photon excited lifetime imaging of autofluorescence in cells during UV A and NIR photostress. *Journal of microscopy* **183**, 197-204 (1996).

116 *ISS | Technical Notes | Fluorescence Lifetime*, <http://www.iss.com/resources/research/technical_notes/K2CH_FLT.html> (2016).

117 Berezin, M. Y. & Achilefu, S. Fluorescence lifetime measurements and biological imaging. *Chem Rev* **110**, 2641-2684, doi:10.1021/cr900343z (2010).

118 Chiang, M. *et al.* Analysis of in vivo single cell behavior by high throughput, human-in-the-loop segmentation of three-dimensional images. *BMC Bioinformatics* **16**, 397, doi:10.1186/s12859-015-0814-7 (2015).

119 Ranjit, S., Dvornikov, A., Levi, M., Furgeson, S. & Gratton, E. Characterizing fibrosis in UUO mice model using multiparametric analysis of phasor distribution from FLIM images. *Biomedical Optics Express* **7**, 3519-3530 (2016).

120 Shyh-Chang, N., Daley, G. Q. & Cantley, L. C. Stem cell metabolism in tissue development and aging. *Development* **140**, 2535-2547, doi:10.1242/dev.091777 (2013).

121 Covarrubias, L., Hernández-García, D., Schnabel, D., Salas-Vidal, E. & Castro-Obregón, S. Function of reactive oxygen species during animal development: passive or active? *Developmental biology* **320**, 1-11 (2008).

122 Ray, P. D., Huang, B.-W. & Tsuji, Y. Reactive oxygen species (ROS) homeostasis and redox regulation in cellular signaling. *Cellular signalling* **24**, 981-990 (2012).

123 Esterbauer, H. Cytotoxicity and genotoxicity of lipid-oxidation products. *Am J Clin Nutr* **57**, 779S-785S; discussion 785S-786S (1993).

124 Gardner, D. K., Lane, M., Calderon, I. & Leeton, J. Environment of the preimplantation human embryo in vivo: metabolite analysis of oviduct and uterine fluids and metabolism of cumulus cells. *Fertil Steril* **65**, 349-353 (1996).

125 Lane, M. & Gardner, D. K. Lactate Regulates Pyruvate Uptake and Metabolism in the PreimplantationMouse Embryo. *Biology of reproduction* **62**, 16-22 (2000).

126 Watanabe, T. *et al.* Characterisation of the dynamic behaviour of lipid droplets in the early mouse embryo using adaptive harmonic generation microscopy. *BMC Cell Biol* **11**, 38, doi:10.1186/1471-2121-11-38 (2010).

127 Hamaoka, T., McCully, K. K., Quaresima, V., Yamamoto, K. & Chance, B. Near-infrared spectroscopy/imaging for monitoring muscle oxygenation and oxidative metabolism in healthy and diseased humans. *J Biomed Opt* **12**, 062105, doi:10.1117/1.2805437 (2007).

128 Stringari, C. *et al.* Metabolic trajectory of cellular differentiation in small intestine by Phasor Fluorescence Lifetime Microscopy of NADH. *Sci Rep* **2**, 568, doi:10.1038/srep00568 (2012).

129 Wang, Z. W. *et al.* Laser microbeam-induced DNA damage inhibits cell division in fertilized eggs and early embryos. *Cell Cycle* **12**, 3336-3344, doi:10.4161/cc.26327 (2013).

130 Revet, I. *et al.* Functional relevance of the histone gammaH2Ax in the response to DNA damaging agents. *Proc Natl Acad Sci U S A* **108**, 8663-8667, doi:10.1073/pnas.1105866108 (2011).

131 Sonoda, E. *et al.* Collaborative roles of gammaH2AX and the Rad51 paralog Xrcc3 in homologous recombinational repair. *DNA Repair (Amst)* **6**, 280-292, doi:10.1016/j.dnarep.2006.10.025 (2007).

132 Lane, M. & Gardner, D. K. Mitochondrial malate-aspartate shuttle regulates mouse embryo nutrient consumption. *Journal of Biological Chemistry* **280**, 18361-18367 (2005).

133 Bolton, H. *et al.* Mouse model of chromosome mosaicism reveals lineage-specific depletion of aneuploid cells and normal developmental potential. *Nature communications* **7**, 11165 (2016).

134 Navin, N. *et al.* Tumour evolution inferred by single-cell sequencing. *Nature* **472**, 90 (2011).

135 Di Carlo, D., Tse, H. T. K. & Gossett, D. R. in *Single-Cell Analysis* 1-10 (Springer, 2012).

136 Collins, D. J., Neild, A., Liu, A.-Q. & Ai, Y. The Poisson distribution and beyond: methods for microfluidic droplet production and single cell encapsulation. *Lab on a Chip* **15**, 3439-3459 (2015).

137 He, M. *et al.* Selective encapsulation of single cells and subcellular organelles into picoliter-and femtoliter-volume droplets. *Analytical chemistry* **77**, 1539-1544 (2005).

138 Schoendube, J., Wright, D., Zengerle, R. & Koltay, P. Single-cell printing based on impedance detection. *Biomicrofluidics* **9**, 014117 (2015).

139 Chabert, M. & Viovy, J.-L. Microfluidic high-throughput encapsulation and hydrodynamic self-sorting of single cells. *Proceedings of the National Academy of Sciences* **105**, 3191-3196 (2008).

140 Kemna, E. W. *et al.* High-yield cell ordering and deterministic cell-in-droplet encapsulation using Dean flow in a curved microchannel. *Lab on a Chip* **12**, 2881-2887 (2012).

141 Edd, J. F. *et al.* Controlled encapsulation of single-cells into monodisperse picolitre drops. *Lab on a Chip* **8**, 1262-1264 (2008).

142 Kamalakshakurup, G. & Lee, A. P. High-efficiency single cell encapsulation and size selective capture of cells in picoliter droplets based on hydrodynamic micro-vortices. *Lab on a Chip* **17**, 4324-4333 (2017).

143 Bendall, S. C. *et al.* Single-cell mass cytometry of differential immune and drug responses across a human hematopoietic continuum. *Science* **332**, 687-696 (2011).
144 Pepperkok, R. & Ellenberg, J. High-throughput fluorescence microscopy for systems biology. *Nature Reviews Molecular Cell Biology* **7**, 690 (2006).
145 Brouzes, E. *et al.* Droplet microfluidic technology for single-cell high-throughput screening. *Proceedings of the National Academy of Sciences* **106**, 14195-14200 (2009).
146 Macosko, E. Z. *et al.* Highly parallel genome-wide expression profiling of individual cells using nanoliter droplets. *Cell* **161**, 1202-1214 (2015).
147 Klein, A. M. *et al.* Droplet barcoding for single-cell transcriptomics applied to embryonic stem cells. *Cell* **161**, 1187-1201 (2015).
148 Chance, B. & Williams, G. Respiratory enzymes in oxidative phosphorylation II. Difference spectra. *Journal of Biological Chemistry* **217**, 395-408 (1955).
149 Chance, B. & Williams, G. Respiratory enzymes in oxidative phosphorylation III. The steady state. *Journal of Biological Chemistry* **217**, 409-428 (1955).
150 Brodie, B. B., Gillette, J. R. & La Du, B. N. Enzymatic metabolism of drugs and other foreign compounds. *Annual review of biochemistry* **27**, 427-454 (1958).
151 Ying, W. NAD+/NADH and NADP+/NADPH in cellular functions and cell death: regulation and biological consequences. *Antioxidants & redox signaling* **10**, 179-206 (2008).
152 Zoumi, A., Yeh, A. & Tromberg, B. J. Imaging cells and extracellular matrix in vivo by using second-harmonic generation and two-photon excited fluorescence. *Proceedings of the National Academy of Sciences* **99**, 11014-11019 (2002).
153 Kukreti, S. *et al.* Characterization of metabolic differences between benign and malignant tumors: high-spectral-resolution diffuse optical spectroscopy. *Radiology* **254**, 277-284 (2009).
154 Dimitrow, E. *et al.* Spectral fluorescence lifetime detection and selective melanin imaging by multiphoton laser tomography for melanoma diagnosis. *Experimental dermatology* **18**, 509-515 (2009).
155 Lee, D.-H., Li, X., Ma, N., Digman, M. A. & Lee, A. P. Rapid and label-free identification of single leukemia cells from blood in a high-density microfluidic trapping array by fluorescence lifetime imaging microscopy. *Lab on a Chip* **18**, 1349-1358 (2018).
156 Jang, M., Kim, S. S. & Lee, J. Cancer cell metabolism: implications for therapeutic targets. *Experimental & molecular medicine* **45**, e45 (2013).
157 Lemons, J. M. *et al.* Quiescent fibroblasts exhibit high metabolic activity. *PLoS biology* **8**, e1000514 (2010).
158 Sagone Jr, A. L., LoBuglio, A. F. & Balcerzak, S. P. Alterations in hexose monophosphate shunt during lymphoblastic transformation. *Cellular immunology* **14**, 443-452 (1974).
159 Barbehenn, E. K., Wales, R. G. & Lowry, O. H. The explanation for the blockade of glycolysis in early mouse embryos. *Proc Natl Acad Sci U S A* **71**, 1056-1060 (1974).
160 Xia, Y. George m. Whitesides. *Annu. Rev. Mater. Sci* **28**, 153-184 (1998).

161 Schneider, C. A., Rasband, W. S. & Eliceiri, K. W. NIH Image to ImageJ: 25 years of image analysis. *Nature methods* **9**, 671 (2012).
162 Tan, Y.-C., Cristini, V. & Lee, A. P. Monodispersed microfluidic droplet generation by shear focusing microfluidic device. *Sensors and Actuators B: Chemical* **114**, 350-356 (2006).
163 Golpour, M. *et al.* Human fibroblast switches to anaerobic metabolic pathway in response to serum starvation: a mimic of warburg effect. *International journal of molecular and cellular medicine* **3**, 74 (2014).
164 Barar, J. & Omidi, Y. Dysregulated pH in tumor microenvironment checkmates cancer therapy. *BioImpacts: BI* **3**, 149 (2013).
165 Kato, Y. *et al.* Acidic extracellular microenvironment and cancer. *Cancer cell international* **13**, 89 (2013).
166 Philp, A., Macdonald, A. L. & Watt, P. W. Lactate–a signal coordinating cell and systemic function. *Journal of Experimental Biology* **208**, 4561-4575 (2005).
167 Schor, S. L., Schor, A. M., Grey, A. & Rushton, G. Foetal and cancer patient fibroblasts produce an autocrine migration-stimulating factor not made by normal adult cells. *Journal of cell science* **90**, 391-399 (1988).